Department of Pure and Applied Chemistry

Chalcogenopyrylium Dye Functionalised Gold Nanoparticles for use as Red-Shifted SERS Nanotags

Amy Morrison

A Thesis submitted to the Department of Pure and Applied Chemistry, University of Strathclyde, in fulfilment of the requirements for the degree of Doctor of Philosophy.

July 2019

The thesis is the result of the author's original research. It has been composed by the author and has not been previously submitted for examination that lead to the award of the degree.

Amy Morrison

The University of Strathclyde

Author Signed:

Date:

Acknowledgements

I would like to start by thanking my supervisors Professor Duncan Graham *throws fist in air* and Professor Karen Faulds *stares intimidatingly from across the room* for allowing me to carry out my PhD research in their research group and for all the help, guidance and occasional 'you've been good' cake and treats over the years. I would like to express my thanks to Professor Ewen Smith for his Raman tutorials, helpful discussions and always checking in on me when he popped into the office. I would also like to thank Professor Neil Shand at DSTL for his help with the DSTL area of my project.

I would like to extend a massive thank you the research group, the Postdocs and students over the years for their help, useful discussions and general good times. I definitely could not have gotten though the difficult times without you all. A few of you deserve extra special thanks: Corinna Wetherill, not only are you the glue that holds this group together you are my work-mum and I am eternally grateful for you. Thank you for checking in on me during the darker days and listening to me rant about life problems. Thank you for your help with the cell studies, general lab issues and well, everything really! Dr. Kirsten Gracie, thank you listening to me when I needed to moan about life and for not allowing me to quit when I was ready to walk away during my second year. Dr. Lauren Jamieson, thank you for all your Matlab help, pep talks, chocolate and general uplifting spirit – however, I still cannot believe you left me in my final three months! The Iceland Massive: Anastasia Kapara, Daniel MacDonald, and Kirsty Callan, you guys were absolute rocks throughout this entire process, thank you for the chats, the rants, the help, the chocolate eggs – everything! Kirsty Milligan, those who DSTL together stay together, am I right! Remember we have a pact, always ready to pack up, move to Australia and pick tomatoes should things go south. Rachael Cameron, you are some woman, thank you for listening to my moans, instilling words of wisdom and sense upon me and generally being one of the best human beings I have met. Fatima Ali, where do I start? Thank you for being so kind, so upbeat and quite possibly the most wonderful person I have ever met. I will miss your massive

smile, neck rubs and treat drawer that is for sure! Craig ward, thank you for the chats, therapy and the mutual understanding of the massive pain in my bum throughout the years. Jenny Gracie, thank you for being patient every time I shouted over "Jennnyyy can I ask a question…?" I would not have become the PowerPoint and formatting whizz I am today without your help. Finally, thanks to Dr. Sian Sloan-Dennison, Dr. Stacey Laing and Dr. Will Tipping for all of your helpful comments in regard to the initial draft of my thesis.

I would like to thank Professor Michael Detty, Kosta Plakas and Lauren Rosch, for providing the dyes necessary for this research to have taken place. I would also like to thank you and the rest of the Detty group for being such good sports and making my trip to Buffalo in April/May 2018 such an enjoyable experience. Contrary to popular belief, I learned a lot about your strange synthetic dye world, and I am very grateful for the opportunity.

I would not have made it through these three and a half years if it were not for Lindsay McCulloch and his Friday therapy sessions. Thank you for your friendship, wisdom and general good banter, if I ever make it big time I'll buy you tickets to all the airport lounges for you to watch all the aeroplanes your heart desires.

I would like to extend my thanks to the ScotCHEM PECRE funding program, the Royal Society of Chemistry, and the Association of British Spectroscopists for allowing me to attend multiple conferences and undertake a placement at the University at Buffalo with their generous travel grant awards.

I would like to thank my friends and family for the support despite having absolutely no idea what I do on a daily basis or why I do it. Being a 'time wasting student without a real job' for almost 9 years has its advantages. In particular, Kathleen and Winnie for the Saturday coffees and treks around M&S.

Finally, Joshua. Where do I start with you? Thank you for swooping in at the very end and being the lifeline I so very much needed, you truly are everything. I will be sure to return the favour when it is your turn. Now, about the 11 am pancakes…

Abstract

Surface enhanced Raman spectroscopy (SERS) in the near infrared (NIR) is a largely unexplored area in Raman spectroscopy, particularly at laser excitation wavelengths greater than 1100 nm. This thesis explores the use of a 1280 nm Raman spectrometer for NIR Raman active nanotag design and application. The NIR region of the electromagnetic spectrum is of specific interest due to the absorption and scattering properties in biological matter throughout this optical window.

Research described in chapter 3 of this thesis highlights the use of a relatively novel class of chalcogenopyrylium (CP) dye molecules, which in combination with the broad extinction profile of large gold nanoparticles (AuNPs) provide an intense SERS response upon 1280 nm laser excitation, previously unachievable with commercially available Raman reporter molecules at this excitation wavelength. However, the structural design of these dyes specifically relating to their SERS performance is unreported. The relationship between CP dye molecule binding orientation, determined *via* sum frequency generation vibrational spectroscopy (SFG-VS), and their SERS response was investigated deducing that due to the polarisation throughout the backbone of the CP dye molecule, an optimal SERS response was achieved when the CP dye molecule is as perpendicular to the NP surface as possible.

Due to the increasing technological advances surrounding counterfeit and fraudulent goods, investigation into the design of a nanotag that could be selectively detected by only those with the knowledge of how to detect it could be incredibly advantageous in the fight against consumer goods piracy and in the secure labelling of important documents. Chapter 4 of this thesis reports the design of such a nanotag using an already established CP dye as the Raman reporter and a novel, purposefully designed, CP based dye blocking molecule (BM) which is able to block or mask the SERS signal from the Raman reporter at 785 nm laser excitation, only providing a SERS response, from the nanotag, upon excitation with a 1280 nm laser source. This resulted in the ability to obtain a

SERS response with a 1280 nm Raman spectrometer that was not achieved at 785 nm laser excitation, by either complete signal elimination or by masking from the BM itself. This could provide the ability to invisibly tag and detect items of vital importance in which no one else, unless equipped with this nanotag, 1280 nm Raman spectrometer and system knowledge could or should be able to identify.

In order for biomedical research to advance away from dated, bulkier, fixed instrumentation, performance of handheld instrumentation, capable of being adapted into a clinical environment, needs to be explored. Previous group work has investigated the performance of CP dye based nanotags at depth through biological tissues by use of spatially offset Raman spectroscopy (SORS). As SORS is a technique which will acquire a Raman measurement at a pre-determined depth, work was also carried out in order to deduce the depth at which a conventional 785 nm Raman spectrometer could detect these nanotags in tissue samples. However, the ability to probe through biological barriers using further red-shifted excitation wavelengths has not yet been studied. Chapter 5 of this thesis reports and compares the depth, in tissue samples, at which CP dye based nanotags can be detected using portable conventional handheld Raman spectrometers of laser excitation wavelengths: 785, 1064 and 1280 nm.

Recent reports have emerged, in the literature, employing CP dye based nanotags in a variety of biological applications including localisation within and detection of cancerous tumours, cell-based cancer models and in *ex vivo* multiplexing platforms, however, to date their cytotoxicity has gone unreported. Chapter 6 of this thesis examines the cytotoxicity of five CP based dye nanotags, two of which have already been employed and reported in biological applications, to a healthy prostate cancer cell line and additionally demonstrates their level of detectability in cells. Finally, towards the end of this research, CP dye molecules containing alkyne moieties were made available. Alkyne tags are of extreme interest in biological, and in particular cellular, applications due to the fact their characteristic alkyne peak occurs in the 'biologically silent' region of the spectrum. The ability to perform as SERS active nanotags, providing the

characteristic alkyne peak in the ‘biologically silent’ region of the spectrum, at a 1064 nm laser excitation wavelength is demonstrated and discussed.

Abbreviations

4-Mercaptobenzoic acid	4-MBA
Active pharmaceutical ingredient	API
Ascorbic acid	AA
Blocking molecule	BM
Cetyl-trimethylammonium bromide	CTAB
Chalgogenopyrylium	CP
Copper nanoparticle	CuNPs
Dihydroartemisinin	DHA
Direct classical least square	DCLS
Dynamic light scattering	DLS
Ethylenediaminetetraacetic acid	EDTA
Epidermal growth factor receptor	EGFR
Far-infrared	FIR
Fetal bovine serum	FBS
Gold nanoparticle	AuNP
Gold nanorod	AuNR
Gold nanostar	AuNS
Highest occupied molecular orbital	HOMO
Hollow gold nanoparticle	HGN
Infra-red	IR
Localised surface plasmon resonance	LSPR
Lowest unoccupied molecular orbital	LUMO

Magnetic resonance imaging	MRI
Multicellular tumour spheroids	MTS
N,N-Dimethylformamide	DMF
Nanoparticle	NP
Nanotag	NT
Nanorod	NR
Nanostar	NS
Near-infrared	NIR
Para-aminothiophenol	p-ATP
Paraformaldehyde	PFA
Poly(methyl methacrylate)	PMMA
Polyethylene terephthalate	PET
Positron emission tomography	PET
Principal component analysis	PCA
Propagating surface plasmon resonance	PSPR
Prostate cell line	PNT2
Resonance Raman scattering	RRS
Revolutions per minute	RPM
Scanning electron microscopy	SEM
Silver nanoparticle	AgNP
Spatially offset Raman spectroscopy	SORS
Sum frequency generational vibrational spectroscopy	SFG-VS
Surface enhanced Raman spectroscopy	SERS

Surface enhanced resonance Raman spectroscopy	SERRS
Surface enhanced spatially offset Raman spectroscopy	SESORS
Surface plasmon resonance	SPR
Ultraviolet	UV

Contents

1. General Introduction

In 1959, Richard Feynman delivered a seminar entitled "There is Plenty of Room at the Bottom an Invitation to Enter a New Field of Physics" introducing the first concepts of nanotechnology, describing how many biological problems could be solved on the atomic scale.[1] Since this innovative seminar, there have been many reports of the use of nanotechnology, specifically the use of nanoparticles, in biotechnology,[2] catalysis and materials science,[3] to cancer diagnostics[4] and even in defence and military.[5]

1.1. Nanoparticles

A nanoparticle (NP) can be defined as a particle with at least one dimension measuring less than 100 nanometres (nm) that demonstrate unique chemical, electrical and optical properties not found in bulk samples of the same material.[6] They can be made from many different materials, including but not limited to: gold,[7] silver,[8] copper,[9] iron[10] and silica.[11] NPs have been used unknowingly for millennia, a historic and interesting example of this is the Lycurgus cup, shown in Figure 1,[12] which dates back to the 4th century; the glass appears a different colour depending on how it is exposed to light due to the gold and silver NPs embedded in the glass. In the daylight (reflected light) the cup appears green, however when illuminated from the inside (transmitted light) the cup appears a deep red colour.

Figure 1 - The Lycurgus cup exhibiting a green colour in reflected light and a red colour in transmitted light.[12]

Saggiomo and co-workers have recently created a modern version of the Lycurgus cup by embedding gold NPs in a polymer filament that was then 3D printed into a similarly shaped chalice to that of the Lycurgus cup, exhibiting a purple colour in transmitted light and an orange-brown colour in reflected light.[13] It is hoped that in addition to being of great use to artist and sculptors, this technology will provide further grounds to aid the study of the optical properties of nanoparticles.

1.1.1. Gold Nanoparticles

Gold nanoparticles (AuNPs) have been utilised extensively in many biological and electronic applications due to their impressive chemical, optical and physical properties as well as the fact they are relatively non-toxic compared to the toxicity of copper nanoparticles (CuNPs), for example.[14,15] Due to their notable ability to scatter light, AuNPs have been utilised in many surface enhanced Raman spectroscopy (SERS) applications.[16] The synthesis of AuNPs is not only limited to solid spheres, there has been an abundance of research over the years dedicated to the synthesis of varying shapes of AuNP and how this influences their unique properties. Shells,[17] rods,[18] cubes,[19] cages,[20] clusters[21] and stars[22] have all emerged over the years and can be tailored to match the needs of a variety of applications.

1.1.2. Nanoparticle Synthesis

The majority of NP synthesis involves the reduction of a metal salt by a reducing agent; most commonly used reducing agents include sodium citrate,[7,23] ethylenediaminetetraacetic acid (EDTA)[24] and sodium borohydride.[25] In 1857, synthesis of AuNPs was reported by Michael Faraday, here AuNPs were synthesised by reducing chloroauric acid by use of white phosphorous.[26] Studying the differences between this AuNP solution and that of bulk gold is what formed the basis for metallic NP research today.

Since then, many synthetic methodologies have been reported, the most popular originating from Turkevich in 1951,[7] then modified by Frens in 1973.[23] This synthesis generally proceeds over three phases: nucleation, growth and coagulation, as shown in Figure 2. During nucleation, the metal ions are reduced and small clusters form. It is these small clusters that come together, during the growth phase, to form larger particles. Coagulation is generally regarded as the most important stage as it is here that the size and shape of the particles is controlled. Less stabilising agent produces larger particles with absence of coagulation at the end of the reaction ensuring stability.

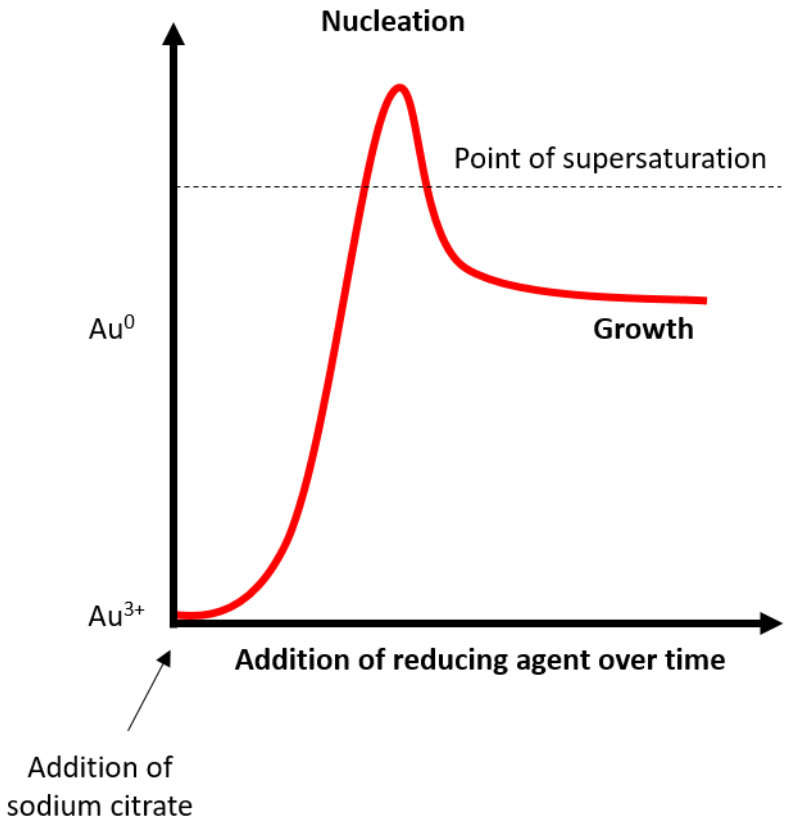

Figure 2 – Nanoparticle growth diagram.

The resulting NPs are generally referred to as colloid or sols. The Turkevich method generally yields AuNPs of approximately 20 – 60 nm in size with an average extinction of 520 nm, however, synthesising larger particles *via* this method becomes difficult. Monodispersity decreases and the overall shape and size of the particles becomes inconsistent.[27] These inconsistencies have led to a number of seed mediated growth protocols, for larger particles, becoming established, a few of which are discussed below.

Perrault *et al.* proposed a synthetic route yielding spherical AuNPs up to approximately 200 nm in size that retain the monodispersity and spherical qualities achieved using the Turkevich method for smaller particles.[28] Here, small gold seed NPs (~ 20 nm in size) are synthesised and grown to the required NP size by reducing gold onto their surface. For larger particles approximately 100 - 200 nm in size, using sodium citrate as the reducing agent would cause

smaller secondary particles to be produced with a chance of aggregation, as there would not be enough sodium citrate to fully coat and stabilise the particles. Perrault recommend the use of hydroquinone as the reducing agent due to its weak reduction potential and the capability to selectively reduce gold onto the AuNP seeds when they are in close proximity to each other.[28,29]

Another method has been reported by Puntes *et al.* who demonstrated a kinetically controlled mechanism for the growth of AuNPs up to 200 nm in size, that possessed good monodispersity, and yielded a high concentration of NPs.[30] This is achieved by the reduction of chloroauric acid by sodium citrate to create small seed NPs approximately 30 nm in size. These seeds are then grown into larger NPs by the reduction of sodium citrate into the seed particles using ascorbic acid (AA). These NPs were then further stabilised with a cetyl-trimethylammonium bromide (CTAB) layer. Despite this yielding excellently stable NPs, care must be taken when considering NP surface chemistry as the capping agent or stabilising layer will greatly affect any analyte molecule surface interaction and particle biocompatibility.[31] CTAB is notoriously difficult to displace from the metal surface, often hindering surface functionalisation of analyte molecules of interest and is known to have a toxic effect *in vitro.*[32,33] Therefore, CTAB capped particles may be unsuitable for bio applications unless the CTAB layer was to be coated in a chemical layer stable enough to prevent the CTAB leaching from the surface.[34] Polyethylene glycol (PEG) has become a popular NP stabilising agent over the years due to its ease of use and biocompatibility.[35] Use of polymers as NP stabilising agents has become increasingly attractive due to the ability of the polymer to not only stabilise the NPs in solution,[36,35] but because of the unique characteristics some polymers possess making them particularly interesting for bio-chemical applications.[37] Great stability is not the only advantageous characteristic of polymer coated nanoparticles, engineered biodegradability of a nanoparticle polymer coatings has been exploited in order to create new methods of localised drug delivery.[38]

Additionally, work conducted by the group has shown the ability to create polymer coated gold nanoparticles capable of switching their SERS response on

and off depending on the temperature the nanotag reaches upon laser excitation. At temperatures greater than 32°C, the polymer chains coating the nanoparticle would 'collapse' becoming coiled and disordered, bringing the Raman reporter molecule closer to the nanoparticle surface, thus achieving a SERS response. Cooling this nanotag resulted in the opposite effect where the polymer chains would become swollen and rigid therefore removing the reporter molecule from close proximity to the NP surface 'switching off' the SERS response.[39]

1.1.3. Optical Properties of Nanoparticles

Metallic NPs possess an electron cloud on the surface, which when oscillating is referred to as the surface plasmon. The oscillation frequency differs depending on the size, shape, metal type, interparticle distance and dielectric environment of the particle. When light is directed at the NP solution, the oscillation amplitude increases. The wavelength were this oscillation reaches its maximum is referred to as the surface plasmon resonance (SPR)[40] as shown in Figure 3. Two types of surface plasmon resonance exist: the localised surface plasmon (LSPR) and the propagating surface plasmon (PSPR).

Propagating surface plasmon occurs on thin planar metallic surfaces, whereas localised surface plasmon resonance is observed in metallic particles with nanoscale characteristics (< 100 nm).[41] As this work described in this thesis employs the use of metallic nanoparticles, only the LSPR will be discussed in this thesis introduction.

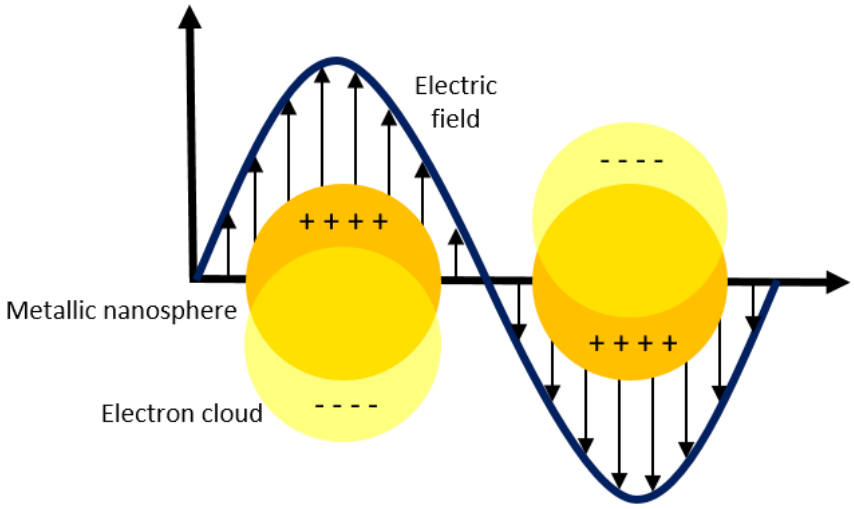

Figure 3 - Schematic illustrating the oscillation of electrons in solid metallic nanospheres under the influence of an electromagnetic field.

This absorption and scattering of light by electrons is described as "Mie Theory" first reported by Gustav Mie in 1908.[42,43] Specifically, it can be used to aid the description of the LSPR and other properties in AuNPs due to the collective oscillation of free electrons in the conductance band. For small solid nanospheres, the LSPR is influenced by multiple factors. The material of the NP greatly affects position of the LSPR; for example, solid spherical AuNPs tend to have a LSPR in the approximate region of 520 – 560 nm,[44] whereas solid spherical silver NPs (AgNPs) have an LSPR of approximately 405 – 420 nm.[45] An increase in NP size and therefore an increase in surface area will lead to a red shift of the LSPR.[46] This is illustrated in Figure 4.

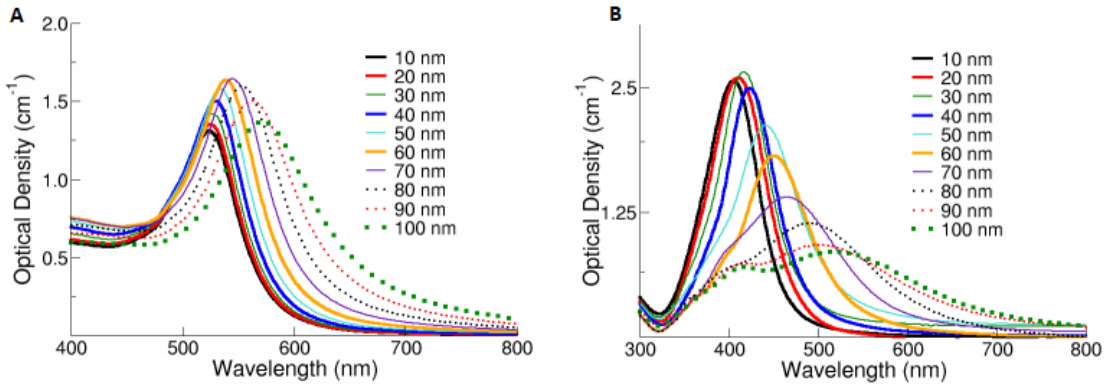

Figure 4 – Extinction spectra describing the LSPR position of (A) solid gold nanospheres 10 - 100 nm and (B) solid silver nanospheres 10 - 100 nm.[47,48]

NP shape also heavily influences the LSPR; for example, the arm length of gold nanostars (AuNS)[49,50] and the overall length of gold nanorods (AuNRs)[51] determine the extent of the LSPR shift. In addition, the dielectric constant of the medium surrounding the NPs, often due to surface functionalisation and modification, is also an important consideration when determining the position of the LSPR. For example, functionalisation of a biomolecule onto the surface of a NP results in a change of the refractive index of the surrounding medium and therefore the resonance condition of the LSPR is affected resulting in a plasmon shift.[52] This is a useful tool to confirm successful NP functionalisation.

The use of LSPR is most commonly exploited for use in biosensing.[53] An example of this is the formation of NP dimers in the detection of specific of DNA. When a DNA probe binds to its complementary DNA strand, aggregation will occur causing a change in the extinction profile of the NPs which can be measured spectroscopically; *via* UV-Visible extinction spectroscopy.[54] Scholfield *et al.* have shown the ability to colourimetrically detect the cholera toxin by use of LSPR monitoring. Glyconanoparticles, carbohydrate functionalised NPs, were developed which aggregated and red-shift upon the presence of this toxin with the degree of the red-shift exhibiting a concentration dependence.[55]

1.1.4. Tuning the Localised Surface Plasmon Resonance

Synthesising NPs in a multitude of shapes and from a variety of different materials is not the only way to control the LSPR of the particle. Controlling specific growth parameters during the synthesis of nanoparticles allows tight control over their LSPR. The LSPR of hollow gold nanoshells (HGNs) can be easily manipulated by controlling the thickness of the shell and the diameter of the internal particle cavity. Decreasing the shell thickness and therefore increasing the cavity size generally results in a red shift in the LSPR. This is achieved by varying the ratio of $HAuCl_4$ and its reductants.[17,56] The LSPR of gold nanorods (AuNRs) can also be controlled by carefully varying some of the experimental parameters during the growth phase. AuNRs possess two LSPR modes: the transverse band and the longitudinal band, corresponding to the short axis and long axis on the nanorods respectively.[57] Increasing the length of the nanorod and decreasing its overall thickness generally leads to a red-shift in the LSPR.[58] Gold nanostars (AuNS) have attracted a lot of attention in recent years due to their excellent performance in surface enhanced Raman applications and the ability to tune the LSPR by controlling a number of factors during synthesis. Varying the length of the star arm and its morphology both have an effect on the position of the LSPR. Increasing the arm length and the overall arm sharpness exhibit more a more red-shifted LSPR.[59]

1.2. Raman Spectroscopy

Spectroscopies are extensively used to provide us with information about the molecular structure of a sample by exploiting one of the three ways in which light interacts with matter: absorption, emission or scattering. In Raman spectroscopy, the focus is on how molecules scatter light, more specifically, the inelastic scattering of monochromatic light.

Raman scattering was first witnessed experimentally by Sir Chandrasekhara Venkata Raman and Kariamanickam Srinivasa in 1928[60] following on from the idea proposed by Adolf Smekal in 1928.[61] Since the discovery of the laser in 1957, Raman spectroscopy has advanced significantly and is now considered a

complementary technique to infrared (IR) spectroscopy. Today, Raman spectroscopy has become an incredibly useful tool with modern advances in instrumentation allowing the translation of Raman spectroscopy into the field with handheld instrumentation becoming increasingly popular in recent years.[62] Further advances in Raman spectroscopy have led to the advent of techniques such as surface enhanced Raman spectroscopy (SERS) and surface enhanced resonance Raman spectroscopy (SERRS) which have become incredibly valuable and functional techniques for a multitude of applications including bio-sensing,[63] cancer and disease diagnostics[4] and has even been applied in security[5] and explosives detection.[64]

1.2.1. The Theory of Raman Scattering

For a molecule to be Raman active, it must be polarisable. When a Raman active molecule is excited by photons of light, a dipole is induced and the electron cloud is distorted – this is referred to as the 'virtual' state. The molecule only remains in this excited 'virtual' state for a temporary period of time, after which it relaxes and returns to the electronic ground state. It is during this relaxation process that scattering of light occurs.[65]

Three scattering processes can occur; Rayleigh scattering, Stokes scattering and anti-Stokes scattering as shown in the Jablonski diagram in Figure 5.

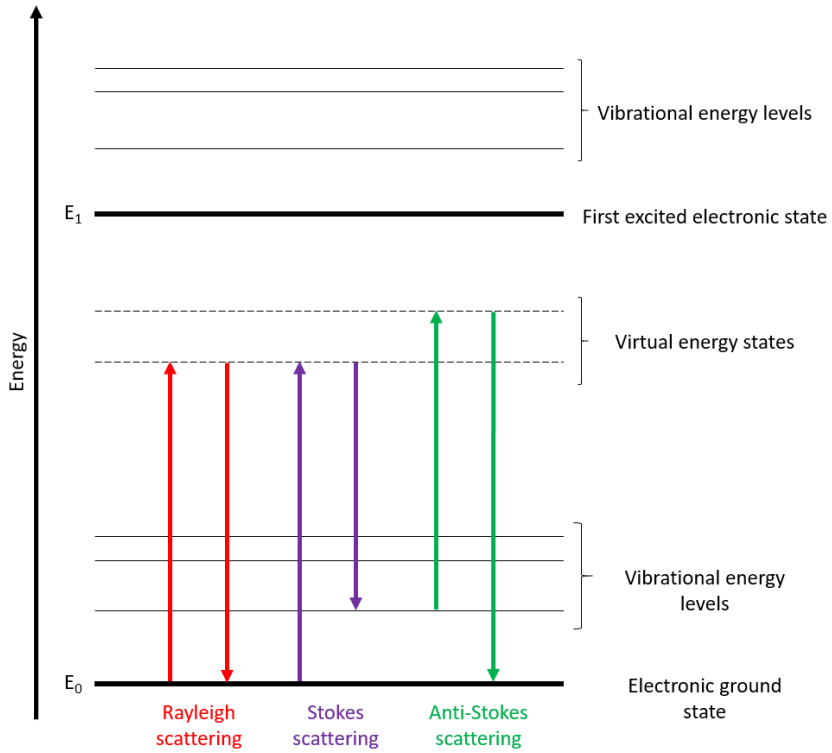

Figure 5 - Jablonski diagram illustrating the Raman (Stokes and anti-Stokes) and Rayleigh scattering processes.[65]

The majority of molecules undergo Rayleigh scattering, an elastic process. Here, the incident and scattered light have the same frequency and the molecule returns to its ground electronic state. There is no change in energy between the incident light and the scattered light therefore the energy of the molecule remains the same as it was prior to excitation.

Raman scattering is an inelastic process: there is a difference in energy between the incident and scattered light. There are two different processes by which this can occur: Stokes scattering and anti-Stokes scattering. When a molecule is excited by photons of light and returns to an excited vibrational ground state higher in energy than that of the vibrational ground state this is termed Stokes scattering. Anti-stokes scattering occurs when the molecule already resides in an excited vibrational energy level then relaxing to the electronic ground state[66] as shown in Figure 5.

The difference in energy between the initial and final vibrational levels (v) is referred to as the Raman shift and given in wavenumbers (cm^{-1}). It can be calculated as shown in Equation 1 where λ represents the wavelength of the incident and scattered photons.[67]

$$v = \frac{1}{\lambda \text{ incident}} - \frac{1}{\lambda \text{ scattered}}$$

Equation 1

At room temperature, the majority of molecules exist in the ground vibrational state, the population of which can be calculated by using the Boltzmann equation, (Equation 2), where N_1 is the number of molecules in the excited vibrational energy level, N_0 is the number of molecules in the ground vibrational energy level, g is the degeneracy of the energy levels, ΔE is the difference in energy between the vibrational energy levels, k is the Boltzmann constant (1.3807×10^{-23} JK^{-1}) and T is the temperature (K). Stokes scattering is likely to be much more intense, as more molecules reside in the ground state at room temperature, than anti-Stokes scattering and is more commonly measured in Raman spectroscopy.[65]

$$\frac{N_1}{N_0} = \frac{g_1}{g_0} \exp\left(\frac{-\Delta E}{kT}\right)$$

Equation 2 – The Boltzmann distribution equation.

A disadvantage of Raman scattering is that it is a relatively weak process with only one in every 10^6 – 10^8 photons being Raman scattered.[68] The intensity of Raman scattering can be described in Equation 3, where I is the Raman intensity, K is a constant, I_L is the power of the laser, α is the polarizability and v is the frequency.

$$I = KI_L\alpha^2 v^4$$

Equation 3 - The intensity of Raman scattering.

As the intensity is proportional to the fourth power of the frequency, the Raman intensity can be improved by use of shorter excitation wavelengths.[69] However, shorter excitation wavelengths can often create issues with sample burning and sample degradation as most molecules absorb light at these wavelengths. The advent and development of techniques such as resonance Raman scattering and surface enhanced Raman scattering has allowed increase of these generally weak signals without the sample burning and degradation that often occurs at shorter excitation wavelengths.[65]

1.2.2. Resonance Raman spectroscopy

The sensitivity of Raman scattering can be increased by tuning the laser excitation wavelength to the frequency of an electronic transition within the analyte molecule. Generally, signal enhancements of up to 10^4 are reported when compared with conventional Raman scattering.[70] Resonance Raman scattering (RRS) differs from Raman as with Raman scattering the molecule is excited to a virtual energy state, whereas resonance Raman scattering results in the excitation of the molecule to an excited vibronic state within the first electronic state as shown in the Jablonski diagram in Figure 6. This can allow a more intense spectrum to be acquired and is advantageous when analysing complex sample matrices. There are however, a few problems associated with resonance Raman, in particular interfering fluorescent background due to the inevitable absorption that occurs alongside resonance Raman scattering.

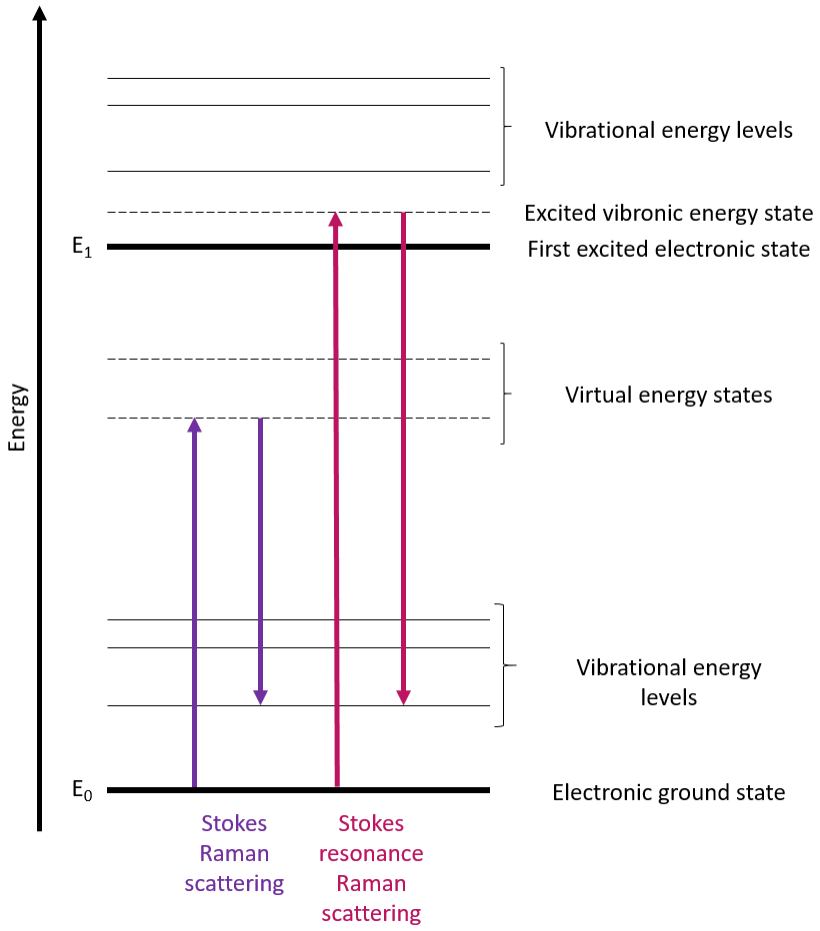

Figure 6 - Jablonski diagram illustrating the Stokes Raman and Stokes resonance Raman scattering processes.

RRS also has some problems with sample degradation, as most molecules absorb light at these wavelengths, and competing electronic processes such as fluorescence can still occur and can obscure Raman peaks of interest.[71] This can be avoided due to the timescale of each event; fluorescence typically occurs over nanoseconds whereas Raman is concluded in picoseconds. Pulsed lasers can be used to separate these events due to the timescale in which they occur on, therefore minimising the amount of fluorescence observed.[72] Additionally, the use of NPs has been shown to quench the fluorescent background and has led to the popular use of surface enhanced Raman spectroscopy.[73]

1.2.3. Surface Enhanced Raman Spectroscopy

First discovered by Fleischmann *et al.* in 1974, SERS was observed by adsorbing pyridine molecules onto a roughened silver electrode and studying their behaviour. It was realised that by doing so, the Raman signal increased drastically, 10^6 times compared to that of the Raman signal of liquid pyridine.[74] This increase in sensitivity had even lead to the ability to detect single molecules.[75] The use and popularity of SERS has increased in recent years, with the technique being applied in a multitude of areas. Docherty *et al.* have employed SERS in the detection of toxic metals by use of salen complex formation. Detection of nickel, copper, cobalt and manganese ions, in water samples, was achieved by measuring the SERS response of the salen-metal complex formed. Each complex provided a unique SERS spectrum therefore allowing discrimination between each of the metal ions in both environmental and synthetic metal ion doped water samples.[76] SERS has been shown a useful tool for the detection of a large number of biomarkers relating to various cancers, infections and diseases. Gracie *et al.* reported the use of SERS for the detection and quantification of three different bacterial meningitis strains, in a multiplexed setting, by use of SERS. Silver NPs were functionalised with different DNA probes and three different Raman reporter molecules, that would hybridise on contact with the complementary DNA of the target allowing SERS spectra to be obtained, each corresponding to each of the three strains of meningitis analysed. As each Raman reporter molecule provided a unique SERS spectrum, differentiation and detection of each strain in a mixed sample was achieved. This ability to multiplex and quantify the different pathogens present using a simple technique like SERS, is extremely desirable in a clinical diagnostic setting.[77]

1.2.4. SERS Enhancement

Two main theories have emerged as to why there is such great enhancement with SERS. Albrecht and Creighton proposed the charge-transfer effect[78] whereas Jeanmarie and Van Duyne proposed the electromagnetic effect[79] as the main reasoning for the SERS enhancement.

1.2.4.1. The Electromagnetic Effect

The electromagnetic enhancement effect is argued to be the more dominant process contributing to SERS enhancement. The electromagnetic effect occurs when the surface plasmons of metallic NPs are excited by the incident laser light causing electron oscillation to occur perpendicular to the metal surface, therefore enhancing the electric field experienced by the analyte molecule. It is this increase in electric field that results in an increase in polarisation and therefore an increase in the intensity of Raman scattering observed.[80] This enhancement effect is even greater when the NPs are in close proximity to each other. The surface plasmons of each NP are able to interact with each other creating large regions of electric field between the particles resulting in a greater SERS enhancement. This phenomenon is termed SERS 'hotspots'.[81,82]

1.2.4.2. The Charge-Transfer (or Chemical) Effect

The charge-transfer or chemical effect also leads to the SERS enhancement, albeit to a much smaller degree than the electromagnetic effect. Here, a chemical bond forms between the metal surface and the analyte molecule resulting in the formation of a charge-transfer complex allowing the charge-transfer of electrons and holes. This in turn results in the formation of new electronic states creating a new state resonant with that of the laser excitation wavelength, increasing the polarisation of the molecule and therefore increasing the intensity of Raman scattering.[83]

It is generally accepted across the scientific community that SERS enhancement is due to a combination of both the electromagnetic and charge transfer effects.

Lombardi *et al.* published a 'unified expression' for the enhancement in order to combine the electromagnetic and charge transfer effects whilst also taking resonance from the analyte molecule into consideration. This merged all three effects allowing the parameters controlling the degree of contribution of each

effect to be identified and provided an approach for the experimental determination of each of these contributions.[84] Lombardi placed emphasis on the importance of the analyte molecule in the unified expression of SERS and this resonance enhancement in combination with a roughened metal surface is known as surface enhanced resonance Raman spectroscopy (SERRS).

1.2.5. Surface Enhanced Resonance Raman Spectroscopy

SERRS, an advancement of SERS, was first presented by Stacy and Van Duyne in 1983 describing that a signal enhancement of approximately 10^{14} orders of magnitude can be achieved when the laser excitation wavelength coincides or is close to that of the absorbance maxima of the analyte molecule.[85,86] An even greater signal enhancement can be achieved by similarly matching this laser excitation wavelength with the resonant frequency of the metal surface plasmons within the NP.[87,88] SERRS provides many advantages over conventional Raman spectroscopy, firstly the use of metallic NPs have the ability to quench fluorescent interference in the sample and therefore the fluorescent background is greatly reduced allowing for fluorescent and non-fluorescent dyes to be used. Sample degradation and burning can also be avoided as lower laser powers and shorter accumulation times can be used.[72] Additionally, by using multiple analyte molecules with varying resonance frequencies, multiple laser excitation wavelengths can be used to achieve multiplexed detection.[89] For example, Faulds and co-workers reported an excellent multiplexed detection of six different DNA sequences corresponding to different strains of Escherichia coli bacterium *via* the use of six commercially available dye labels.[90]

1.2.6. Near-Infrared Raman Spectroscopy

Most reports of near-infrared (NIR) Raman spectroscopy employ the use of a 785 nm laser excitation and this has demonstrated fruitful applications in many areas such as cell imaging, cancer diagnostics and blood analysis.[91] It is of considerable interest to many spectroscopists and medical professionals to further advance longer wavelengths in which efficient SERS can be achieved as the absorption of light of many biomolecules is minimised as we move towards

these longer wavelengths.[92] This could lead to an ease in signal acquisitions from biological samples, as less background signal would be observed resulting in a lesser need for complicated data processing to remove large backgrounds from these biological samples.

Recently, we have witnessed the emergence of SERS applications, which employ the use of laser excitation wavelengths greater than 1000 nm. Kearns et al. demonstrated superb SERS response with nanotags consisting of hollow gold nanoparticles (HGNs), functionalised with a host of commercially available Raman reporters with a laser excitation wavelength of 1064 nm.[93] This was advanced with an intense SERS response achieved by the combination of a novel class of chalcogenopyrylium based chromophores (expanded upon in section 1.3) with 1280 and 1550 nm laser excitations.[94,95]

1.2.7. Raman Imaging

Raman imaging or Raman mapping is used in order to produce detailed images from the Raman spectrum of a sample. The spectrometer laser is scanned over a pre-selected area collecting a spectrum at each step point, this then allows false colour images to be created displaying the distribution of intensity of a specific vibration, or reference spectrum over the area imaged. This is typically presented as a 'heat map' where pixels are assigned a colour corresponding to their intensity over a selected colour range. Raman imaging has been exploited over a wide variety of applications. It has been used to image the differing components of cells and tissues,[96,97] the detection and distribution of an active pharmaceutical ingredient within drug samples[98] and even in the analysis of artwork pigments and materials for authenticity.[99]

1.3. Chalcogenopyrylium Dyes

As each chapter of this thesis employs the use of a novel class of chalcogenopyrylium (CP) dye molecules as Raman reporter molecules, this thesis would not be complete without providing them with a suitable introduction. A general structure of these dye molecules is shown in Figure 7. They consist of two

cationic, six-membered heterocyclic rings containing a chalcogen atom, X = S or Se, with R_1 – R_4 representing different aromatic or aliphatic substituents. The methine backbone of the molecule can also be extended from a monomethine (n = 0) to a trimethine (n = 1) and to a pentamethine (n = 2) dye.

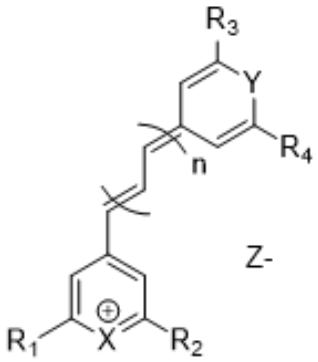

Figure 7 - General chemical structure of a polymethine pyrylium dye, where X and Y represent chalcogen atoms (generally sulphur or selenium), R_1 - R_4 are aliphatic and aromatic substituents, Z is the counterion and n = 0, 1 or 2.

Prior to use in SERS, these dyes were initially designed for application as photosensitisers in the electrophotographic industry.[100] They have also been employed in the photodynamic therapy of cancers,[101] modulation of p-glycoprotein[102] and in the immunisation of blood borne pathogens.[103] The ability to easily manipulate the light absorption maxima of these dyes has made them particularly attractive for use in red-shifted SE(R)RS applications, particularly at excitation wavelengths greater than 1000 nm.

Controlling the light absorption maxima (λ_{max}) of these chromophores can be accomplished in different ways. Firstly, extending the backbone of the molecule from a monomethine, to a trimethine or pentamethine dye results in a red-shift of approximately 100 nm for every two-carbon addition.[104] Secondly, switching the heteroatom in the main body of the molecule will also lead to control of the λ_{max}. As the chalcogen atom size increases down group 16 (O < S < Se < Te), the energy of the highest occupied molecular orbital (HOMO) becomes less negative and the energy of the lowest unoccupied molecular orbital (LUMO) becomes less positive and consequently a red-shift of the molecule occurs.[105] Varying the

heteroatom can be used to tune the λ_{max}, allowing these dyes to be tailored to absorb light from the visible region into the NIR region and are therefore excellent candidates for use in SE(R)RS. Z is the counterion and can be Cl^-, Br^-, ClO_4^- or PF_6^- depending on dye application. The counterion has no observable effect on the dye absorption maxima, the Raman shift in SERS measurements is also unaffected with the exception of the chloride counter ion. The PF_6^- counterion is known to have the lowest or no negative effect on the stability of the colloidal solution when synthesising nanotags and it is for this reason that dye molecules stabilised with a PF_6^- counterion are preferentially used throughout this thesis.[106]

Additionally, these molecules can also be modified with functional groups fit for specific purposes, an example of which, used in this thesis, is an alkyne moiety. Expanded upon in section 6.1.2.3, alkyne functionality is often exploited in Raman and SERS due to the appearance of the characteristic alkyne peak in the cellular Raman silent region of the spectrum (1800 – 2800 cm^{-1}) allowing biological background free detection of alkyne containing nanotags.[107,108]

2. Thesis Aims

The overall aim of this thesis was to develop red-shifted nanotags that could be detected using SERS, in particular by use of a 1280 nm laser excitation source. More specifically, this was to be achieved by exploiting the light scattering properties of large gold nanoparticles and the intense Raman response of an emerging class of chalcogenopyrylium (CP) dye molecules.

Previous group work deduced the binding orientation of one of these CP dye molecules on hollow gold nanoshells (HGNs). However, in order to aid future design of these CP dye based nanotags for specific use, differing binding anchors and orientations in relation to SERS response should be investigated. Chapter 3 of this thesis aims to examine the nanotag SERS response in relation to the calculated binding angle of five CP dye molecules with binding angles over the range of 0° – 85°.

There is requirement for novel methodology for the labelling and tagging of various items in order to prevent counterfeiting of goods. The aim of chapter 4 of this thesis was to investigate how these CP dyes can be used to create wavelength selective nanotags for invisible tagging and detection. This chapter aims to explore the ability of these nanotags to provide intense SERS response at 1280 nm laser excitation while remaining transparent at 785 nm excitation, creating the ability to selectively tag and detect items of interest.

Chapter 5 of this thesis investigates the depth of penetration of three conventional hand held Raman spectrometers: 785, 1064 and 1280 nm, fitted with a point and shoot adaptor. Firstly, this chapter aims to examine the ability of these instruments to probe through a tissue barrier of increasing thickness, and detect a CP based nanotag, as it is known the absorption and scattering of light in biological media is minimised at longer wavelengths. An additional objective of this chapter was to explore the ability of each spectrometer to probe though a plastic barrier, of increasing thickness, in order to determine if the resonance of

the excitation wavelength and CP based nanotag affected the depth at which these nanotags could be detected.

These CP based nanotags have already been employed in biological systems, however their cytotoxicity is currently unknown. The aim of chapter 6 of this thesis was to investigate the toxicity and detectability by SERS of these CP based nanotags, in cells. Additionally, this chapter aims to ascertain whether addition of an alkyne moiety to the CP dyes would be beneficial for biological SERS applications.

3. CP Dye Binding Angles: A Study of the Effect of Orientation on SERS Response

3.1. Introduction

It has been theoretically shown that the magnitude of the local electric field of a nanoparticle can vary significantly over the space of a few nanometres, and so the SERS response of the analyte molecules functionalised onto the surface of nanoparticles will be affected depending on the spatial arrangement they assume.[109] Therefore the way in which an analyte is orientated onto a metallic nanoparticle surface can greatly affect the SERS response obtained. An insight into how this new class of chalcogenopyrylium molecules bind to the nanoparticle surface would provide valuable information in the future design of chalcogenopyrylium based nanotags for SE(R)RS applications.

It is known that by changing the concentration, and thus the packing density, of molecules on a nanoparticle surface that the orientation of said molecules can be altered. MacDonald and Smith described how increasing the packing density of cytochrome *c* on hexagonal silver nanoparticles can re-orientate the molecule from an almost planar to a more vertical orientation, observable by changes in the relative peak intensities in the acquired SERRS spectra.[110] Zhang *et al.* demonstrated the importance of nanoparticle-molecule orientation in the SERS response of various alkanoic acids functionalised onto silver nanoparticles, in particular the effect on the SERS intensity and presence, or absence, of vibrations corresponding to the modes of the phenyl ring. It was established that if the molecule possessed an odd number of methylene linkers, it would be more likely to bend and assume a *trans* formation on the silver nanoparticle surface with molecules containing an even number of methylene groups assuming a gauche orientation on the AgNPs surface. The authors deduced that this variation in conformation could be attributed to the differing interactions between the pi (π) electrons from the phenyl ring and the interaction of the carboxylic acid with the silver surface. This effect causes visible changes in the Raman spectrum with the

gauche formation resulting in a weaker ring bending mode and stronger C=O vibration than that which is observed by the trans binding molecules. This work concluded that the variation in SERS spectra in relation to variation in molecular orientation is significant enough that great consideration must be taken in the design of chromophores for specific SERS response and application.[111] Michota *et al.* reported that a pH dependence would affect the molecular orientation of 4-mercaptobenzoic acid (4-MBA) on both gold and silver surfaces. It was established that the molecules bind to the metallic surface *via* the sulphur atoms and carboxylate groups and that at acidic pH, the carboxylic acid groups are protonated resulting in a more perpendicular orientation compared to that of the slightly tilted formation that the 4-MBA molecules adopt at lower pH, evident by the relative intensities of the carboxylate bands in the SERS spectrum.[112]

There are many experimental factors that can influence the orientation at which analyte molecules will orientate on metallic surfaces. As this thesis employs the use of chalcogenopyrylium dye molecules for NIR SERS applications, the arrangement of chalcogen based ring systems and their calculated surface-selective sum frequency generational vibrational spectroscopy (SFG-VS) binding angles, in relation to their SERS response, will be discussed herein.

Bedics *et al.* have demonstrated the pronounced optical benefits of this new class of chalcogenopyrylium dyes for use at longer excitation wavelengths, especially their improved SERS signals and detection limits, upon 1280 nm laser excitation, compared with that of previous commercially available reporter molecules.[113] Work has also emerged from these researchers deducing the binding angle and monolayer formation of one of these CP dye molecules (dye 1) on hollow gold nanoshells in an attempt to understand more about the surface layer formed when an analyte is added to the nanoparticle surface.[114] This indicated that the axis of the methine-bridge core of the molecule lies almost perpendicular to the surface plane of the nanoparticle, with SFG-VS deducing a similar orientation with the methine-core of the molecule lying at an angle of 64°-85°. SFG-VS is a technique in which two laser beams overlap at an interface, in this case the gold surface and the dye molecule, generating an output beam which is a sum of the

two incident laser beams which can then be read by a detector. It is then possible to gather information about how a molecule behaves at the interface by studying how it responds to the incident laser beams. SFG-VS is now considered a complementary technique to IR and Raman spectroscopy given its ability to acquire information regarding surface-analyte interactions.[115,116] The SERS spectrum for this molecule was calculated and compared with that of the experimental spectrum allowing for the conclusion that the two selenophene rings rotate inward towards the metal surface allowing these two selenium atoms, in addition to the sulphur atom in the thiophene ring, to directly face the gold surface. Additionally, a space-filled model was created, emphasising that this dye molecule is strongly adsorbed to the surface *via* the selenium and sulphur atoms, with the final proposed surface interaction being between the gold surface and the selenium atoms, as steric hindrance would prevent the sulphur atom from fully reaching the metal surface.[117]

To complement this experimental data, four new CP dye molecules were designed and synthesised with SFG-VS binding orientations calculated over the range 0°- 85°, functionalised onto large solid gold nanospheres and their SERS response, in combination with a 1280 nm excitation wavelength, studied.

3.2. Chapter Aims

The aim of this chapter was to study the SERS response, upon 1280 nm laser excitation, of a novel class of chalcogenopyrylium dye molecules, designed specifically for this study due to the calculated SFG-VS binding angles, in order to ascertain if there was a relationship between the achieved SERS response and the SFG-VS calculated dye binding orientations. By investigating the relationship between SERS response and calculated molecule orientation, it is hoped that in combination with the ability to easily tune these chalcogenopyrylium to the required absorbance maxima (as discussed in section 1.3), this will aid and improve future chalcogenopyrylium dye synthesis and nanotag design for a variety of different SERS applications.

3.3. Results and Discussion

3.3.1. Synthesis of Large Gold Nanoparticles

AuNPs, approximately 100 nm in size, were prepared using a modified Turkevich approach. Chloroauric acid was reduced in the presence of sodium citrate, at a slow stir speed. The resulting colloid was characterised using extinction spectroscopy, dynamic light scattering (DLS), zeta measurements and scanning electron microscopy (SEM) in order to assess stability and applicability for this specific study. The results of the extinction measurements and SEM analysis are shown in Figure 8.

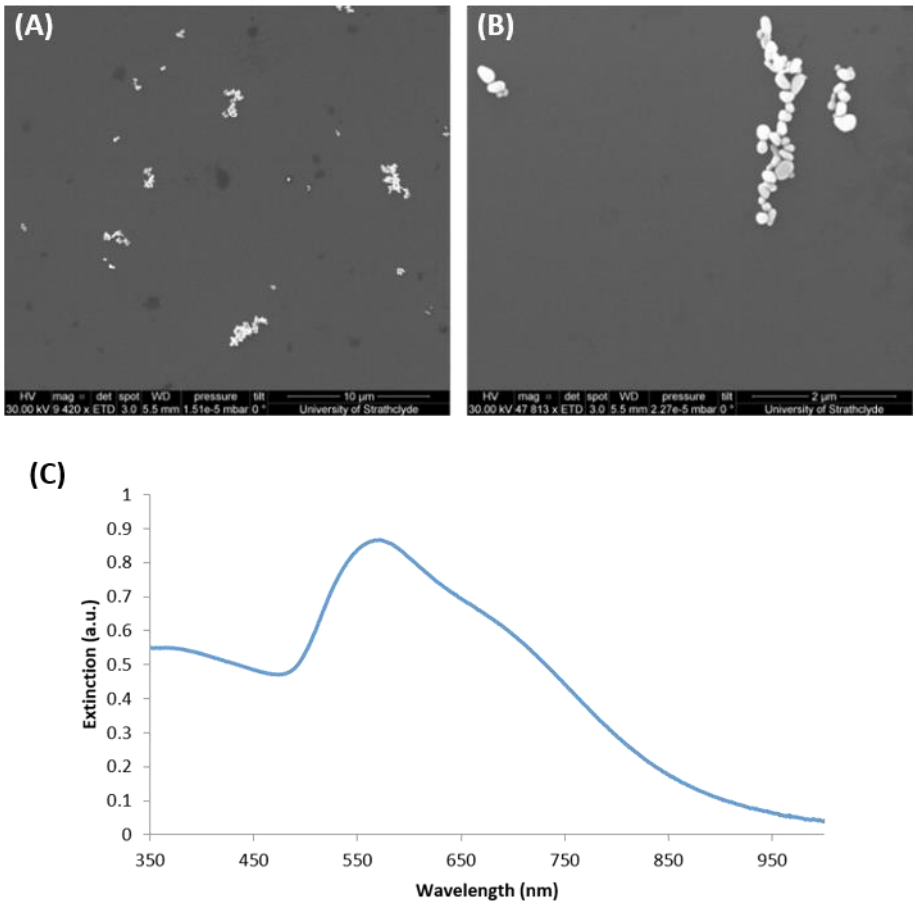

Figure 8 – (A) and (B) SEM images and (C) extinction spectrum of gold nanoparticles used in SERS experiments.

The extinction spectrum of the AuNPs, shown in Figure 8, displays an LSPR of 569 nm, in line with what would be expected of larger sized AuNPs. This LSPR is also slightly broader than would be expected and can be attributed to the method of synthesis; it is acknowledged that rapid stirring should be employed throughout spherical NP synthesis however, if this was conducted, in this particular synthetic route, the resulting colloid would be much smaller in size. At these higher gold and lower citrate concentrations, smaller seed particles tend to form with a chance of aggregation, however the SEM images do not appear to show that any small 'seed' particles have formed and aggregated. It is observed that this nanoparticle extinction profile is somewhat broader than expected and that a sharper extinction profile would indicate better colloidal stability and monodispersity however, it is believed this broad extinction is ultimately the main contributing factor to the SERS intensity achieved, at 1280 nm laser excitation, upon functionalisation with the chalcogenopyrylium (CP) dye molecules mentioned in section 1.3. The CP dyes used throughout this thesis have absorbance maxima values ranging from 780 - 959 nm, which can be considered far enough away from a 1280 nm laser excitation source, that this signal enhancement is not entirely due to a resonance contribution from the dye molecules themselves. Previous work has shown impressive SERS response with these CP dye molecules in conjunction with hollow gold nanoshells, another nanoparticle type that often exhibits a broad extinction profile, particularly so with red-shifted plasmon resonances, and large solid gold nanospheres. Smaller nanoparticle types 20 - 60 nm, with characteristic sharp extinction profiles, were also investigated in these studies however the larger solid nanospheres and the hollow gold nanoshells prevailed as the more impressive SERS substrate with these CP dyes at excitation wavelengths 1280 and 1550 nm.[118,113,94] SEM analysis was carried out to further confirm the size and, to an extent, the degree of monodispersity of the colloid. SEM is a technique that produces an image by scanning the sample with a focused beam of electrons; these electrons interact with atoms in the sample producing secondary electrons that can then be detected. Image J software was then employed to estimate the size of these NPs, this was deemed to be an average size of 134.9 ± 10.8 nm. It should be highlighted

that sizing nanoparticles *via* SEM imaging, in combination with image J software, can often be subjective as this requires the user to visually select, highlight and measure the size of each individual NP and ascertain its size by eye, in which an average NP size is then calculated. The SEM images shown in Figure 8 confirm that these nanoparticles are not perfectly spherical, and contain a small range of sizes, as expected from the broad extinction profile obtained. These images also show some of the AuNPs 'grouping' together indicating the colloid is not as monodispersed as would be favoured, however it should be noted that it is difficult to determine the colloidal monodispersity from an SEM image as the colloidal samples are dried out on a silica wafer and aggregation does occur as a result of this drying process. Dynamic light scattering (DLS) was also employed in order to obtain an average NP size. DLS is a technique which evaluates the hydrodynamic radius of NPs by measuring the Brownian motion and variations in the intensity of the scattered light by the particles in the sample.[119] The NPs were analysed using DLS to determine the average particle size, with the zeta potential then being measured to give the average particle charge.[120] This synthesis yielded NPs of 106.1 ± 5.2 nm in diameter with a zeta potential of -28.5 ± 0.5 mV as determined by DLS and zeta potential measurements. It should be noted that when determining NP stability, zeta potential values under -20 mV are considered stable.[121]

3.3.2. Selection of Chalcogenopyrylium Dye Molecules

Five CP dye molecules were selected for this study by their SFG-VS calculated binding angles in addition to their known ability to provide excellent SERS response upon 1280 nm excitation. Figure 9 shows the chemical structure, light absorption maxima and SFG-VS calculated binding angle of each dye used in this study. Figure 10 depicts the orientation of these dyes on the spherical nanoparticle surface. All dyes were synthesised by Professor Michael Detty's group and all SFG-VS calculations were performed by Dr Luis Velarde's group, both at the University at Buffalo, NY, USA.

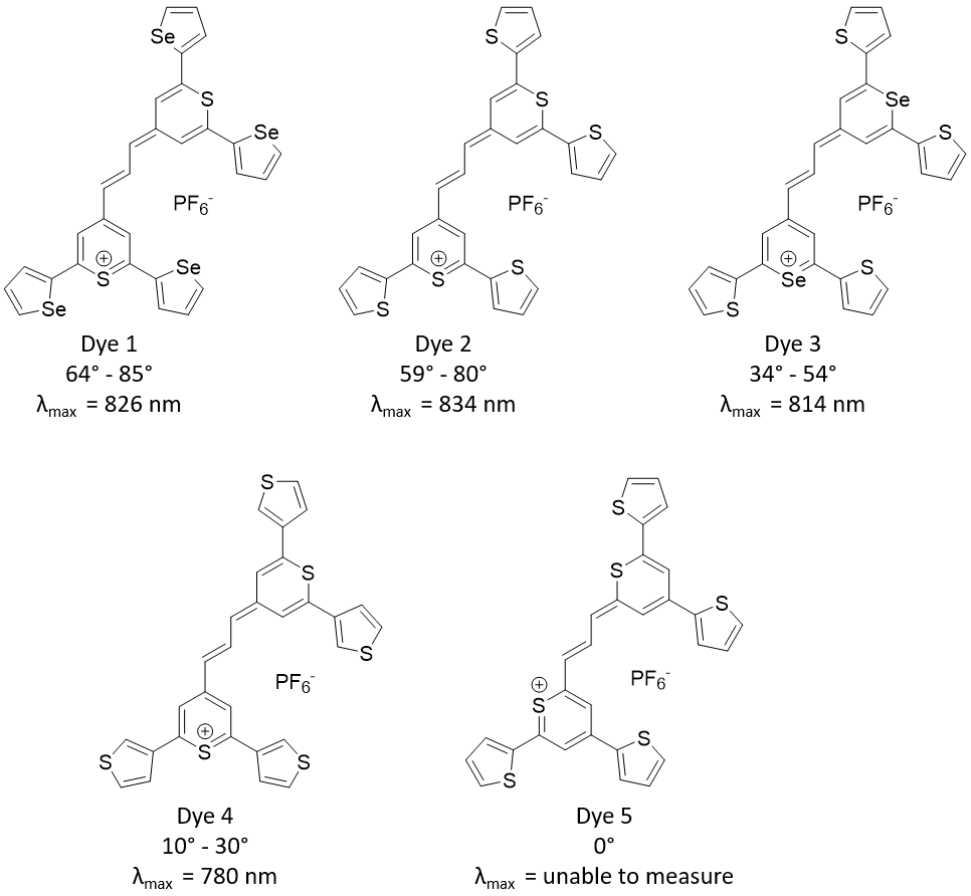

Figure 9 - Chemical structure, SFG-VS calculated binding angles and absorbance maxima (measured in DMF) of five chalcogenopyrylium dyes selected for use in this study.

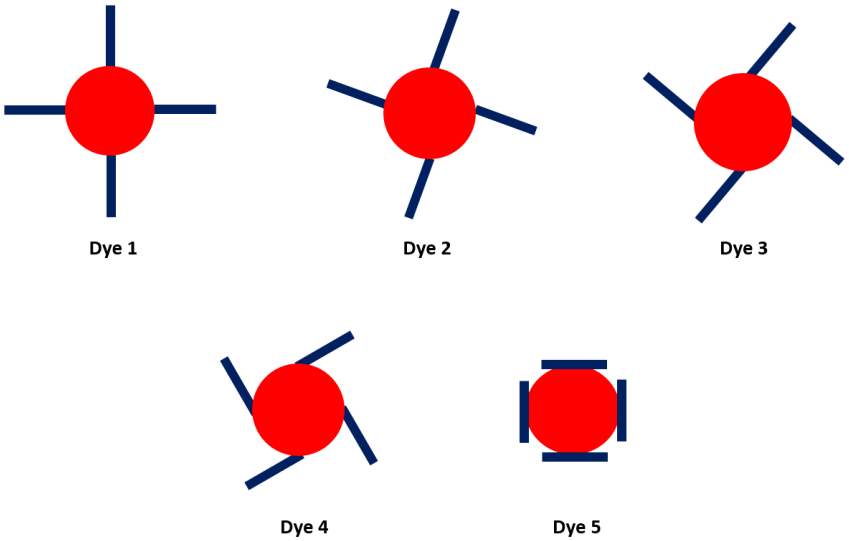

Figure 10 - Cartoon illustrating the binding orientations of dyes 1 - 5 used in this study.

3.3.3. Functionalisation of CP Molecules onto AuNPs

A concentration study (50 nM – 500 nM) of final dye concentration on nanoparticle was carried out in order to deduce the optimal concentration for each nanotag. It should be noted that at concentrations above 500 nM these nanotags would crash out of solution and no SERS signal would be achieved. This optimal concentration is generally regarded to be the concentration at which full monolayer coverage is achieved and thus it is anticipated that the dye molecules will lie in the orientation calculated by SFG-VS at these concentrations. Each dye was added to a nanoparticle sample yielding a final concentration of 50 - 500 nM, shaken for 15 minutes and purified by centrifugation before SERS analysis to ensure no excess free dye remained in the nanoparticle solution.

It should be noted that at this point, Dye 5 was excluded from this study due to its instability in solution despite analysis of multiple batches. This dye produced no SERS response at excitation wavelengths 532 nm – 1280 nm and upon measurement and inspection of the absorption maximum (shown in Figure 11) a poor absorbance spectrum was observed. It is thought this particular dye may possess poor stability and degrade during the shipping process.

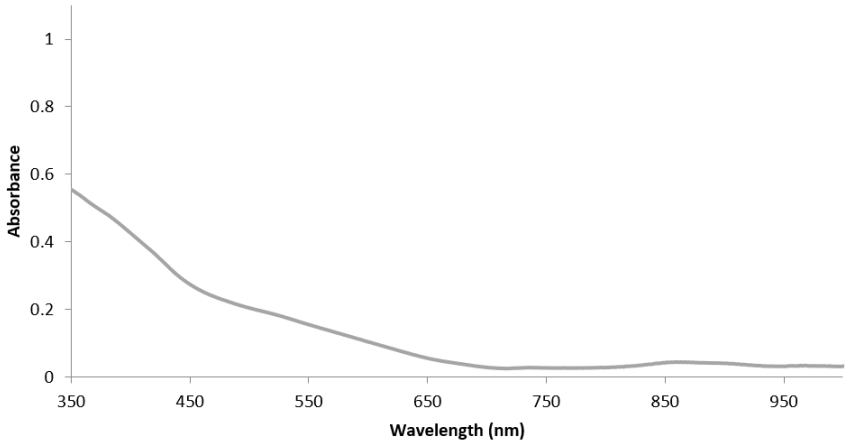

Figure 11 - Absorbance spectrum of dye 5.

3.3.4. 1280 nm SERS response of CP Based Nanotags

SERS measurements were carried out using a Snowy Range portable Raman spectrometer (now Metrohm Raman) fitted with a 1280 nm laser source with a 100 mW laser power. Samples were measured in a vial specifically designed to fit the sample holder of the instrument. Shown below in Figure 12 shows the raw, unprocessed spectra for each nanotag in the concentration range 50 – 500 nM. It is important to highlight that the data is unprocessed as significant spectral information is often lost when data is baseline corrected or when the background is removed; this information is important to retain when attempting to draw a conclusion relating SERS response and predicted orientation. It should also be noted that these nanotag samples were analysed ensuring the time between particle functionalisation, purification by centrifugation and measurement of the SERS response were kept consistent for each concentration and for each dye used.

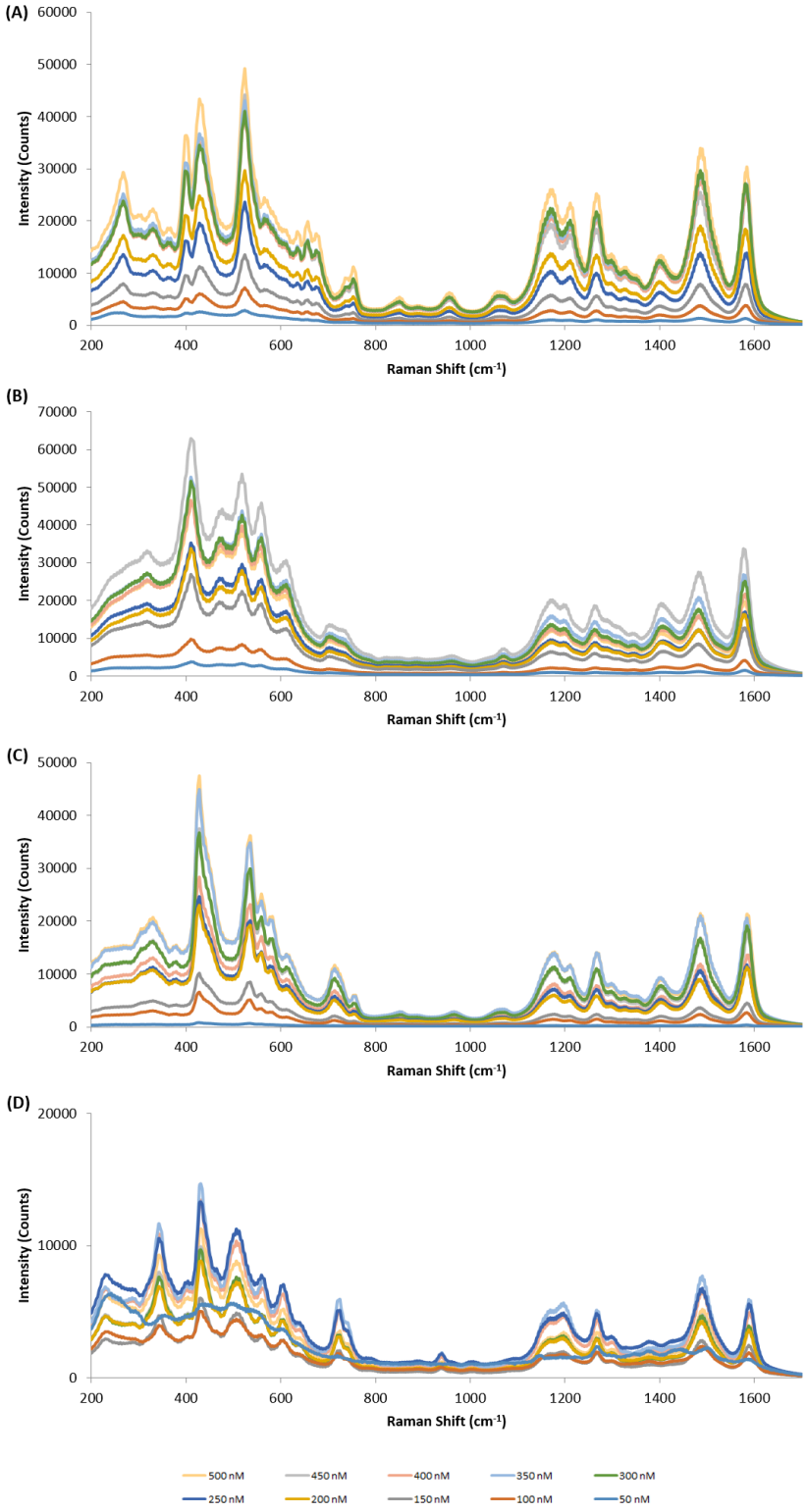

Figure 12 - Raw, average SERS spectra of each CP based nanotag over the concentration range 50 - 500 nM. (A) dye 1, (B) dye 2, (C) dye 3 and (D) dye 4. Measured using a 1280 nm excitation wavelength (100 mW) and an integration time of 3 seconds. Each sample was prepared in triplicate with 3 replicate scans recorded for each sample.

At first glance, the spectra of each chalcogenopyrylium nanotags appear overall, similar. Each exhibits two intense peaks at approximately 1490 cm^{-1} and approximately 1590 cm^{-1}. The Raman shift varies slightly for each dye as highlighted in Table 1. These peaks are highlighted, as they are most intense, they are the most commonly tracked peaks in SERS analysis of these CP dyes.

Table 1 - Summary of the Raman shift of peak A and B for each nanotag.

Dye	Raman Shift peak A (cm^{-1})	Raman shift peak B (cm^{-1})
1	1486	1585
2	1485	1579
3	1486	1584
4	1490	1589

The ~1590 cm^{-1} peak corresponds to the C=C, C-C, C-H and the C-S and C-Se vibrations from the thiopyran and selenopyrylium rings, i.e. the vibration throughout the main body of the molecule. The ~1490 cm^{-1} peak corresponds to that of the molecules core C=C, C-H and the C-C, C-H, C-S and C-Se vibrations from the thiophene and selenophene rings, i.e. the vibration throughout the main body of the molecule with extension to the rings involved in binding to the nanoparticle surface. As these are generally regarded the most intense peaks, these are the peaks typically monitored in SERS measurements and analysis, particularly the ~1590 cm^{-1} peak. The absolute intensity of both peaks, at each concentration for each nanotag is shown in Figure 13 as a bar graph to help visualise determine the optimal concentration for each nanotag and thus the concentration at which full monolayer coverage should occur. The absolute peak intensity was determined by subtraction of the intensity value at the base of the peak from the maximum

intensity value of each peak. The peak base, i.e., the peak minimum, values for all spectra analysed were kept consistent and taken from the Raman shift at 1430 cm^{-1} for peak A and 1550 cm^{-1} for peak B.

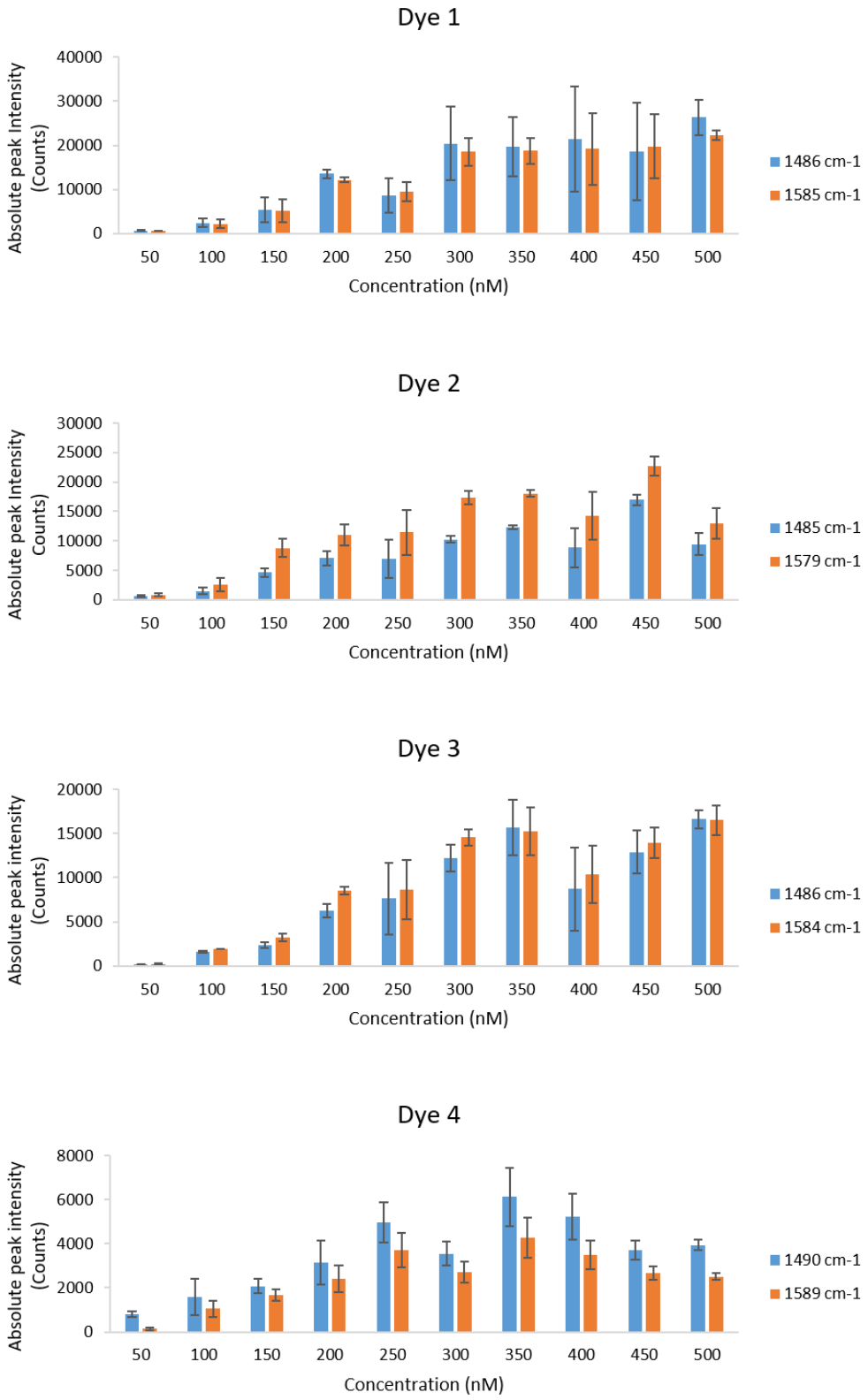

Figure 13 - Average absolute peak intensity bar graphs of peaks A (approximately 1490 cm^{-1}) and B (approximately 1590 cm^{-1}). Error bars are ± one standard deviation based on three replicate measurements of three replicate samples.

From this data, the optimal concentration of each nanotag, based on the absolute intensity of the peak at approximately 1600 cm^{-1}, can be regarded as follows: dye 1 = 500 nM, dye 2 = 450 nM, dye 3 = 500 nM and dye 4 = 350 nM. This is summarised in Table 2.

Table 2 - The optimal concentration of each nanotag upon 1280 nm laser excitation based on the peak intensity at approximately 1590 cm^{-1}.

Dye	Optimal concentration (nM)
1	500
2	450
3	500
4	350

Additionally, from this data, there does not appear to be any direct trend relating the dye NP binding orientation to the SERS response. Dye 1 and dye 3 functionalised NPs analysed in this study provide a SERS intensity which generally increases as the final dye on NP concentration increases. Dye 2 and dye 4 functionalised NPs follow a similar fashion in that the SERS response increases up to a final dye concentration of 450 nM and 350 nM respectively, after which the SERS response decreases.

Despite a direct relationship between dye molecule binding orientation and SERS response not being established as hoped, it was interesting to note that the peak ratios of the ~ 1590 cm^{-1} and ~1490 cm^{-1} peaks varied between the dyes and between some of the dye concentrations. This indicates a potential variation in the orientation taken by the CP dye molecules on the NP surface, different to that expected by the SFG-VS calculations. A bar graph highlighting these peak ratios

was formed in order to highlight this and allow any trends to be deduced. These bar graphs are shown in Figure 14.

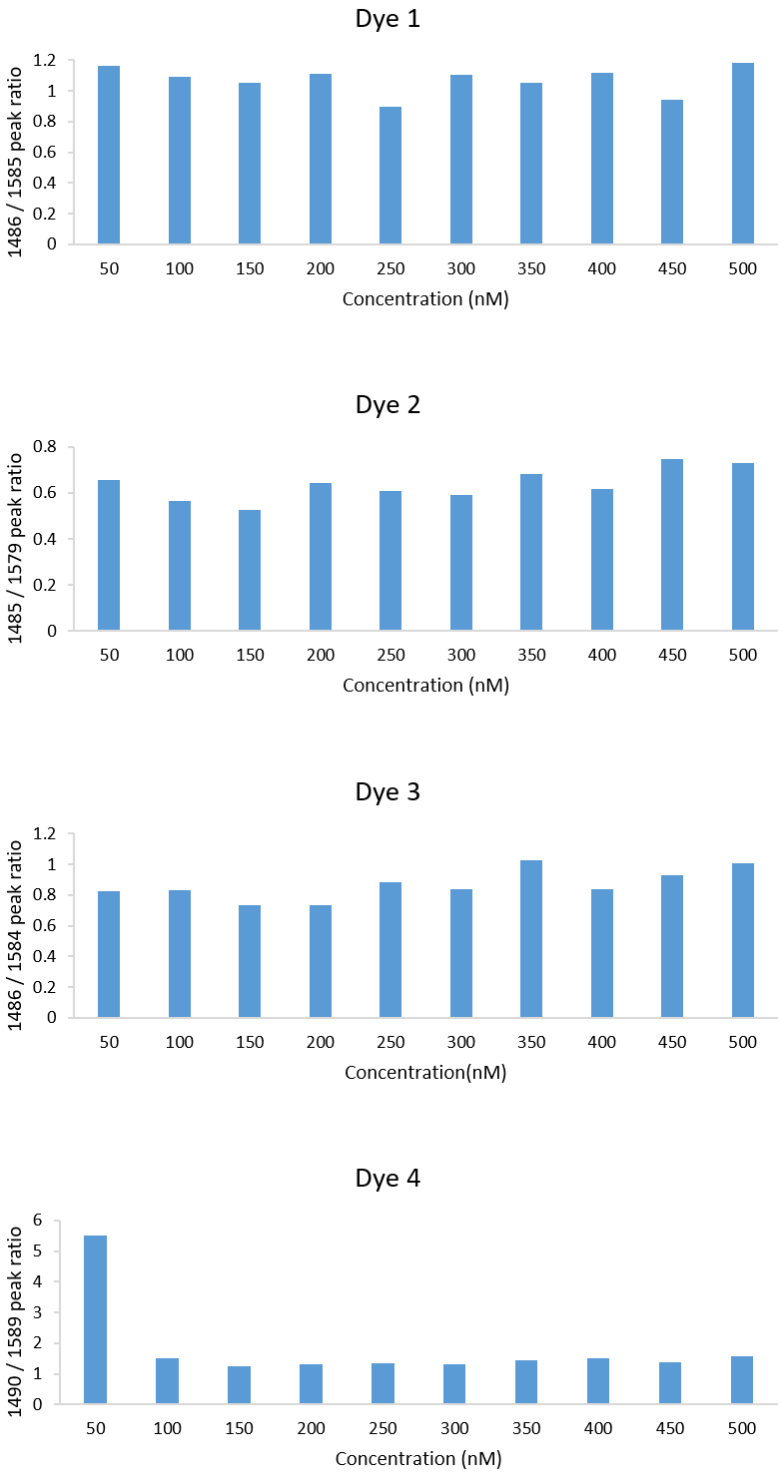

Figure 14 - Bar graphs demonstrating the peak ratio between the two main peaks in each nanotag spectrum. Dye 1: 1486 cm^{-1} and 1585 cm^{-1}. Dye 2: 1485 cm^{-1} and 1579 cm^{-1}. Dye 3: 1486 cm^{-1} and 1584 cm^{-1}. Dye 4: 1490 cm^{-1} and 1589 cm^{-1}.

The peak ratios of dye 1 tend to waver on or around 1 showing very little change in the relative peak intensities of bands 1486 cm^{-1} and 1585 cm^{-1} over the 50 - 500 nM concentration range analysed. This would indicate that this dye does assume its approximate 64° – 85° binding angle over this concentration range with little fluctuation relating to concentration variations. The peak ratios of dye 2 all lie between 0.5 – 0.7, again showing only a slight change in the relative intensities of the 1485 cm^{-1} and 1579 cm^{-1} peaks. This would again indicate very little variation in the molecules orientation from its SFG-VS estimated orientation of 59° - 80°, however the peak ratio is at its highest, around 0.75 over 450 - 500 nM, indicating that perhaps these molecules do assume the most upright orientation they can, most likely due to surface packing, at these higher concentrations. The peak ratio values of dye 3 are similar to dye 2 in that they are approximately 0.8, increasing to around 1 at the optimal concentration of 350 nM and at higher concentrations of 450 - 500 nM, indicating that these dyes may assume a more up right orientation due to surface packing at higher concentrations. Dye 4, however shows a very different peak ratio when comparing the relative intensities of the 1490 cm^{-1} and the 1589 cm^{-1} peaks. At the lowest concentration of 50 nM, the peak ratio is approximately 5.5, which then largely decreases to around 1.5 for concentrations 100 - 500 nM. It is thought that at 50 nM this molecule does assume, the calculated, almost flat orientation of 10° - 30°. Referring to Figure 12, at this concentration, dye 4 provides a poorer quality SERS spectrum in comparison to the spectrum acquired from the other dyes at this concentration. This is thought to be due to the fact that as the extent of the polarisation change along the core of the molecule is thought to be large, due to its π-system: the surface enhancement of this molecule on a nanoparticle surface would be thought to be at its greatest when this change in polarisation is perpendicular to the surface, i.e. the dye would be 'upright' on the nanoparticle surface. This complements the fact that in this study the more perpendicular dyes 1 and 2 provide more intense SERS spectra over this concentration range than that of dye 4. For concentrations 100 - 500 nM, the relative peak ratio of these two peaks drops to approximately 1.5 with an increase in the SERS intensities and improvement in the overall spectral resolution. This

would fit with the proposed idea that dye 4 may orientate slightly differently, i.e. in a more perpendicular orientation, due to molecular packing at these higher concentrations. Dye 4 does provide the poorest SERS response at all concentrations compared with the other three dyes studied, again eluding to the fact these dyes will exhibit optimal intense SERS enhancement when functionalised onto the nanoparticle surface in the most perpendicular arrangement possible.

With only the SERS and SFG-VS data at hand, it is difficult to directly relate an increasing dye attachment angle with a direct increase in SERS response. This assumptive relationship would only be guaranteed if the dye molecules were indeed assuming the binding orientation, and only that binding orientation, calculated by SFG-VS. However, we have to take into account the packing arrangement of the dye molecules on the nanoparticle surface and whether or not concentration and therefore molecular surface packing causes the dye molecules to assume the binding orientations calculated by SFG-VS. It should also be reiterated at this point that the SFG-VS analysis is carried out on thin dried gold films, whereas the SERS experiments are carried out on solid spherical nanoparticles in solution, where these dye functionalised nanoparticles are continually moving in an unpredictable and random fashion due to Brownian motion. Acquiring data enabling the understanding of dye molecule binding and surface orientation on solid surfaces in suspension is extremely difficult and no one technique gives a definitive answer.

While it is difficult to directly relate an increasing attachment angle with an increased SERS response as hoped, some useful information has come from this study, which will in fact aid chalcogenopyrylium dye selection for nanotag design based on the specific application. A general observation can be made relating the SFG-VS calculated binding angles with the optimal dye concentrations as shown in Figure 15.

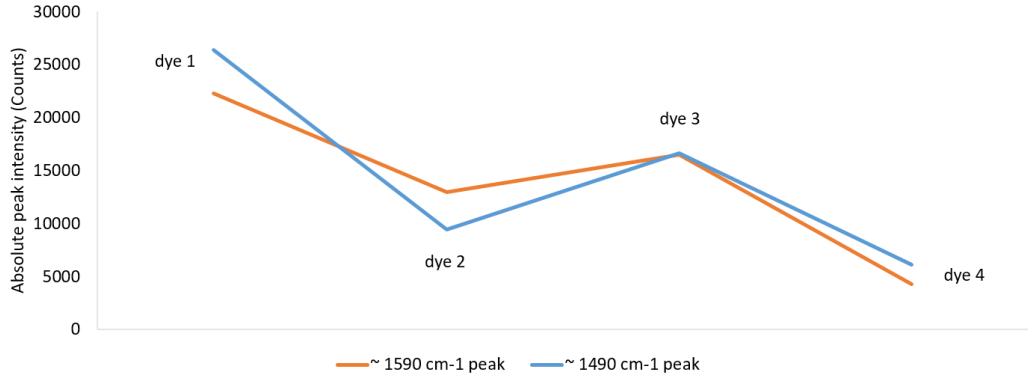

Figure 15 – Line graph showing the overall general decrease in absolute peak intensity for each dye at their optimal concentrations for both the~ 1490 cm^{-1} (blue) and ~ 1590 cm^{-1} (orange) peaks.

Decreasing the perpendicular nature of the dye attachment angle, as calculated by SFG-VS, does generally decrease the overall SERS intensity when we survey the optimal concentration for each dye. There is slight fluctuation with dye 3, and this brings attention to the individual atoms actually involved in the direct binding to the gold nanoparticle surface. It has been reported that dye 1 binds to the gold surface *via* rotation of the side selenophene rings, bringing the selenium atoms into contact with the gold surface leaving the sulphur atom in the pyrylium ring hovering just above the nanoparticle surface due to steric hindrance.[114] However, computational analysis has yet to be carried out on dyes 2, 3 and 4, therefore the exact binding orientation, and therefore atoms involved in the binding site are not yet confirmed. It is speculated that the strength of the interaction between the nanoparticle surface and atoms, in the dye molecule, involved in the binding could have an effect on the SERS response; however, further work would need to be carried out in order to confirm this.

3.4. Chapter Conclusions and Future Work

From purely the SERS data alone, it is not possible to confidently produce a wholesome relationship between the SFG-VS calculated binding angles and the SERS response. It is worth highlighting that the SFG-VS calculated binding angles are measured and acquired on thin dried gold films, what happens to these chalcogenopyrylium dyes on the surface of large spherical gold nanoparticles in solution could be completely different to that measured on dried gold films. It can be observed that generally, increasing the dye attachment angle, i.e. increasing the perpendicular nature of this angle and thus orientation of the dye molecule on the gold surface, does have an overall increase on the SERS response attained. It would be interesting to design and analyse more of these dyes over a wider SFG-VS calculated binding angle range in order to investigate further and potentially deduce a more wholesome relationship relating binding angle and spectral intensity.

From the four dyes analysed in this study and their acquired SFG-VS measurements, there are three possible extreme orientations for these dyes to assume: perpendicular (vertical or almost vertical), plane parallel with the metal surface and horizontal plane perpendicular to the metal surface. Dyes 1, 2 and 3 are most likely to assume some form of 'upright' almost perpendicular orientation as estimated by the SFG-VS and from the intensity of the peak ratios of the SERS spectra obtained. Bands that appear most intense in these SERS spectra ($\sim$ 1490 cm^{-1} and $\sim$1590 cm^{-1}) are believed to arise due to displacements along the core of the dye molecules, i.e. the pyrylium rings and core aliphatic body of the molecule. This π-system provides a readily polarisable electron cloud along the core of the dye molecule, therefore when the core of the dye molecule is as perpendicular as possible to the metal surface, the greatest surface enhancement will occur. Dye 4 fits the calculated SFG-VS binding formation of almost planar (10° – 30°) on the metal surface at the lowest concentration of 50 nM. At this concentration, the SERS response is poor, fitting with the explanation that as the π-system lies along the main axis of this dye molecule, optimal SERS enhancement would be obtained with this molecule in the most perpendicular

arrangement possible on the nanoparticle surface. Upon increasing the final concentration of dye 4, an increase in the SERS response is observed and this is likely attributed to the dye molecules assuming a more perpendicular, although not entirely perpendicular, surface conformation *via* surface packing effects at higher concentrations. It would be incredibly advantageous if dye 5 could be stabilised and included in these studies as the SFG-VS calculations predict this molecule to lie at 0°, i.e. plane parallel to the metal surface. This would help endorse the idea that in order for a respectable SERS response to be obtained, from these chalcogenopyrylium based nanotags, these dye molecules ideally should assume an orientation on the surface with some degree of perpendicular nature.

Acquiring any type data enabling the understanding of dye molecule binding and surface orientation on solid surfaces in suspension is extremely difficult and no one technique gives a confidently definitive answer. Therefore, other techniques should be employed in order to support the SERS data and confirm if in fact we can relate this SERS data to the SFG-VS calculated binding angles. As previously conducted with dye 1 on hollow gold nanoshells, it would be of great value to compare the SERS spectra obtained in these experiments with the Raman spectra and theoretical Raman calculations in addition to studying the electronic structure of these dye molecules. Again, as with work carried out for the determination of the binding of dye 1 to HGNs, it would be useful to employ computational simulations in order to fully conclude this work.

In addition to studying the molecular orientation vs SERS response, it would be thought provoking to investigate the interactions between the anchor chalcogen atoms and metallic nanoparticle surface. Dyes 1 – 4 bind to the nanoparticle surface *via* different chalcogen anchors, therefore it would be interesting to ascertain whether the specific atoms involved in the metallic surface binding show any form of relationship with the SERS response achieved. Again, a larger study employing more CP based dyes with varying chalcogen anchor molecules would be beneficial.

4. Wavelength Selective SERS for Invisible Tagging and Detection

4.1. Introduction

There is immense interest and urgency in SERS substrates as novel anti-counterfeit technologies covering a whole host of specific applications ranging from security labels on important documents to the labelling of items for the protection against piracy of consumer goods.[122] In 2015, the global cost of counterfeiting was estimated at $1.7 trillion with the number of counterfeit seized goods on the increase year after year.[123] Therefore there is great demand for novel substrates capable of improving the ease of detection and statistics surrounding counterfeit goods. Many attempts have been made to implement a form of 'tag' allowing companies and defence sectors to protect their goods; holograms, colour-changing inks and security graphics have all been exhausted, increasing the urgency for new and improved anti-counterfeit technologies.[124]

There have been reports, in recent years, employing Raman spectroscopy and SERS in the design of 'tags' for specific anti-counterfeiting purposes. Ling *et al.* have created a multiplex plasmonic anti-counterfeiting platform in which the molecular information, of the sample, can only be identified and 'read' using Raman spectroscopy – something the majority of criminals and organised crime groups involving manufacture of fake goods, in the past, would not have access to. Here, Raman active labels are embedded in nanowires which can only be successfully detected when viewed at different spectral positions or viewed when individual vibrational modes are chosen, making it almost impossible to determine the molecular fingerprint without preceding knowledge of how to conduct the analysis.[125] Rodriguez and co-workers have developed a Raman barcode system specifically for the detection of fake and dangerous counterfeit drug products. Here a unique Raman barcode was created for a multitude of drug molecules by comparing the spectrum of their active pharmaceutical ingredient (API) to the spectrum of the drug sample in question.[126] However, with the advent

of mass commercialisation and the advancement of portable handheld Raman technology, it is now easier than ever for criminals to hone in on this technology and 'catch up' with the regulatory bodies trying to prevent fake, dangerous, counterfeit goods from being distributed.

Here, a colloidal solution has been developed consisting of the combination of a chalcogenopyrylium dye based nanotag and chalcogenopyrylium dye based 'blocking' molecule which can only be detected using a prototype 1280 nm Raman spectrometer, in which the signal remains transparent at the more commonly used and much more readily available 785 nm excitation wavelength. Although the exact application of this nanotag is unknown, it is anticipated this will be applied in invisible tagging and detection of important items in conjunction with Raman spectrometers equipped with excitation wavelengths no one other than the personnel producing these 1280 nm SERS active nanotags, would be able to detect.

4.2. Chapter Aims

The aim of this chapter was to design a nanotag capable of providing a clear and relatively intense SERS response upon 1280 nm excitation while remaining invisible and providing no SERS signal upon 785 nm excitation. This could be achieved by either nanotag signal elimination or nanotag signal masking. A cartoon schematic of which is shown in Figure 16. The exact application of this nanotag is unknown, however it is speculated this system will be used for the tagging and unique invisible identification of materials in matters relating to defence and security.

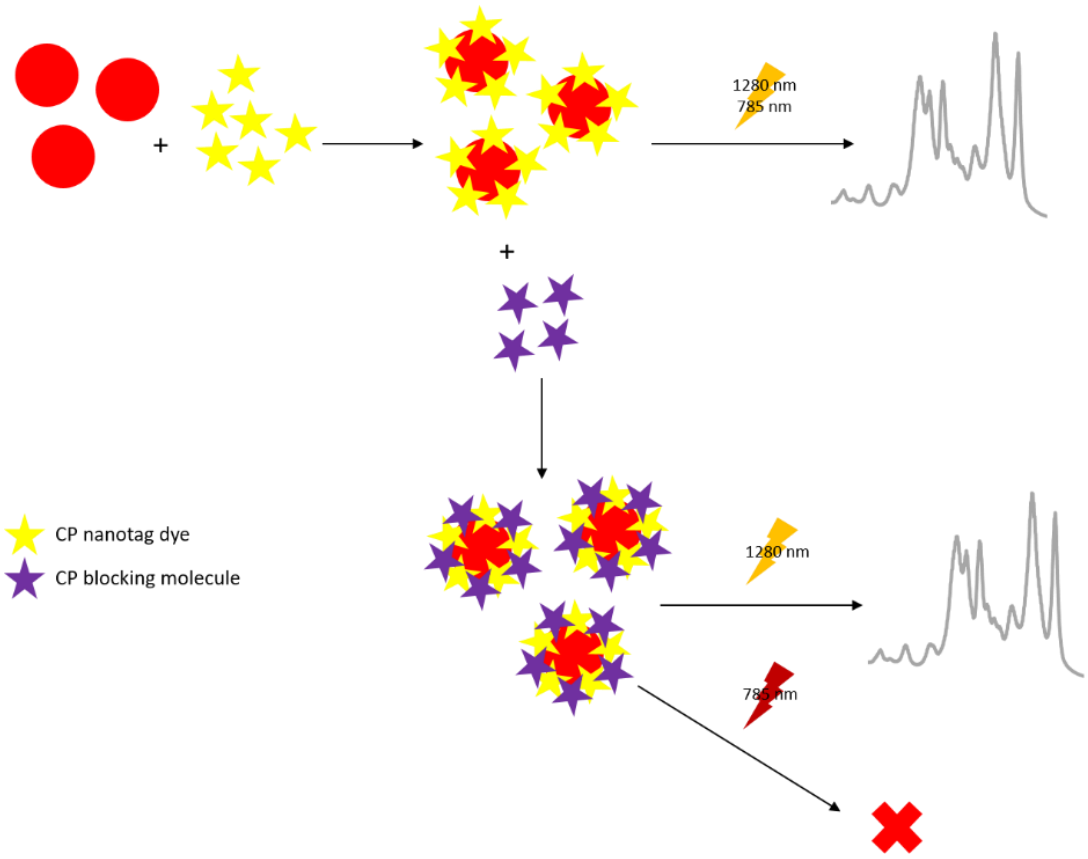

Figure 16 - Cartoon schematic highlighting the functionalisation and SERS response of the chalcogenopyrylium dye based nanotag, upon 785 nm and 1280 nm laser interrogations, with and without addition of the blocking molecule. A SERS response is achieved on interrogation with a 1280 nm laser but not with that of a commercially available 785 nm laser.

4.3. Results and Discussion

4.3.1. Synthesis and Characterisation of Gold Nanoparticles

Synthesis and characterisation of gold nanoparticles is as reported in section 3.3.1.

4.3.2. Nanotag Design, Functionalisation and SERS Response

A chalcogenopyrylium dye was selected based on its absorbance maxima: 959 nm. This is the highest absorbing CP based dye synthesised thus far and has shown excellent SERS response at 1280 and 1550 nm excitation, therefore is a known candidate for red shifted SERS applications.[94,95] The structure of this dye molecule is reiterated in

Figure 17.

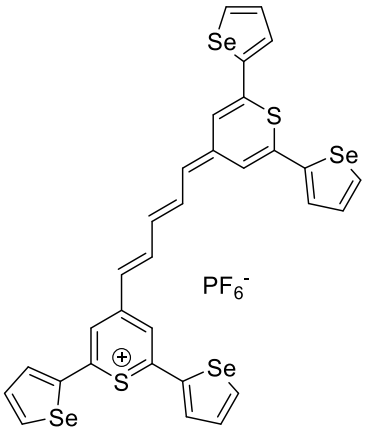

Figure 17 - Structure of the chalcogenopyrylium dye reporter molecule (dye 6), with an absorbance maxima of 959 nm, used in this study.

A concentration study of 50 – 500 nM was carried out in order to determine the optimal tag concentration; the concentration at which the most intense SERS response would be achieved. It should be noted that as with the CP-nanotag concentration studies carried out in chapter 3, final concentrations above 500 nM were unstable; nanotags would crash out of solution and no SERS signal would be achieved, therefore the concentration study was capped at a concentration of 500 nM. Figure 18 shows the average raw SERS spectra of the nanotag, at concentrations 50 – 500 nM, upon 1280 nm excitation and a bar chart displaying the absolute peak intensity, of the most intense peak in the spectrum, at 1561 cm^{-1}. The absolute peak intensity was determined by subtraction of the

intensity value at the base of the peak from the maximum intensity value of each peak. The base peak values for all spectra analysed were kept consistent and taken from the Raman shift at 1550 cm^{-1}. From this, the optimal nanotag concentration, can be deemed as 350 nM. The dye was added to the NP solution and allowed to shake for 15 minutes before being purified by centrifugation to ensure no excess free CP dye molecule was present in the nanotag solution.

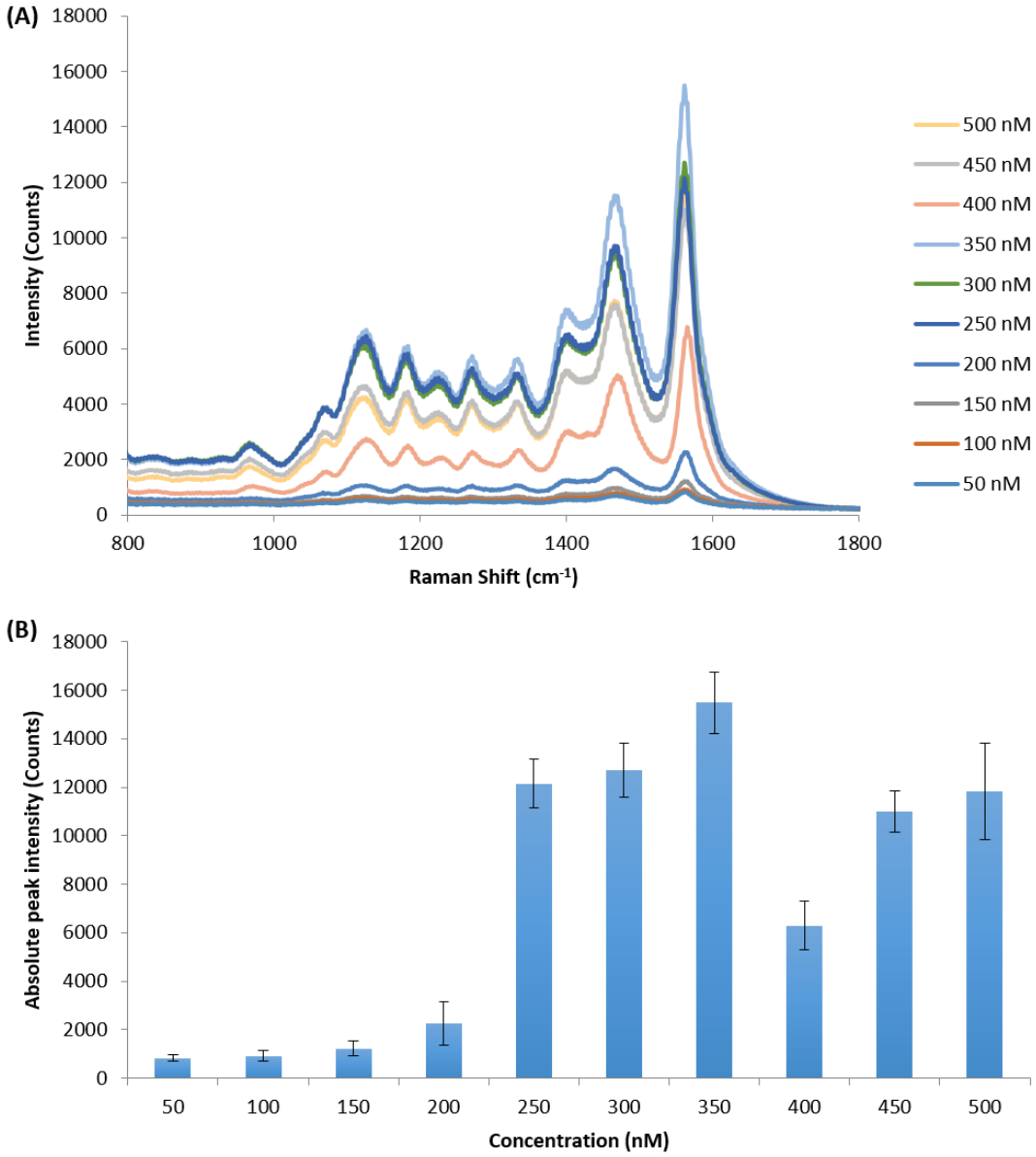

Figure 18 – (A) Raw average SERS spectra and (B) absolute peak intensity bar graph of the 1561 cm^{-1} peak of the dye 6, functionalised onto ~ 100 nm AuNPs, measured with a laser excitation of 1280 nm, 100 mW laser power, and an integration time of 3 seconds. Bar graph error bars are ± one standard deviation based on three replicate measurements of three replicate samples.

4.3.3. Addition of the Blocking Molecule

A solution containing solely the blocking molecule (BM), was added to the nanotag solution, in various concentrations, and the SERS response of the

nanotag at 1280 nm and 785 nm observed. The structure of this blocking molecule and its absorbance spectrum measured in DMF are shown below in Figure 19.

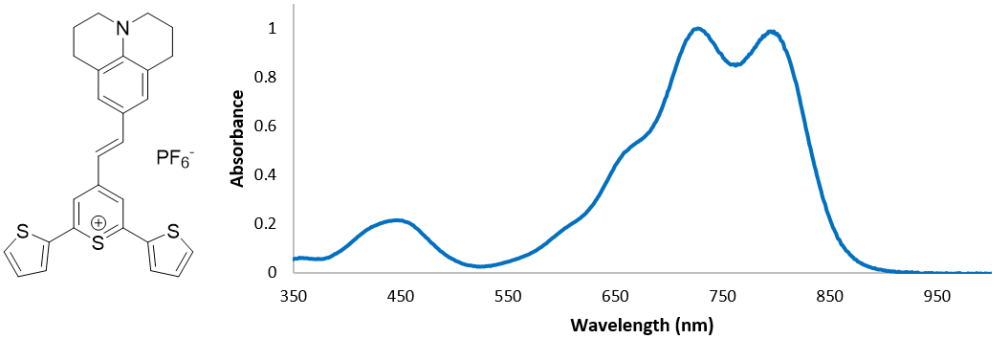

Figure 19 – Chemical structure and absorbance spectrum (measured in DMF) of the blocking molecule, measured at a scan rate of 1 nm per second.

This absorbance spectrum is different to that of the absorbance spectra acquired from the other chalcogenopyrylium molecules used throughout this thesis in that it has two major absorption maxima: 731 nm and 793 nm, with the other CP dye molecules possessing one major band corresponding to a π to π* transition within the electron density in the core of the molecule. (See appendix). As the molecule possesses two absorption maxima, this indicates that it will occupy two states when the molecule is excited. This is most likely what allows us to achieve the nanotag signal masking effect upon 785 nm excitation, as this molecule will be highly absorbing over the wavelength range 731 – 793 nm.

4.3.4. 785 nm and 1280 nm SERS Measurements

SERS measurements were performed using two Snowy Range (now Metrohm Raman) portable Raman spectrometers, one fitted with a 785 nm laser source (100 mW laser power) and the other a 1280 nm laser source (100 mW laser power). Initially, blocking of the nanotag signal at 785 nm excitation was achieved by adding a high enough concentration of the BM that the detector of the 785 nm spectrometer would be saturated and the signal would therefore 'top

out', with this effect not being observed at 1280 nm. At 1280 nm excitation, the signal remained consistent except for a slight decrease in intensity due to the dilution of the nanotag sample. This is illustrated in Figure 20.

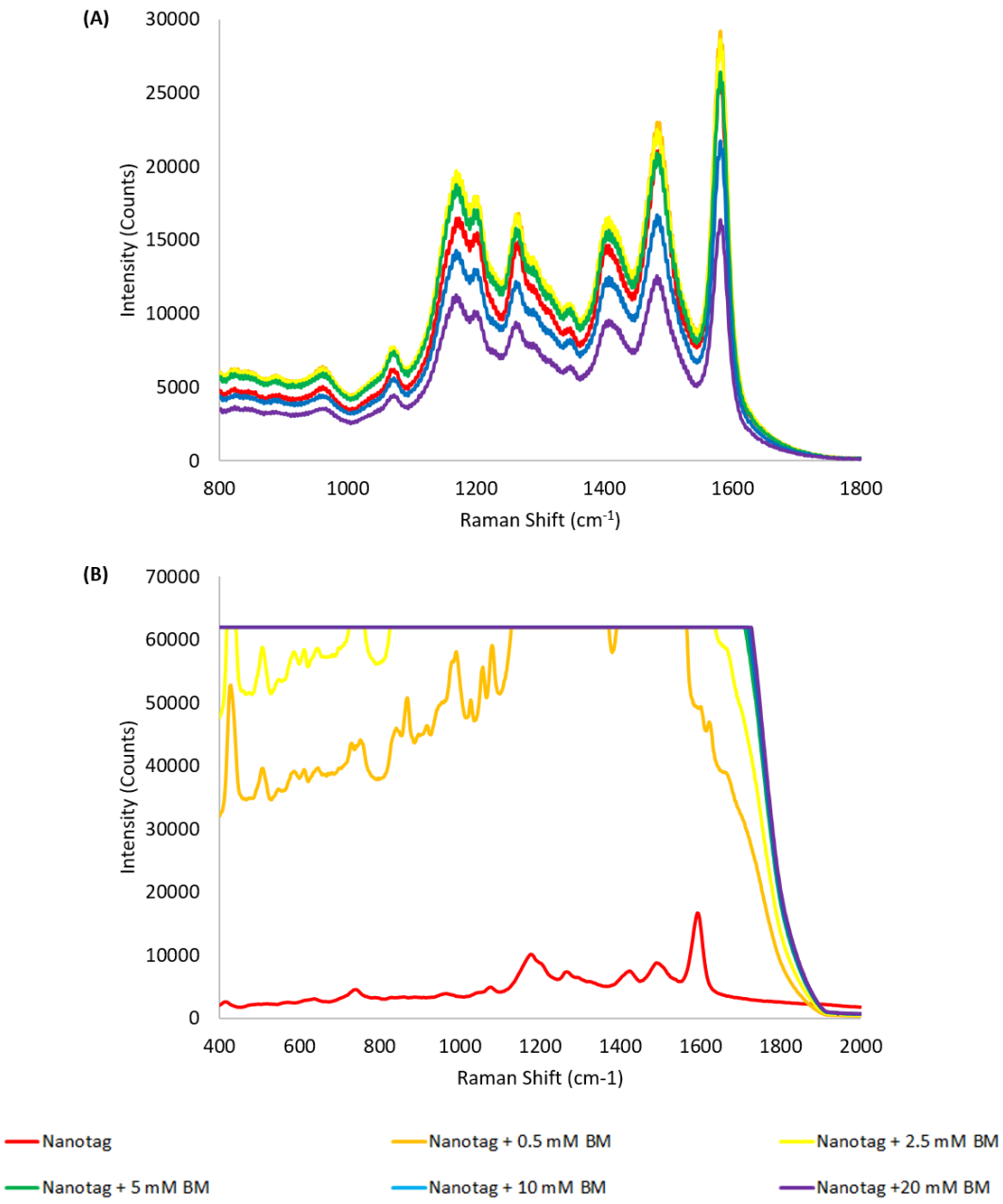

Figure 20 - Average SERS spectra of the nanotag with increasing concentrations of BM recorded with (A) a 1280 nm excitation, 100 mW, with an integration time of 3 seconds and (B) a 785 nm excitation, 100 mW, with an integration time of 0.01 seconds. The samples were prepared in triplicate with three replicate measurements of each sample recorded.

Figure 20 shows that it is possible to entirely block the signal of the nanotag from 785 nm detection, by oversaturating the detector, at a minimum concentration of 5 mM BM while maintaining a good level of signal intensity, from the nanotag, at

1280 nm. Additionally, it should be noted that the integration time of the 785 nm spectrometer was decreased and set to the lowest possible setting of 0.01 seconds, and that even at such a low integration time this BM was still able to oversaturate the detector and thus no signal from the dye 6 nanotag was observed.

To further this and confirm the ability of the blocking molecule to obscure the nanotag signal selectively, a concentration study was carried out in order to determine if there was a concentration at which the signal from the nanotag could be obscured spectrally with a response from the blocking molecule itself, rather than simply oversaturating the detector, 'topping out' and therefore eliminating the nanotag signal. Figure 20 also suggests that a resonance Raman response could be being achieved from the blocking molecule itself at higher concentrations.

Before this was carried out, it was important to attain the SERS spectrum of solely the blocking molecule at both 785 and 1280 nm laser excitations to determine whether there were any spectral differences between the blocking molecule and the nanotag which would allow the point at which the signal from the blocking molecule obscured the signal from the nanotag to be identified. A concentration study of the blocking molecule directly adsorbed onto AuNPs over the concentration range 50 – 500 nM was carried out. Again, it should be noted that at concentrations above 500 nM, the nanotags would crash out of solution and thus no signal would be achieved. This is shown in Figure 21.

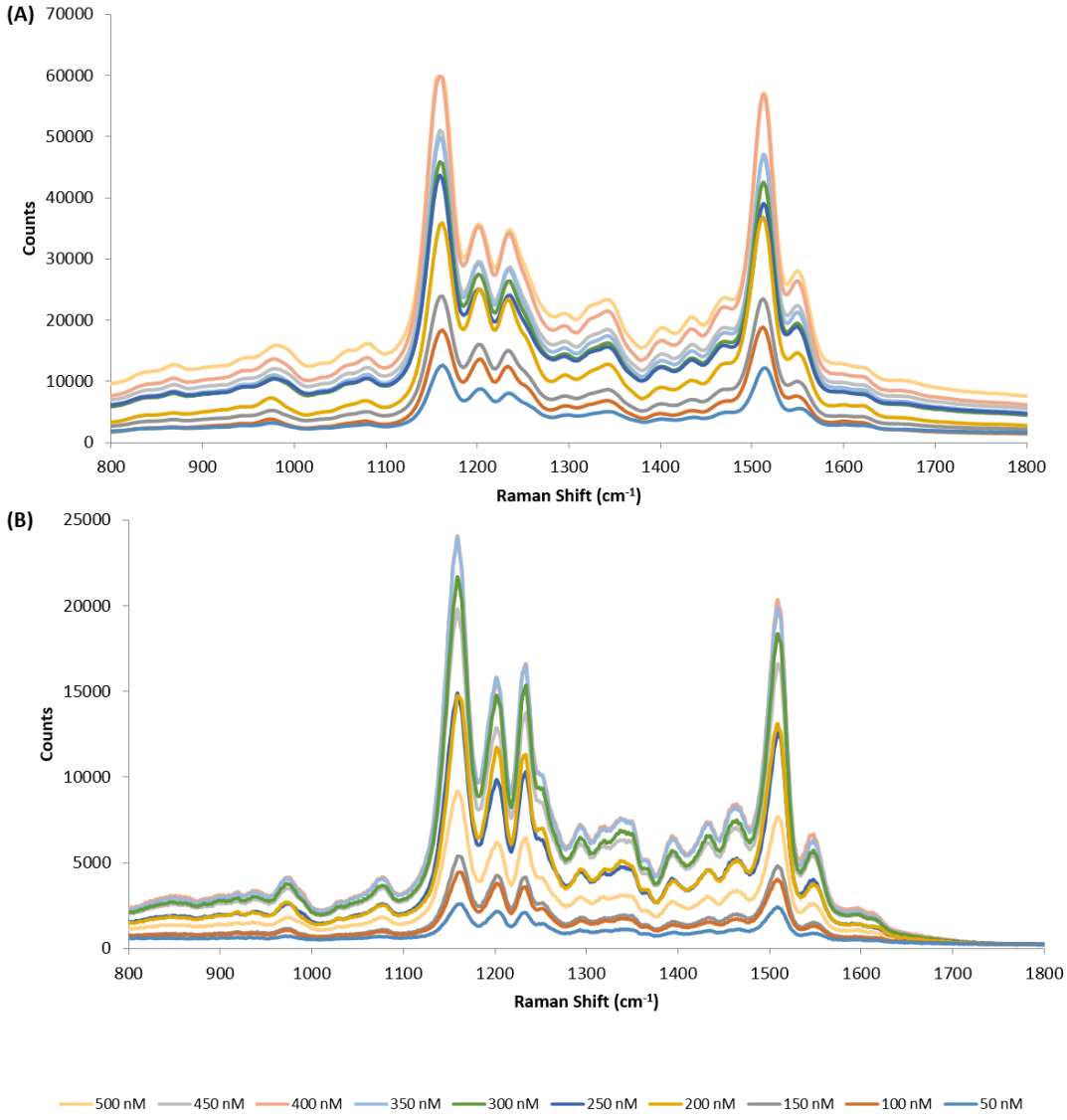

Figure 21 - Average SERS spectra of the BM functionalised onto large gold nanoparticles recorded using (A) a 785 nm laser excitation, 100 mW laser power and (B) a 1280 nm laser excitation, 100 mW laser power (bottom), both with a laser integration time of 3 seconds. The samples were prepared in triplicate with three replicate scans measured for each sample.

From this data, it is understood that the peak corresponding to the main body of the CP based blocking molecule lies at 1516 cm^{-1} upon 785 nm excitation and at 1509 cm^{-1} upon 1280 nm excitation. In comparison, the peak which corresponds to the main body of the CP dye in the nanotag (and the peak most commonly tracked in applications with these CP dye molecules) lies at 1597 cm^{-1} upon both

785 and 1280 nm excitations, therefore it should be easy to decipher at which point the nanotag signal is obscured by signal from the blocking molecule. It should be noted that upon 785 nm excitation, the spectrum corresponding to the nanotag possesses a peak at 1521 cm^{-1} that at first glance appears to be the corresponding BM peak. This 1521 cm^{-1} peak actually shifts to 1516 cm^{-1}, at a concentration of 825 nM BM, which at this concentration and above, can be attributed to the BM, not the nanotag.

Following this, a concentration study of BM added to the nanotag, over the concentration range 99 nM – 1666 μM was carried out at both 785 and 1280 nm excitations. This would allow determination of the concentration at which the signal of the nanotag is obscured by spectral noise or by potential SERS signal from the BM itself. The results of this upon 1280 nm laser excitation are shown in Figure 22 and the absolute peak intensity of the 1597 cm^{-1} peak plotted as a bar graph, shown in Figure 23.

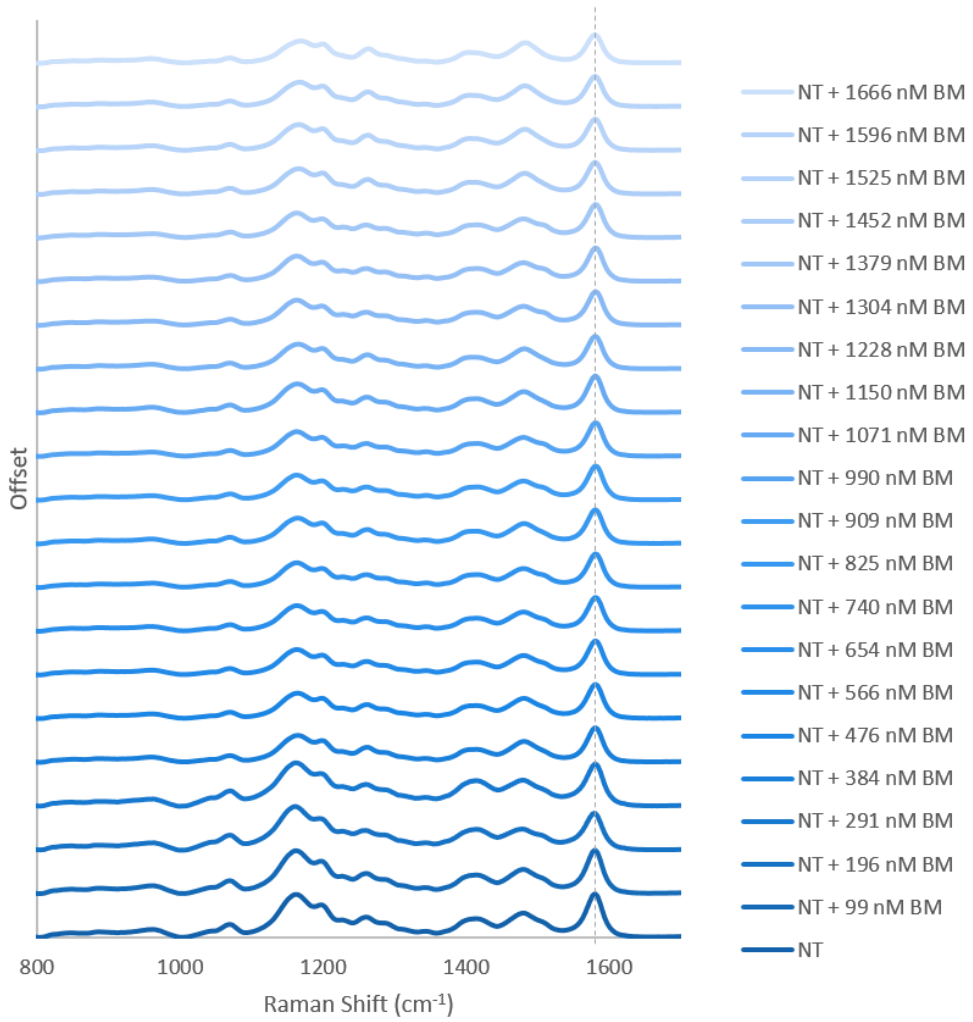

Figure 22 – Average normalised stacked SERS spectra of the nanotag upon addition of increasing concentration of BM at 1280 nm excitation, 100 mW laser power, and a laser integration time of 3 seconds. A dashed line highlights the dye peak of interest at 1597 cm^{-1} corresponding to the vibration through the main body of the CP dye molecule.

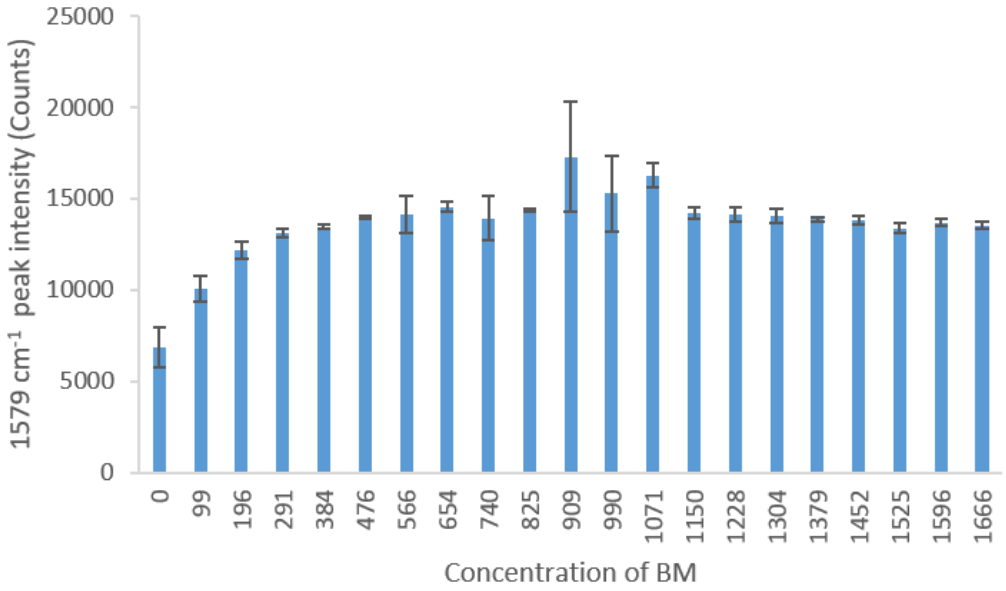

Figure 23 - Peak intensity bar graph of the 1597 cm^{-1} peak corresponding to the nanotag upon the addition of increasing BM concentrations at 1280 nm excitation. Error bars are ± one standard deviation based on three replicate measurements of three replicate samples.

It is observed that the BM has little effect on the SERS signal of the nanotag, upon 1280 nm excitation, throughout the concentration range of 99 nM – 1.666 µM, in which the SERS intensity of the 1597 cm^{-1} peak appears to remain relatively consistent despite a slight deviation around 909 nM, thought to be attributed to a slight error in the measurement. Initial increase of the peak intensity at lower concentration of BM is most likely due to the nanotag itself, self-aggregating upon initial functionalisation. It is not believed that the blocking molecule interacts with the nanotag / nanoparticle surface; a reason for this will be discussed further in section 4.3.5.

This concentration study was also analysed at 785 nm excitation, producing an interesting result. Here, at the lowest BM concentration, 99 nM, the signal from the nanotag drops very significantly and is eventually fully masked by the signal from the BM itself at higher BM concentrations. This is shown in Figure 24 with a peak intensity bar chart of signal intensities of both the BM (1516 cm^{-1}) and nanotag (1597 cm^{-1}) shown in Figure 25. Again, it should be noted that the spectrum of the nanotag possesses a peak at 1521 cm^{-1} that upon first glance

appears to be the corresponding BM peak. This 1521 cm^{-1} peak actually shifts to 1516 cm^{-1}, at a concentration of 825 nM BM, contributed to from the BM.

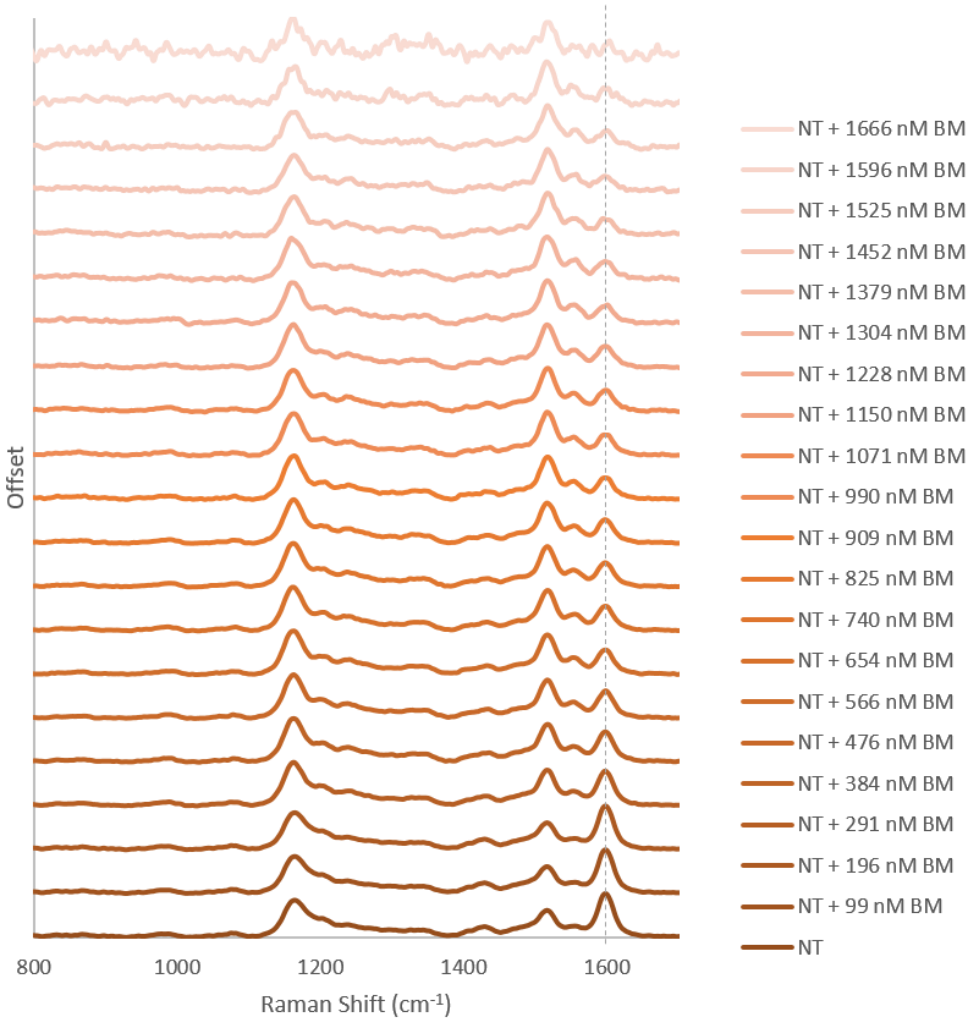

Figure 24 – Average normalised stacked SERS spectra of the nanotag upon addition of increasing concentration of BM upon 785 nm excitation, 100 mW, with a laser integration time of 3 seconds. A dashed line highlights the main nanotag dye peak of interest at 1597 cm^{-1} corresponding to the vibration through the main body of the nanotag dye molecule.

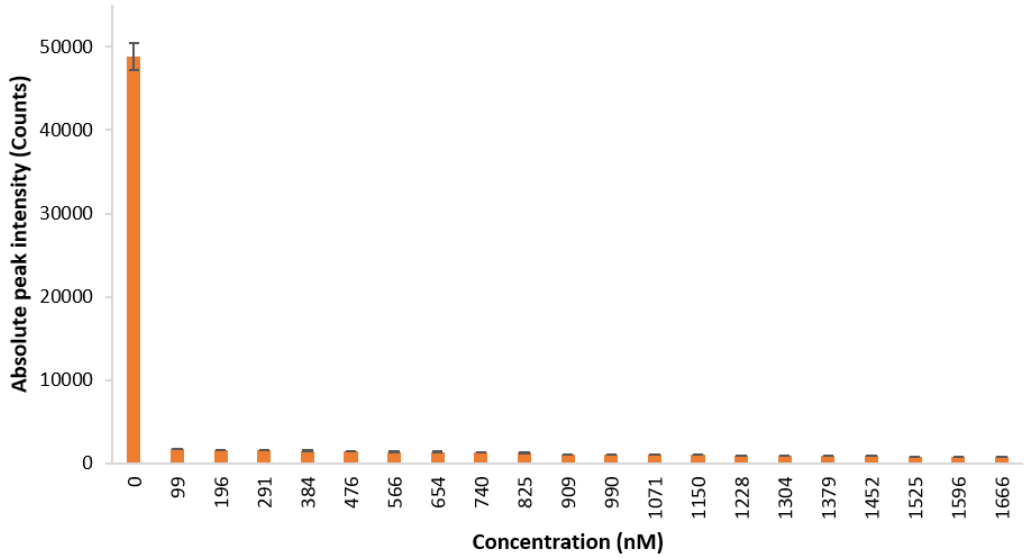

Figure 25 - Peak intensity bar graph of the 1597 cm^{-1} peak corresponding to the nanotag, upon the addition of increasing concentrations of the blocking molecule at 785 nm laser excitation. Error bars are ± one standard deviation based on three replicate measurements of three replicate samples.

It should be highlighted that from 1452 – 1666 nM BM, the peak which appears apparent at 1597 cm^{-1} cannot be assigned with certainly to the nanotag as the peak intensity here is less than three times the standard deviation of the blank measurement and appears mainly to be spectral noise. Therefore, without the 1597 cm^{-1} peak corresponding to the nanotag and with the peak corresponding to the BM at 1516 cm^{-1} dominating, it can be said that the BM successfully obscures the nanotag peak at concentrations above 1452 nM. In addition, contributing peak from the nanotag at 1158 cm^{-1} shifts to 1164 cm^{-1} at BM concentrations of 825 nM BM, further eluding to the idea that the BM begins to obscure the peaks corresponding to the nanotag, and becomes the dominating spectrum, at approximately 825 nM BM in addition to significantly reducing the signal of the nanotag peak at 1597 cm^{-1}.

4.3.5. Supernatant Study

It was important to produce reasoning for why masking of the nanotag occurs simply by addition of this dye molecule to the colloidal solution. A supernatant study was carried out in an attempt to understand if the BM attaches itself to the nanotag or simply remains in solution. Here, the nanotag was created and the BM, in solution, then added at a concentration of 1.666 µM. The nanotag was then separated from the supernatant by centrifugation, re-suspended in d.H_2O and the extinction measured. The absorbance of the supernatant was also measured for comparison to that of just the dye in solution in order to determine whether surface attachment of the BM actually occurs. Figure 26 shows the average UV-Vis measurements of the substrate.

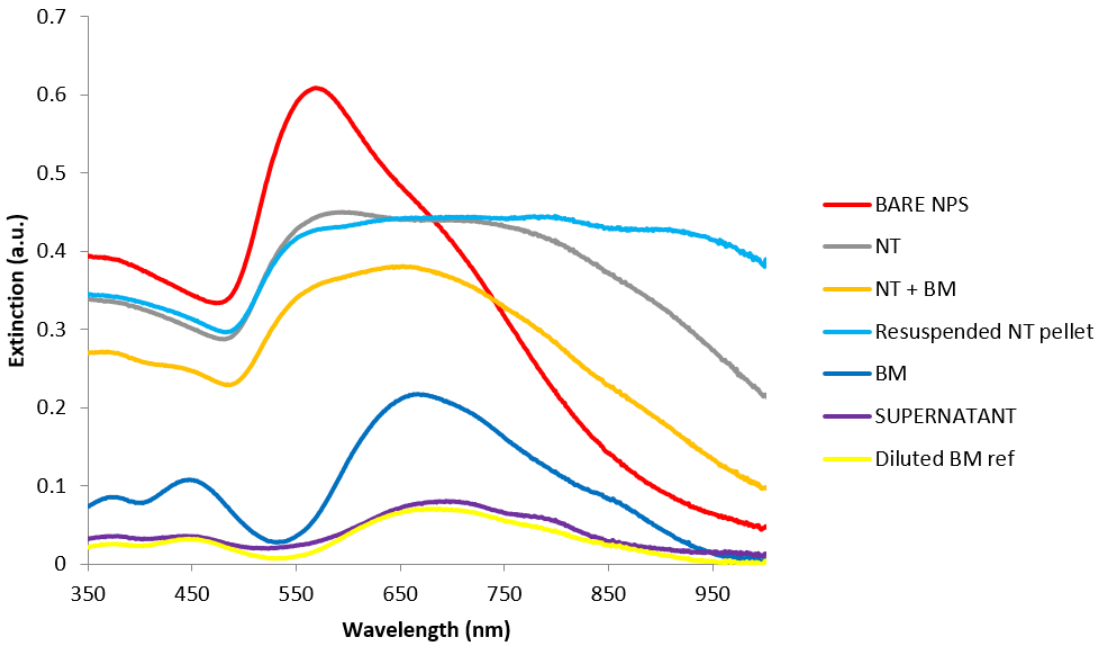

Figure 26 – Extinction spectra of a study on the supernatant of this SERS substrate showing bare nanoparticles (red), dye 6 nanotag (lilac), nanotag + 1666 nM blocking molecule (orange), re-suspended nanotag pellet after purification by centrifugation (light blue), blocking molecule in solution (dark blue), supernatant after purification by centrifugation (purple) and the blocking molecule in solution dilute to the same dilution as that of the supernatant (yellow).

Here, dampening of the bare nanoparticle LSPR (red line) can be seen upon addition of the reporter molecule (lilac line), creating the nanotag, as expected. After centrifugation, the re-suspended nanotag pellet (pale blue line) provided an extinction profile very similar to that of the initial nanotag extinction measurement. Assuming that during centrifugation all of the nanotags collected in the pellet, the absorbance of the supernatant (purple line) was measured and again, had a very similar absorbance profile to that of the aqueous BM solution at the same dilution (dark blue line). This allows the assumption that the BM remains in solution and is not actually adsorbed onto nanoparticle or nanotag surface.

A proposed reasoning for this signal masking, from the data above, is that the blocking molecule must absorb most of the light scattered by the nanotag, thus blocking any nanotag signal from reaching the detector. For this to occur it would be expected that the BM would have to be on or in very close proximity to the NP surface. As it has been concluded the blocking molecule does not adhere to the nanotag, it is assumed that in concentrations above 1452 nM, there is enough of the blocking molecule present around the nanotags for this absorption of scattered light to occur, thus masking the nanotag signal upon 785 nm laser excitation.

It should be noted in this discussion that this work was carried out, with each replicate sample, using one sample in one vial, i.e. the sample was measured at 1280 nm excitation, and then immediately measured at 785 nm excitation. This was also conducted in reverse, firstly acquiring the SERS measurement at 785 nm with the same vial being inserted into the 1280 nm spectrometer. This confirmed that nanotag sample degradation as result of either laser excitation was the not reason for this selective SERS observation.

4.4. Chapter Conclusions and Future Work

A solution-based system of a wavelength selective nanotag has been developed allowing detection of a chalcogenopyrylium based nanotag upon excitation of a 1280 nm laser, which cannot be detected upon excitation with a 785 nm

excitation wavelength due to the masking of this nanotag signal by the addition of a blocking molecule. It is believed that this blocking molecule, when present in high enough concentrations, is able to absorb the scattered light from the nanotag upon excitation therefore preventing its SERS response from being observed. This can be achieved in two ways. Firstly, adding a large concentration (5 mM or greater) of the blocking molecule to the nanotag solution causes the detector to become over saturated spectrum acquired to 'top-out' upon 785 nm excitation but not at 1280 nm excitation, even when set to the lowest integration time possible by the 785 nm spectrometer. Therefore, at blocking molecule concentrations of 5 mM and above, the nanotag spectrum is eliminated from view by use of detector saturation. Secondly, the ability of this blocking molecule to mask the nanotag signal was studied over the concentration range 99nM – 1666 nM in order to deduce a concentration of blocking molecule at which this nanotag spectrum would not be observed. It was found that at concentrations of 1452 nM and above the main peak corresponding to the nanotag (1597 cm^{-1}) was not visible by eye and was dominated by spectral noise. The main peaks corresponding to the blocking molecule at 1164 cm^{-1} and 1516 cm^{-1} become apparent in the spectra at a concentration on 825 nM indicating that at this concentration and above, the blocking molecule masks the nanotag signal successfully.

As the proposed reasoning for this was that the blocking molecule absorbed the scattered light from the nanotag, it was important to decipher whether or not this was achieved because the blocking molecule adhered to the nanoparticle surface / nanotag surface layer or was simply present in solution in a high enough concentration for this masking effect to be observed. A study on the supernatant of the nanotag solution was carried out concluding that the blocking molecule does not adhere to the nanoparticle surface / nanotag surface layer and remains free in solution. Therefore, if enough of the blocking molecule is present in the solution surrounding the nanotag, this masking effect will occur.

Initially, it was thought that nanotag sample degradation as a result of laser interrogation could be a reason for this selective SERS effect being observed.

However, by analysing these samples in the same vial from spectrometer to spectrometer and then in reverse order, it could be confirmed that no nanotag degradation was taking place as a result of laser interrogation.

At present, this work is solution based; therefore it would be interesting to investigate whether or not this masking effect will still be observed if this was particle based. This could involve coating the nanotag itself in a stabilisation layer in which the blocking molecule would be functionalised onto, or perhaps creating a mixed monolayer of the dye 6 reporter molecule and the blocking molecule. It is anticipated the former could be achieved through use of a silica or polymer capping layer and it would be interesting to carry this idea forward in order to determine if SERS signals will still be achieved through use of stabilising agents.

Although the specific application of these wavelength selective nanotags is unknown, it is speculated that DSTL have interest in using these nanotags to coat and mark various objects for authenticity, counterfeiting and specialised detection. Therefore, it would be interesting to see if, once a whole nanotag has been developed, coating and drying these nanotags onto a variety of different surfaces, will still allow an intense SERS spectrum to be achieved with this same wavelength selective capability. As coatings and markings for purposes of identification and security may be a future application of these nanotags, it would be of interest to investigate the ability of these nanotags to produce this wavelength selective SERS effect when diluted to the point of transparency in solution, i.e., the nanotags appear undetectable and clear in solution to the naked eye but still provide a SERS response with the 1280 nm laser excitation and not the 785 nm laser excitation. This would provide the ability to invisibly tag items of interest in addition to invisibly detecting them.

Again, the specific application of these wavelength selective nanotags is unknown, however, it is known that DSTL have interest in applying these nanotags in harsh conditions, i.e., environments where poorly stabilised nanotags would degrade in solution and thus provide no SERS response. It would be of great interest to apply these nanotags, once stabilised, in solutions containing strong acids, strong bases, solvents, peroxides and saline buffers in order to

assess their ability to perform as wavelength selective nanotags under these conditions.

5. The Depth of Penetration of Portable Hand-held Raman Spectrometers: An Excitation Wavelength Comparison

5.1. Introduction

The requirement for the non-invasive ability to probe through biological barriers, such as tissues, fats, bone and fluids, has become increasingly urgent in recent years due to the complications, difficulties and costs surrounding current and popular biomedical methods. As it stands, many methods for the detection of cancerous tumours and other fatal diseases possess disadvantages, which often result in a prolonged diagnosis time thus making the disease increasingly difficult to treat in its latter advanced and complicated stages. Invasive blood tests are often time consuming, with many samples requiring analysis in laboratories far from the point of care with these samples requiring collection and analysis by a skilled medical professional. Medical imaging is at the forefront of tumour detection and diagnosis, however some of these imaging techniques, such as magnetic resonant imaging (MRI)[127] and positron emission tomography (PET)[128], are incredibly expensive, very large and in an isolated and fixed position, requiring a highly trained specialist to operate, perform and interpret the results. Confocal techniques are often employed to obtain signal and high-resolution images through varying barriers, with the ability to control depth of field and reduce often noisy backgrounds.[129,65] However, biomedical research is moving away from large machinery and bulky, conventional bench-top instrumentation for sample analysis, to smaller, portable instrumentation, in order to easily translate these imaging techniques into the clinic / operating theatre and to speed up diagnosis time scales. Therefore there is considerable scope for the development of economical, easy to operate, non-bulky instrumentation for the detection of tumours and other types of diseased tissues at depth through numerous types of biological media.[130]

Raman spectroscopy offers a means to attempt to solve these various problems with the ability to provide a unique chemical fingerprint of the sample analysed without sample destruction and complicated sample preparation. There has been substantial advancement over the years in Raman spectroscopy, in particular with the development of simpler, smaller and portable instrumentation making Raman spectroscopy, and its adducts, particularly attractive for application in biomedical research. There has been recent growth in the application of spatially offset Raman spectroscopy (SORS) and surface enhanced spatially offset Raman spectroscopy (SESORS) for the detection and analysis of analytes at depth through a variety of biological barriers. SORS is a technique in which two measurements are acquired, one at the source and one at an offset, usually a few millimetres in size. This is shown in Figure 27.

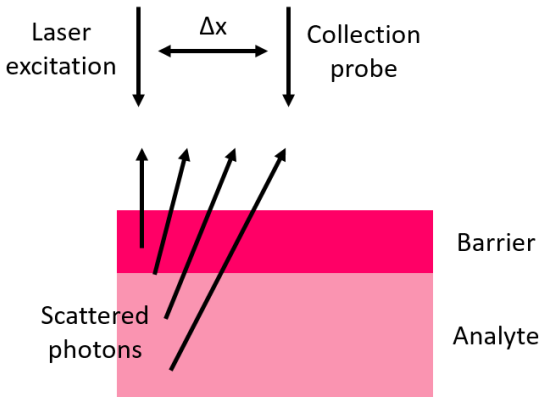

Figure 27 – Illustration of SORS in a back-scattered set-up. Moving the collection probe further from the point of laser excitation, photons in the deeper layers can be collected by the spectrometer.

These spectra are then subtracted producing a SORS spectrum corresponding to the surface measurement and a spectrum corresponding to the signal acquired at depth, creating the ability to probe through barriers and obstructions of varying thicknesses. The thickness at which spectra can be acquired can be altered and pre-set by the user allowing specific thicknesses of interest to be reached.[131,132] Sharma *et al.* has shown the impressive ability to detect nanotags, functionalised

with a commercially available Raman reporter molecule, through up to 8 mm of bone,[133] with Moody and Sharma advancing upon this by demonstrating the ability to detect multiple neurochemicals, at concentrations as low as 100 μM, through a feline skull specimine.[134] This was achieved by the use of a small and portable, spatially offset Raman spectrometer. Breast cancer tumour calcification models have also been detected through up to 10 mm of tissue by exploiting the characteristics of SORS,[135] with complimentary research following with the imaging of multicellular tumour spheroids at depth as a breast cancer model bye use of SESORS.[136]

SE(R)RS has been exploited for the detection and analysis of cancers in biological tissue samples. Harmsen and co-workers have highlighted the capabilities of inoperative cancer imaging with SERRS by detecting prostate tumours in mice using nanoprobes injected *via* the mouse tail vain. Here the nanoprobes were found to accumulate at malignant prostate tissue sites but not in that of the healthy prostate tissues and could be easily imaged using SERRS. However, this research was carried out using a large, bulky, fixed confocal Raman microscope system, something which if these probes are developed further may prevent full clinical translation again due to the complexity of use and requirement of a skilled and trained individual to operate. Therefore, there is a huge requirement for biological research involving the detection and imaging of tumours to be carried forward and advanced upon with simpler, smaller and portable Raman instrumentation.

There have been some reports in recent years where small, portable Raman spectrometers have been employed in areas of biomedical detection. As many cancers and diseases are only diagnosed following rigorous blood tests, often requiring 24 – 48 hours for a return of results and in some more complex cases, up to two weeks, there is requirement for a rapid method of blood analysis and biomarker detection and quantification. Blood analysis of various analytes has been made possible by use of a handheld Raman spectrometer to scan disposable sample strips, paving the way for employment of this technique for the detection of biomarkers relating to a multitude of diseases.[137] Portable Raman systems

have also been employed in the analysis of urine in order to diagnose, analyse and treat various urinary tract conditions therefore allowing a quicker and more applicable treatment route to be prescribed. Additionally, Raman analysis of urinary stones has been shown to provide a rapid result regarding stone sample composition thus allowing prescription of an appropriate course of treatment.[138] Fitting a fibre optic probe to such Raman spectrometers has allowed previously difficult and complicated live samples to be investigated. Resection of bladder cancer tumours *in vivo* by the monitoring of amino acid peaks in the Raman spectra, in suspicious and non-suspicious areas of the bladder, has been made possible by use of a portable 785 nm Raman spectrometer and optical probe attachement.[139]

For optical biomedical research concerning tumours, calcifications and other malignancies *in vivo* to develop it is important to understand the degree in which light can penetrate through tissue, often multiple differing types of tissue, and then 'escape' in order to be identified by a detection source.[140] The optical window for biological tissues is known to exist within the NIR region, over the wavelength range 650 – 1350 nm, where the absorption of light due to components of the tissue is minimal (shown in Figure 28); therefore the majority of current Raman spectroscopy employs the use of 785 nm laser excitation sources for their analysis due this reduced interference and the minimisation of fluorescence often acquired with other excitation wavelengths.[141,142] Penetration of light through tissues in the ultraviolet (UV) region is very poor as the majority of organic molecules absorb light at these wavelengths. Additionally, components within tissue such as haemoglobin and melanin are the main contributing factors of light absorption in the visible region, which is why focus is being placed on the red and NIR wavelengths as these are weakly absorbed by tissues and can penetrate deep into such. However, the depth of penetration with red and NIR excitation wavelengths is limited by optical scattering which has led to the recent interest of the depth of penetration of light of NIR and far-infrared (FIR) wavelengths. Here, it is water within the tissue samples that absorbs most intensely.[140,141]

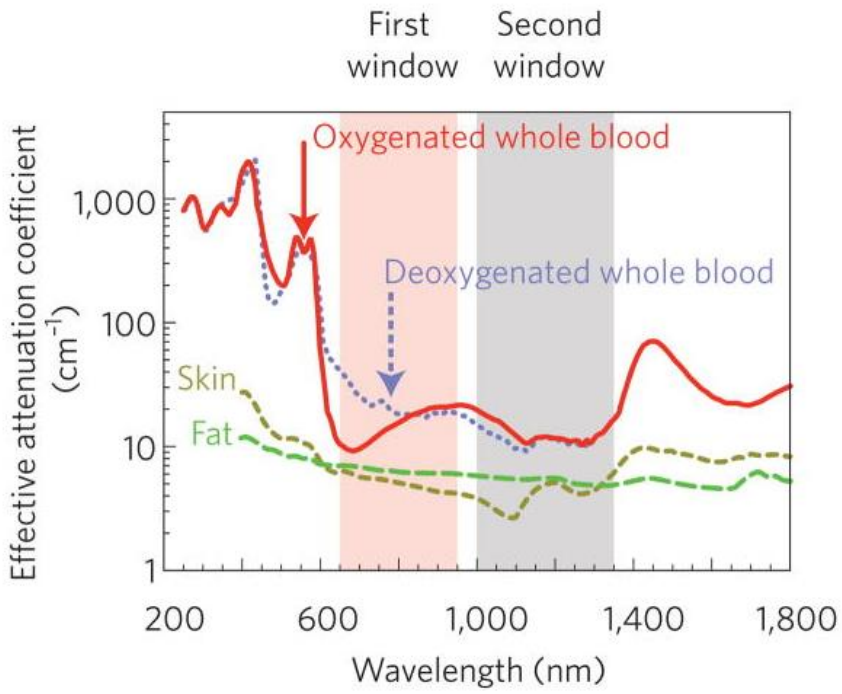

Figure 28 – A plot of the effective attenuation coefficient (log scale) vs wavelength illustrating that the absorption and scatting from oxygenated blood, deoxygenated blood, skin and fatty tissue is lowest in either the first (pink shaded area) or second (grey shaded area) near-infrared window.[141] Reprinted with permission from A. M. Smith, M. C. Mancini and S. Nie, *Second Window for in Vivo Imaging.* Nature Nanotechnology, 2009, 4, 710–711. Copyright (2019) Nature Nanotechnology.

Within this NIR optical window, tissue is somewhat transparent to light. The absorption of light is minimal with scattering being the most dominant light-tissue interaction in which light becomes diffused. As scattering increases, so does the distance and variance in direction at which photons travel through tissues. Therefore, the ability to detect and quantify these photons is of great importance to understanding the depth at which these can be detected using a conventional backscattering Raman spectrometer.

There have been a few reports in literature as of recent, of longer wavelength Raman spectroscopy being used as a potential tool in disease diagnostics. A pilot study has been carried out by Magalhaes *et al.* exploring the ability of a 1064 nm

equipped Raman spectrometer to distinguish between healthy and cancerous prostate cancer samples by evaluating the scattering of differing molecular compounds present in the cancerous tissues, which are not present in the healthy tissues. This was possible by the observed decrease in sample background using a 1064 nm laser compared with 785 nm laser interrogation.[143] Discrimination of cancerous and normal liver tissue has been reported by Pence *et al.* in which they have demonstrated the ability to discriminate between healthy liver tissue and two types of liver carcinoma *via* use of a 1064 nm Raman spectrometer, work previously ineffective with both 785 nm and 830 nm laser excitations due to intense sample autofluorescence.[144]

In order to evaluate the extent at which a commercially available conventional handheld portable Raman spectrometer can penetrate through varying barriers, in particular biological samples, we have recently reported the use of a handheld 785 nm Raman spectrometer for the detection of ethanol through clear plastic barriers up to thicknesses of 9 mm.[145] This work paved the way for the detection of chalcogenopyrylium (CP) dye based nanotags through up to 20 mm plastic and 10 mm tissue using the same commercially available handheld Raman spectrometer in conjunction with chemometrics. This work also deduced a resonance contribution; the depth of penetration achieved was affected by the absorbance of the chalcogenopyrylium dye molecule used in the nanotag. Three CP based dyes with absorbance maxima 676, 823 and 959 nm were employed in these experiments with use of 823 nm dye resulting the greatest depth that a SERS signal could be achieved.[146] With the majority of conventional Raman biological studies employing the use of portable Raman spectrometers fitted with a 785 nm laser, there is scope to explore longer excitation wavelengths in order to exploit the reduced absorption and scattering effects in tissues[92] and as a result penetrate deeper while observing much less spectral background noise than the conventionally used 785 nm excitation wavelength.

To date, little research exists employing longer wavelength Raman spectrometers for depth analysis, specifically handheld portable Raman spectrometers. Here, the depth of penetration of three portable handheld Raman spectrometers, in

conjunction with novel chalcogenopyrylium dye based nanotags, through varying thicknesses of tissue and plastic is reported and compared. Pork tissue samples were used in order to mimic a human tissue model. Any background acquired from these experiments, originating from the plastic and tissue barriers, was not removed in order to assess the depth of penetration in plastic and tissue in regard to what we already know about light absorption and scattering in the NIR optical window. It is also important that for future development and potential clinical translation, that as little data manipulation as possible is carried out ensuring integrity of the results and eliminating the need for complex data processing software and algorithms to be applied.

5.2. Chapter Aims

The aim of this chapter is to assess the depth of penetration abilities of conventional handheld Raman spectrometers in conjunction with a novel class chalcogenopyrylium dye based nanotags upon three excitation wavelengths: 785 nm, 1064 nm and 1280 nm, through increasing depths of both pork tissue and polyethylene terephthalate (PET) and barriers. Dyes with different absorbance maxima are implemented in order to determine if there is a resonance contribution regarding the depth of detection with these nanotags. Additionally, the nanotag signal should be detected little or no data processing, manipulation or background subtraction, in order to assess the ability of these spectrometers to be used in a simple and immediate setting.

5.3. Results and Discussion

5.3.1. Synthesis and Characterisation of Gold Nanoparticles

Synthesis of gold nanoparticles is as reported in section 3.3.1.

5.3.2. Nanotag Design and Functionalisation

As previous group research deduced a resonance contribution in relation to the depth at which CP dye based nanotags can be detected at depth upon 785 nm excitation,[146] these experiments were carried out using two CP dye based nanotags, dye 1 and dye 6, as used in chapters 3 and 4 of this thesis respectively. The chemical structure and absorbance maximum of each dye is reiterated in Figure 29. As three excitation wavelengths are to be deployed in this study, a CP based dye molecule resonant at a wavelength as close to 1280 nm as possible would have been incredibly valuable for comparison of the relationship of the depth of penetration with reporter molecule resonance contribution, however, synthesis of such a molecule has proved incredibly difficult to date and as such these experiments were carried forward using the dye molecules currently in production. In addition, dye 6 is the longest wavelength absorbing CP dye available at present.

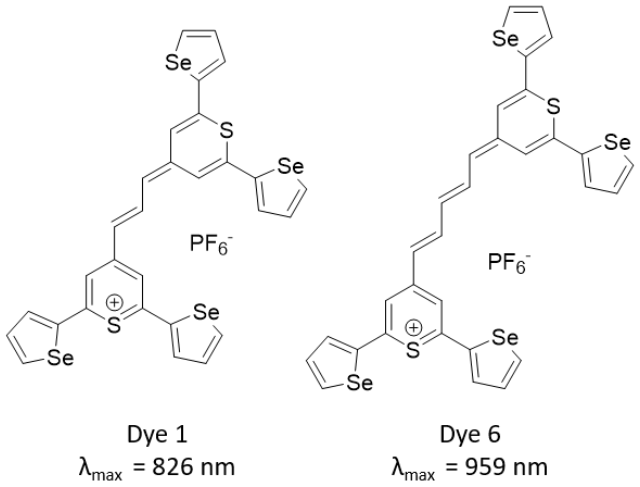

Figure 29 - Chemical structures and absorption maxima of the chalcogenopyrylium dye reporter molecules used in this study.

5.3.3. SERS Measurements

SERS measurements were carried out using: a Snowy Range (now Metrohm Raman) CBEX handheld Raman spectrometer 785 nm, 43 mW laser power, a Snowy Range (now Metrohm Raman) CBEX handheld Raman spectrometer 1064 nm, 30 mW laser power and a portable handheld Raman spectrometer 1280 nm, 28 mW laser power (not commercially available), provided by Professor Neil Shand at DSTL. All spectra were collected using a 3 second integration time.

A glass vial, 2 mL total volume, 15 mm vial diameter, 1 mm wall thickness was filled with each nanotag solution of optimal concentration, as deduced in chapter 3 and chapter 4 (dye 1: 2 mL 500 nM, and dye 6: 2 mL 350 nM) and placed behind the tissue or plastic barrier. A point and shoot adaptor was fitted to the spectrometer, placed in contact with the barrier and the SERS measurement taken (Figure 30). Measurements were taken, as the thickness increased, every 2 mm for the tissue barrier and every 1 mm for the clear plastic barrier. 2 mm was the smallest thickness that the meat could be sliced into and 1 mm was the smallest thickness of plastic sheet available. At this point it should be noted that the focal distance of all three Raman spectrometers is fixed, only one point and shoot adaptor lens was available for each spectrometer therefore variation of the focal distance was not possible. It was postulated that analysing the SERS response these nanotag samples by fixing the distance from the spectrometer to the sample vial and only varying the barrier thickness would be more representative when comparing all three spectrometers of different wavelengths. However, it was established that this would not be representative of a 'real life' scenario. Translation into the clinic, for example, would involve the spectrometer being placed in direct contact with the tissue sample or patient, with the depth of detection initially unknown.

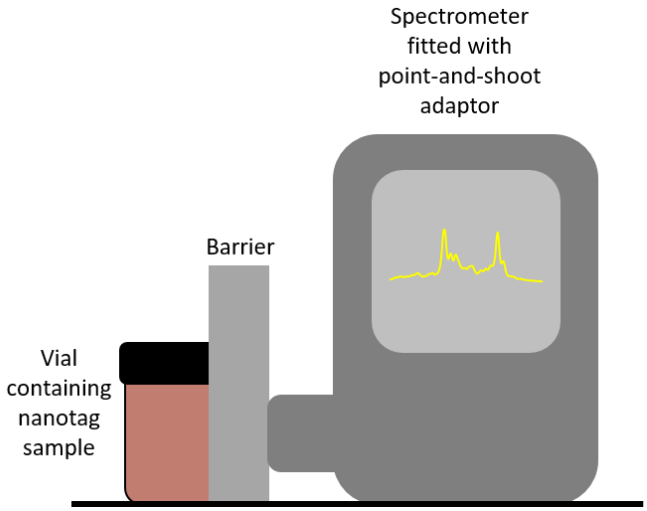

Figure 30 – Cartoon illustration showing the experimental set up for the depth of penetration experiments using portable handheld Raman spectrometers.

The data was processed using Matlab version R2018a, and was baseline corrected, smoothed, normalised and stacked. The baseline correction and smoothing functions applied to these data sets are that of an already established group protocol specifically written for Raman and SERS experiments involving the depth of penetration through varying barriers for these specific spectrometers. This allowed the peaks corresponding to the nanotag and peaks corresponding to the barrier to be viewed and compared with ease. No background corresponding to the tissue or the plastic barriers was removed in order to assess the ability of each spectrometer to 'see through' the barriers.

5.3.3.1. Depth of Penetration through Tissue

The normalised stacked spectra of the nanotag with dye 1 and dye 6, through increasing thicknesses of tissue, at each excitation wavelength, is shown in Figure 31 (785 nm excitation), Figure 32 (1064 nm excitation) and Figure 33 (1280 nm excitation).

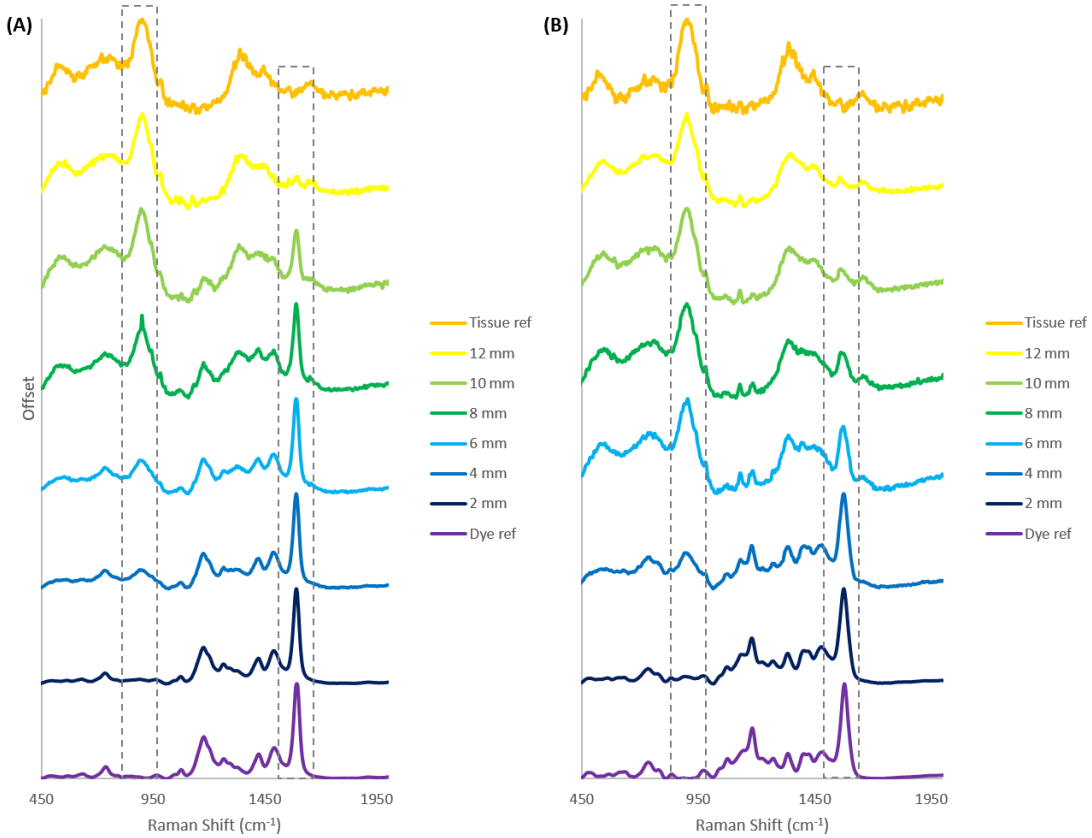

Figure 31 - Average normalised stacked spectra of each nanotag (A) dye 1 and (B) dye 6 through increasing thicknesses of pork tissue. Measured with a laser excitation wavelength of 785 nm, 43 mW laser power and an integration time of three seconds. Each sample was prepared in triplicate with three replicate scans measured at each tissue thickness.

Figure 31 (A) shows that the peak corresponding to dye 1 at 1600 cm^{-1} is visible up to a tissue thickness of 10 mm, beyond which the tissue spectra dominates. There is a small peak at this shift at a depth of 12 mm, however its intensity is less than three times the standard deviation of the blank and therefore cannot be considered a dye peak with certainty. The peak at 907 cm^{-1} resulting from the tissue does not become apparent until a tissue thickness of 4 mm, after which it increases in intensity with increasing tissue thickness. Examining the spectra relating to dye 6, shown in Figure 31 (B), at increasing tissue thicknesses shows the peak at 1579 cm^{-1} visible up to a tissue thickness of 8 mm, after which any apparent dye peaks at this shift are not intense enough i.e., less than three times

the standard deviation of the blank, to be deemed a dye peak with confidence. As with the spectra acquired from a dye 1, the spectral contribution from the tissue becomes apparent at a thickness of 4 mm, increasing in intensity as the thickness of the tissue barrier increases.

The same experiment and spectral analysis was carried out for detection of these nanotags at through increasing thicknesses of pork tissue using a 1064 handheld Raman spectrometer, as shown in Figure 32.

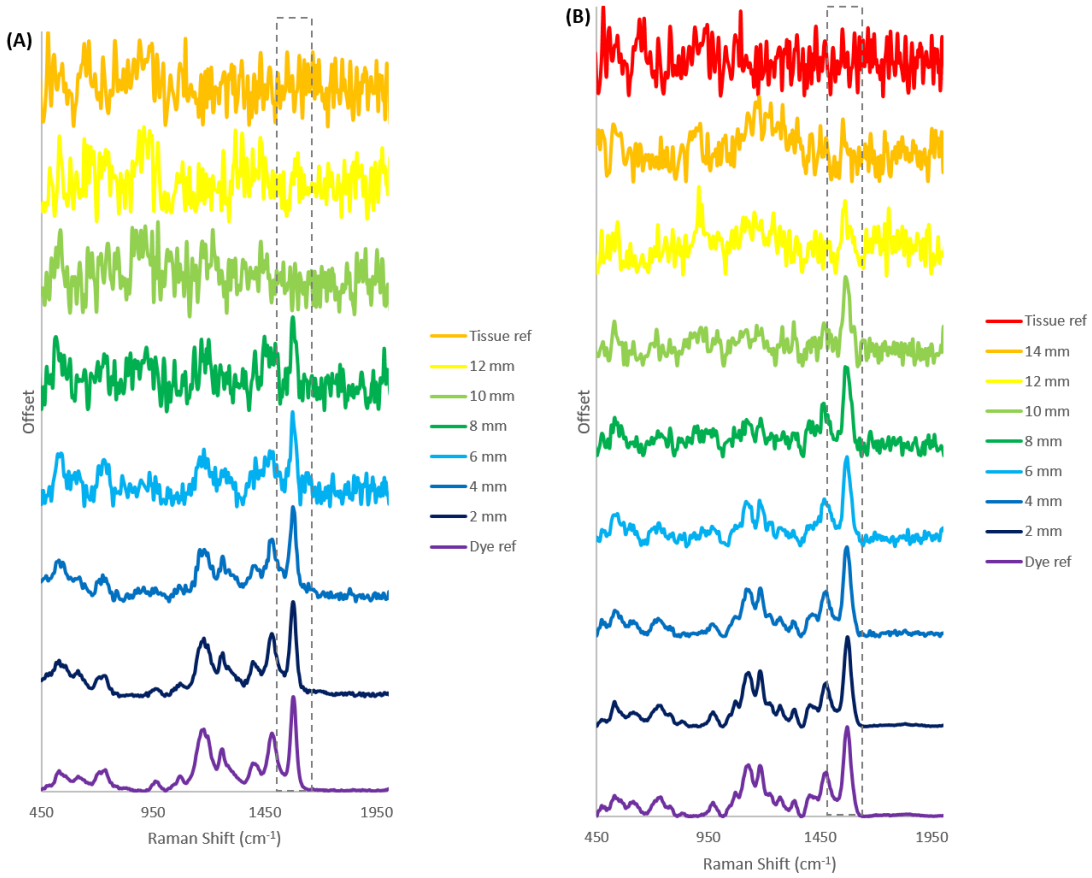

Figure 32 - Average normalised stacked spectra of each nanotag (A) dye 1 and (B) dye 6 through increasing thicknesses of pork tissue. Measured with a laser excitation wavelength of 1064 nm, 30 mW laser power and an integration time of three seconds. Each sample was prepared in triplicate with three replicate scans measured at each tissue thickness.

On examination of the spectra of dye 1 (Figure 32 (A)) through an increasing depth of tissue, the main peak corresponding to the dye at 1589 cm^{-1} is visible up to a tissue thickness of 8 mm after which spectral noise is the dominating characteristic. Similarly, on analysis of the spectra corresponding to dye 6 (Figure 32 (B)) through increasing thicknesses of tissue, the dye peak at 1581 cm^{-1} is visible up to a tissue depth of 12 mm after which the intensity of the peak is not significant enough, i.e. it is less than three times the standard deviation of the blank, to be considered a dye peak with confidence.

This complements previous group work conducted with the same 785 nm handheld spectrometer regarding the relevance of the resonance contribution from the dye and the depth at which the nanotags can be detected.[146] The 826 nm absorbing dye could be detected 2 mm deeper than that of the 959 nm absorbing dye on interrogation with a 785 nm handheld spectrometer, through the tissue barrier. Work carried out, here, with the 1064 nm handheld Raman spectrometer further acknowledges the fact that resonance must be considered to achieve optimal depth with use of the 959 nm resonant dye and the 1064 nm spectrometer being detectable 4 mm deeper than with the 785 nm handheld spectrometer.

It is interesting and important to note that there is significantly less tissue background observed upon interrogation with a 1064 nm laser source compared to that observed with the 785 nm laser. Reasoning for this is thought to be due to the reduced absorption and scattering effects observed with longer excitation wavelengths. Spectral contributions from the tissue, at 785 nm, become evident at tissue thickness of 4 mm, particularly the peaks at 907 cm^{-1}, 1342 cm^{-1} and 1663 cm^{-1}, as depending on the nanotag or Raman reporter molecule used, these tissue peaks could in fact obscure significant peaks of interest. Therefore, the fact that significantly less tissue background was observed with 1064 nm laser excitation is a pronounced advantage over the 785 nm laser excitation.

The same experimental procedures and spectral analysis was carried out for detection of these nanotags at through increasing thicknesses of pork tissue using

a prototype 1280 nm handheld Raman spectrometer, provided by DSTL, as shown in Figure 33.

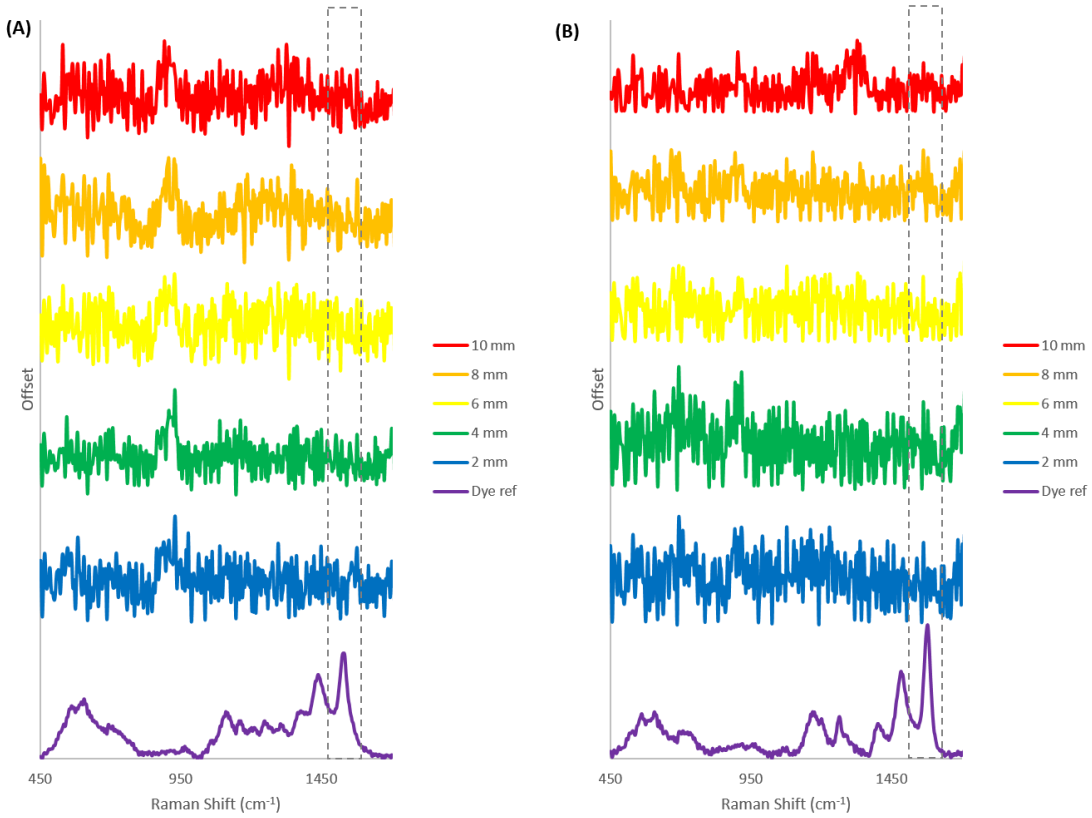

Figure 33 - Average normalised stacked spectra of each nanotag (A) dye 1 and (B) dye 6 through increasing thicknesses of pork tissue. Measured with a laser excitation wavelength of 1280 nm, 28 mW laser power and an integration time of three seconds. Each sample was prepared in triplicate with three replicate scans measured at each tissue thickness.

Figure 33 shows the SERS spectra through increasing thicknesses of tissue relating to (A) dye 1 and (B) dye 6. No spectral contribution from either dye 1 or dye 6, or tissue, is observed at any tissue thickness. It is expected that no nanotag signal was observed through a tissue barrier at 1280 nm laser excitation due to the barrier itself and not necessarily the spectrometer. This is investigated and discussed further in section 5.3.3.3.

A summary of the depth at which each dye could be detected at through increasing thicknesses of tissue at the three different wavelengths is shown below in Table 3.

Table 3 - Summary of the tissue depth at which dye 1 and dye 2 can be detected upon interrogation with a 785, 1064 and 1280 nm laser by note of the depth at which the dyes are visible and the depth at which the tissue is the main contributing spectrum.

Excitation Wavelength (nm)	Dye	Tissue depth at which dye is still visible (mm)	Depth at which tissue is the main contributing spectrum (mm)
785	1	10	12
785	6	8	10
1064	1	8	-
1064	6	12	-
1280	1	0	-
1280	6	0	-

As expected, the depth at which the nanotag signal can be achieved, through pork tissue samples, is dependent on the resonance contribution from the dye used. Using the 826 nm absorbing dye results in a 2 mm greater detection depth with the 785 nm spectrometer than by employing dye 6 (λ_{max} = 959nm). Conversely, using the 959 nm absorbing dye in conjunction with the 1064 nm spectrometer results in a detection depth 4 mm greater than achieved with dye 1 (λ_{max} = 826 nm). By employing the optimal resonant dye for each spectrometer, the 1064 nm Raman spectrometer is able to detect its resonant nanotag 2 mm deeper in the tissue sample than the 785 nm Raman spectrometer and its resonant dye. This demonstrates that, from these experiments, in order to obtain the best possible signal through a tissue barrier, SERRS must be employed.

5.3.3.2. Depth of Penetration through Plastic

Before a reasoning was proposed for why no SERS response was attained at depth with the 1280 nm spectrometer, with either of the dye molecules, but successfully achieved with both the 785 and 1064 nm spectrometers, it was important to assess whether or not the tissue barrier or the spectrometer was the main contributing factor. The same experiments were carried out using a plastic barrier, specifically polyethylene terephthalate (PET). It should be noted that PET is a clear plastic, however as the plastic sections are layered on top of one another, i.e. increasing the plastic barrier thickness, the plastic becomes increasingly opaque.

The normalised stacked spectra of each nanotag through increasing thicknesses of plastic, at each excitation wavelength, is shown in Figure 34 (785 nm excitation), Figure 35 (1064 nm excitation) and Figure 36 (1280 nm excitation).

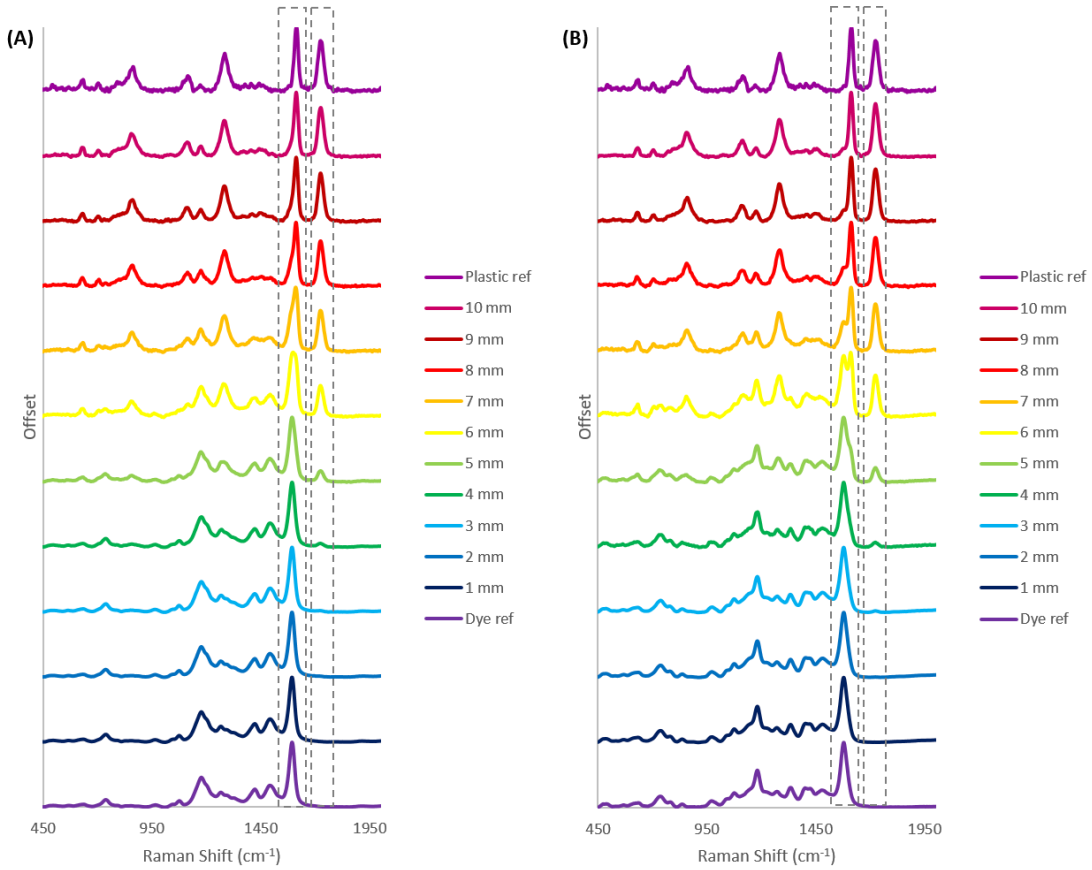

Figure 34 - Average normalised stacked spectra of each nanotag (A) dye 1 and (B) dye 6 through increasing thicknesses of plastic. Measured with a laser excitation wavelength of 785 nm, 43 mW laser power and an integration time of three seconds. Each sample was prepared in triplicate with three replicate scans measured at each plastic thickness.

On examination of Figure 34 (A) and (B), the main peak corresponding to each nanotag (dye 1 nanotag = 1600 cm^{-1}, dye 6 nanotag = 1579 cm^{-1}) appears to dominate in both experiments up until a plastic depth of 5 mm, after which, these peaks start to broaden. A small contribution from the plastic at 1730 cm^{-1} is also apparent. For both experiments, the intensity of this plastic peak gradually increases until the intensity is similar, if not the same as, the intensity of the peak in the plastic reference spectrum. For dye 1, the dye peak (1600 cm^{-1}) begins to broaden at 6 mm eventually shifting to 1617 cm^{-1} at a 7 mm plastic thickness and above. This correlates with the 1617 cm^{-1} peak in the pure plastic spectrum and can be deduced that with a 785 nm excitation wavelength the dye resonant at 826 nm (dye 1) can be confidently viewed, by eye, up to a thickness of 6 mm, after

which the plastic spectrum begins to dominate. For dye 6, the dye peak begins to broaden at a plastic thickness of 5 mm shifting to 1617 cm^{-1} at a 7 mm plastic thickness. The dye peak gradually diminishes becoming a shoulder of the emerging plastic peak with this newly emerged plastic peak dominating at plastic thicknesses including and above 8 mm. It can be argued that dye 6 is confidently visible at plastic thicknesses up to 7 mm when interrogated with a 785 nm laser excitation wavelength. However, although the plastic spectra begins to dominate and the dye peak decreases into a small shoulder within the plastic peak, the dye peak at 1579 cm^{-1} is still visible, by eye at a plastic thickness of 8 – 9 mm.

The same analysis was carried out for detection of these nanotags at through increasing thicknesses of plastic using a 1064 handheld Raman spectrometer, as shown in Figure 35.

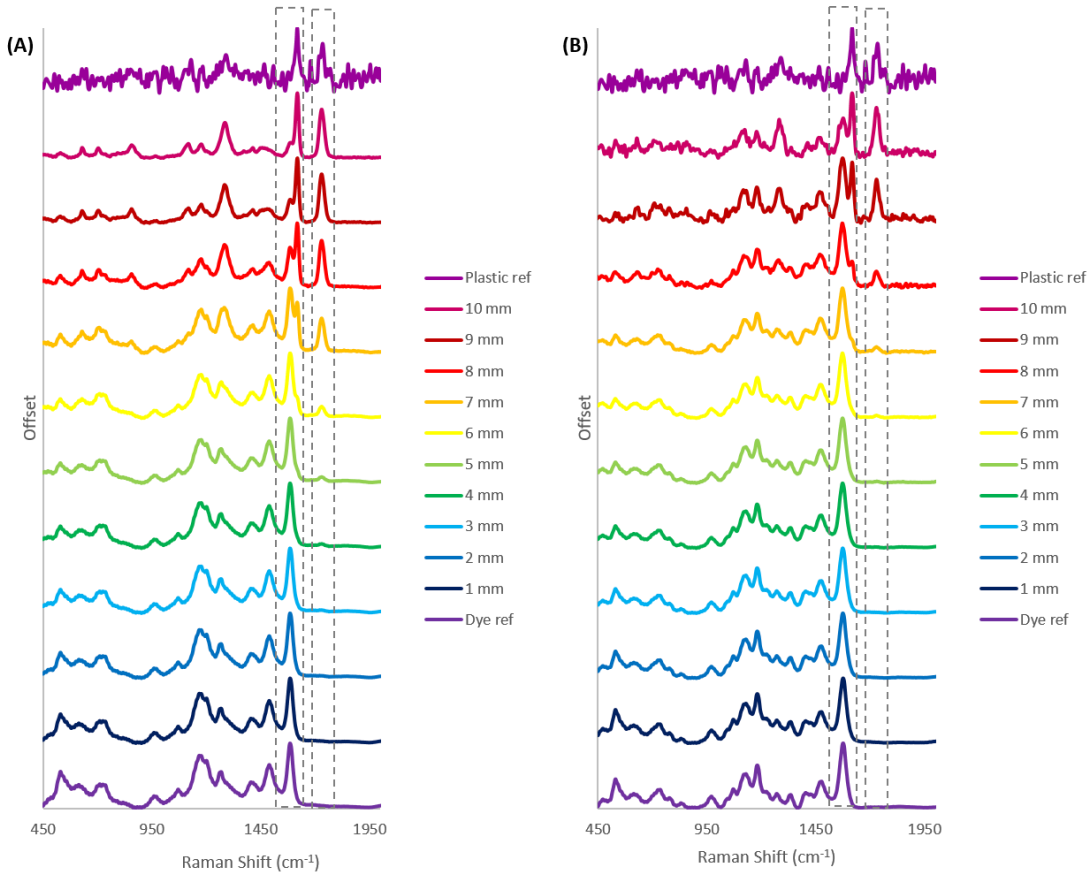

Figure 35 - Average normalised stacked spectra of each nanotag (A) dye 1 and (B) dye 6 through increasing thicknesses of plastic. Measured with a laser excitation wavelength of 1064 nm, 30 mW laser power and an integration time of three seconds. Each sample was prepared in triplicate with three replicate scans measured at each plastic thickness.

The spectral changes that occur upon increasing the thickness of the plastic barrier between each nanotag upon 1064 nm excitation, as shown in Figure 35, vary more so than upon 785 nm excitation. The peak referring to dye 1 (1589 cm^{-1}) is visible until a shoulder, contributed from the plastic, begins to form at 1621 cm^{-1} at a plastic thickness of 6 mm. Beyond this thickness, the peak at 1621 cm^{-1} dominates over the 1581 cm^{-1} peak. It can be argued that this dye peak, now a shoulder of the newly emerged plastic peak, is still observed at a plastic thickness of 10 mm, hence the nanotag is still visible. However, examination of these peaks and the spectra as a whole leads the conclusion that 9 mm is the plastic barrier thickness at which the dye peak is detected, confidently by eye. The main peak corresponding to the plastic (1736 cm^{-1})

begins to appear at a barrier thickness of 4 mm, gradually increasing in intensity as the thickness of the plastic barrier is increased. The peak referring to dye 6; 1581 cm^{-1} is observed up to a plastic thickness of 8 mm, after this a shoulder, produced by the plastic, is observed at 1621 cm^{-1}, which increases in intensity as the plastic barrier thickens, with this shoulder having a higher intensity than that of the dye peak at a plastic thickness of 10 mm. The main peak corresponding to the plastic (1736 cm^{-1}) appears at a plastic thickness of 7 mm and increases in intensity as the thickness of the plastic barrier increases, as expected. As the main peak corresponding to dye 6 is still visible as a shoulder at a plastic thickness of 10 mm and it could be argued that this nanotag is still detectable at this depth However, at a 10 mm plastic thickness the spectrum corresponding to the plastic does dominate the spectrum therefore upon examining the spectra at all thicknesses it can be said that the spectrum corresponding to dye 6 is visible by eye confidently at a plastic thickness of 8 mm.

As with the analysis carried out on the spectra acquired at depth in tissue (section 5.3.3.1) there also appears to be a partial relationship between the resonance contribution of the dye and the depth at which these nanotags can be detected. The 1064 nm spectrometer provides a deeper depth of penetration with both dye 1 and dye 6 than the 785 nm spectrometer. Employing the 1064 nm excitation wavelength, the 959 nm absorbing dye 6 is visible 2 mm deeper than at 785 nm excitation. The same is also true for dye 1, it is visible 2 mm deeper than that at 785 nm. When comparing the optimal laser excitation wavelength, resonant dye combination, dye 6 in conjunction with the 1064 nm laser source outperforms the combination of dye 1 and the 785 nm laser source with a nanotag detection depth 3 mm greater.

Similarly, analysis was conducted for detection of these nanotags through increasing thicknesses of plastic using a 1280 handheld Raman spectrometer, as shown in Figure 36.

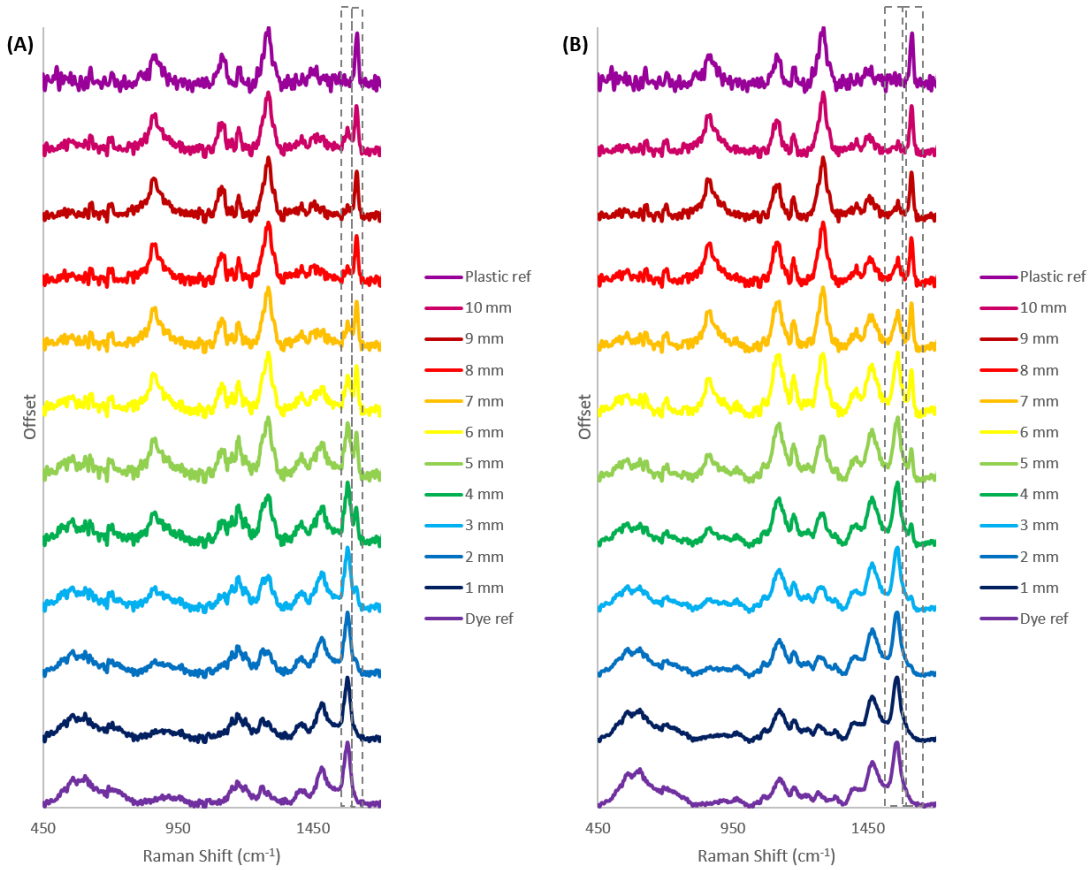

Figure 36 - Average normalised stacked spectra of each nanotag through increasing thicknesses of plastic. Measured with a laser excitation wavelength of 1280 nm, 28 mW laser power and an integration time of three seconds. Each sample was prepared in triplicate with three replicate scans measured at each plastic thickness.

As shown in Figure 36 (A), the main peak that corresponds to dye 1 (1581 cm^{-1}) is observed up to a plastic depth of 6 mm, with a shoulder peak forming at a plastic thickness of 3 mm which increases until, eventually becoming the dominant peak, at a plastic thickness of 7 mm. The main peak corresponding to dye 1 is not visible at thicknesses above 7 mm, and only appears by eye in the 7 mm spectrum however this signal is less than three times the standard deviation of the blank measurement and therefore cannot be said for certainty to be present. There are also additional peaks corresponding to the plastic that become more apparent as the thickness of the barrier increases mainly that of 868 cm^{-1} and 1289 cm^{-1} which both increase in intensity as the thickness of the plastic is increased. As shown in Figure 36 (B), the main peak corresponding to

dye 6 (1559 cm^{-1}) is observed up to a plastic thickness of 8 mm with a shoulder peak corresponding to the plastic (1616 cm^{-1}) becoming apparent at a 3 mm plastic thickness. At a plastic thickness of 9 mm there does appear to be a small contribution at 1559 cm^{-1} from the dye, however, as this intensity is less than three times the standard deviation of the blank it cannot be said with certainty that this is in fact a contribution from the dye and not merely spectral noise. As observed with dye 1, other plastic peaks become apparent as the thickness of the barrier is increase, particularly 868 cm^{-1} and 1289 cm^{-1} again, both increasing in intensity as the thickness of the plastic increases. The plastic thickness at which dye 1 and dye 6 can confidently be observed by use of a 1280 laser excitation is 6 mm and 8 mm respectively.

The resonance contribution in relation to depth is also apparent at 1280 nm excitation. Although not in close resonance, dye 6 (959 nm) is able to be detected 2 mm deeper through the plastic barrier than dye 1 (826 nm). To further confirm this and ascertain whether or not a dye absorbing in resonance with the 1280 nm laser would allow further depth of nanotag detection through a plastic barrier, it would be of great use in the future to design and synthesise a dye absorbing in the region of 1100 - 1300 nm. Attempts so far to synthesise such a molecule have been unsuccessful.

The plastic depth at which the main contributing peak from each dye can be confidently observed by eye is summarised in Table 4. In addition to this, the plastic depth at which the dye peak is still apparent and the depths at which the plastic spectrum dominates are also included in this table.

Table 4 - Summary of the plastic depth at which dye 1 and dye 6 can be detected upon interrogation with a 785, 1064 and 1280 nm laser by note of the depth at which the dyes are visible and the depth at which the plastic is the main contributing spectrum.

Excitation Wavelength (nm)	Dye	Depth at which nanotag is the main contributing spectrum (mm)	Greatest depth at which the main dye peak is visible (mm)	Depth at which plastic is the main contributing spectrum (mm)
785	1	5	6	7
785	6	5	7	8
1064	1	6	8	9
1064	6	8	9	10
1280	1	4	6	7
1280	6	5	8	9

5.3.3.3. The Inability to Probe through Tissue at 1280 nm

No spectra from either nanotag was acquired at depth upon 1280 nm laser excitation through the tissue barrier but was successfully obtained through up to 6 mm and 8 mm of plastic bye use of dye 1 and dye 6 functionalised NPs, respectively, shown in Figure 33. It is known that photons go through multiple diffuse scattering processes at depth, particularly in tissue samples therefore not all of these scattered photons are collected by a conventional back-scattering Raman spectrometer as used in these experiments. As SERS signal is achieved at depth with both 785 nm and 1064 nm laser excitations but not with a 1280 nm laser excitation, it is proposed that the photons scattered by the nanotag, and thus the photons that would return to the detector, are absorbed by components in the tissue matrix and thus not received by the spectrometers detector. The pork tissue samples used in these experiments have a relatively high water content compared to that of general human tissue. Water is, in fact, added to pork during the manufacturing process and could be a factor contributing to this light

absorbance as it is known that water within tissues strongly absorbs light at this wavelength.

It can be stated with confidence that the tissue is preventing the detection of scattered photons, not the Raman spectrometer itself, as intense signal is still achieved from the nanotag solution in a vial without the tissue barrier in place and can be successfully detected at depth of 8 mm through a plastic barrier as shown in Figure 33.

5.4. Chapter Conclusions and Future Work

The depth of penetration of three portable handheld Raman spectrometers in conjunction with chalcogenopyrylium dye based nanotags has been established through both clear plastic (PET) and pork tissue barriers of notable thicknesses. This has been achieved without barrier background subtraction and any complex data processing.

Nanotags can be detected through tissue samples at thicknesses of 10 and 12 mm using 785 and 1064 nm laser excitations respectively. No SERS response, from the nanotags, was achieved by use of the 1280 nm Raman spectrometer at depth through a tissue barrier. This is assumed to be caused by the high water content within the pork tissue samples absorbing the diffuse scattered light from the nanotag sample. It would be of beneficial interest to conduct these experiments employing different tissue models of varying and known water contents in order to consolidate this proposed reasoning and potentially achieve SERS response through a tissue barrier at this wavelength. To further investigate the ability of these conventional handheld Raman spectrometers to detect nanotags at depth, it would be of interest to probe through different types of biological media in addition to tissues of varying water content. For example, breast tissue is predominantly made up of fat, therefore assessing the ability of these spectrometers to probe through fat would be advantageous in furthering the current group work reporting on the depth of penetration, detection and imaging of breast cancer models.

To support this theory, it was important to eliminate the 1280 nm spectrometer as a reason signal was not achieved through the tissue barrier, therefore the same studies involving a clear plastic (PET) barrier were conducted. Nanotag detection depths, through plastic, were achieved at 7 mm with the 785 nm spectrometer, 9 mm with the 1064 nm spectrometer and 8 mm with the 1280 nm spectrometer. This confirmed the lack of SERS response, through pork tissue samples, with the 1280 nm Raman spectrometer was due to the tissue barrier in place, not the Raman spectrometer itself.

A resonance contribution in relation to the depth of penetration in tissue with both 785 and 1064 nm spectrometers was observed. It was noted that using an 826 nm absorbing dye allowed detection 2 mm deeper with the 785 nm spectrometer than using the 959 nm absorbing dye. Conversely, employing the 1064 nm spectrometer allowed nanotag detection 4 mm deeper with the 959 nm absorbing dye than with the 826 nm absorbing dye. The same resonance contribution was evident with the clear plastic (PET) barrier upon 1064 nm laser excitation but not with the 785 nm excitation. Use of the 1064 nm handheld spectrometer resulted in a 2 mm increase in nanotag depth detection with both dye 1 and dye 6. Although not in close resonance with the 1280 nm laser source, dye 6 (λ_{max} = 959 nm) was detected 2 mm deeper through the plastic barrier than dye 1 (λ_{max} = 826 nm), providing further confirmation that Raman reporter molecule resonance must be considered when studies at depth, through barriers, using conventional handheld Raman spectrometer are to be conducted.

It is doubtful that a dye absorbing in the range 1150 – 1300 nm, i.e. in resonance with the 1280 nm laser, would provide a SERS response through the tissue barrier. However, it would still be of interest to evaluate the depth at which such a nanotag could be detected through a plastic barrier upon 1280 nm excitation in order to fully compare the effect of resonance contribution at depth with all three portable handheld Raman spectrometers.

It was important to conduct this work with as little data processing as possible in order to keep this depth detection model as simple as possible, in which nanotag detection at notable depth was achieved. It can be argued that peaks

corresponding to the nanotag spectrum were still present at the deeper barrier thicknesses but could not be confirmed by eye. Therefore, this work should be carried forward investigating the depth of penetration further, perhaps employing chemometrics in order to determine mathematically if the signal of the nanotag is still present at depth.

Detecting nanotags at depth, through tissue samples, in a vial is not representative of real-life scenarios. If these conventional handheld Raman spectrometers were to be employed in biomedical situations, for example, localising these nanotags in tissues and malignant tumours, work should be done to further these detection abilities in more representative samples. Nanotags should be buried or injected at depth in tissues in absence of a sample holder (i.e. a vial, cuvette etc.) and the depth at which SERS signal can be achieved studied. In addition to this, nanotags should be added to cells and buried at depth, again, in order to ascertain a depth at which a SERS response would be achieved allowing determination as to whether or not these conventional handheld Raman spectrometers and nanotags are capable of providing clinically relevant results.

It should be reiterated that this work was carried out using small portable handheld Raman spectrometers no heavier than a few kilograms, indicating the prosperity of this type of instrumentation for easy in-field and clinical translation.

Finally, towards the end of this research, the Detty research group made available a series of alkyne functionalised dye molecules for applications in Raman imaging and SERS. These are expanded upon and studied in section 6.3.4. These nanotags, possessing alkyne functionality, should be studied at depth through tissues, in order to determine if this alkyne signal poses an advantage in detection of the nanotag through biological barriers as this alkyne peak appears in the 'biologically silent' region of the Raman spectrum.

6. Chalcogenopyrylium Based Nanotags for SERS: Cytotoxicity and Detectability in Cells

6.1. Introduction

6.1.1. Introduction of Metallic Nanoparticles and Cells

The behaviour of metallic nanoparticles in cells has become an increasingly interesting and popular area of research due to their unique optical properties, stability and ease of surface modification, making them ideal for application in the study of many biological systems.[147] Metallic NPs have outstanding light scattering properties allowing their interaction with cellular components and localisation within cells to be monitored and studied. Nanoparticles can be taken up into cells by a multitude of different processes. Initially, NPs are largely introduced into cells *via* endocytosis, where the NPs are effectively 'swallowed up' by the plasma membrane of the cell. After the NPs have been engulfed, the section of the cell membrane surrounding the NPs detaches forming an endosome. The cell can easily remove endosomes from itself; therefore the NPs must escape the endosome membrane in order to remain inside the cell.[148] NP surface modification can aid the uptake of NPs into cells, particularly by altering the surface charge allowing interaction with cell membrane receptors as they cross the membrane barrier. This is easily achieved by the functionalisation of positively or negatively charged molecules and / or capping layers onto the NP surface.[149]

6.1.2. Raman Spectroscopy and SERS Analysis of Cells

6.1.2.1. Cell Based Raman Spectroscopy

Once nanoparticles have been engulfed and localised in a cell, they can be analysed using Raman spectroscopy and SERS. Raman spectroscopy and SERS

have been well documented and applied to the imaging of cells for a large variety of applications. Raman spectroscopy of cells provides the opportunity to non-destructively study cells, subcellular components and even intracellular chemical concentrations.[150,151] Due to the growing interest surrounding stem cell therapies, the ability to distinguish and characterise such cells is of great importance in the advancement of stem cell based disease treatments. Mitchell *et al.* have reported the use of Raman spectroscopy, in conjunction with principal component analysis (PCA) to characterise the spectral changes in stem cell culture over a two-week period in order to study the stem cell adipogenic differentiation. This work demonstrated the ability of Raman spectroscopy to detect changes during adipogenesis in a non-invasive, label free means as early as three days into the study.[152] Raman spectroscopy has also been used to map the differences between healthy lung cells and cancerous lung cells by monitoring the cell differences predominantly centralised at the nucleus.[153]

6.1.2.2. Cell Based SERS

Cell based SERS was first demonstrated by Nabive *et al.* where they reported the incubation and detection of silver NPs in cancer cells and presented the ability to detect doxorubicin, an anticancer drug commonly used in chemotherapy, in differing areas of the cell using SERS. The doxorubicin functionalised NPs were predominantly found to localise in the cell nucleus.[154] Since this study in 1991, SERS has been used to detect and study a variety of biological markers of cellular function,[155] cellular stress responses[156] and cell apoptosis and necrosis.[157] SERS analysis of cells can be conducted label-free or with the aid of Raman reporter and targeting molecules. Using bare, non-functionalised NPs can result in a SERS signal as bare NPs can spectrally enhance components surrounding them in the cells. NPs can also be functionalised with Raman reporters and / or targeting molecules providing a strong SERS response with the ability to localise in specific areas of the cell. Using SERS to study the uptake of NPs into cells by addition of specific recognition molecules is widely reported. Zhai and co-workers have reported the use of SERS to monitor NPs entering cells by targeting the folate receptors. They achieved this by functionalising para-aminothiophenol (p-ATP)

and folic acid modified beta-cyclodextrin onto NPs. As the folic acid has a high affinity for the folate receptor, which is over expressed in many diseased cells, they were able to monitor the cell uptake of these NPs using SERS. This study provides ground to effectively study the influence of folate receptor targeting drugs, such as dihydroartemisinin, by quantifying the amount of NPs present in the diseased cells before and after drug treatment.[158]

6.1.2.3. Raman and SERS Analysis of Alkynes

Raman and SERS analysis in bioanalytical applications often encounters challenges due to biological background interference of the analyte's Raman signal. Use of alkyne functionalised probes and NP based tags in bioimaging is advantageous due to the lack of background alkyne signals throughout cells, tissues and other biological media. The first use of alkyne imaging in cellular applications was reported by Yamakoshi *et al.* where they were able to track the degree of cell proliferation by monitoring an alkyne moiety within 5-ethynyl-2'-deoxyuridine (EdU), a thymidine derivative present in the DNA of cells which have undergone divison.[107] Since then, alkyne groups have been incorporated into a multitude of biological Raman applications.

Kennedy *et al.* has shown the ability to image the antibiotic class of β-lactams, in human cell models, by use of terminal alkyne functionalised silver NPs and SERS. The close proximity of the alkyne moiety to the AgNPs allowed intense alkyne SERS signal to be achieved due to the high degree of enhancement along the plane of the metal – alkyne bond.[159] The advantages of the biologically silent alkyne signal has also been employed in applications involving the imaging of cancerous and non-cancerous tissue samples using SERS. Li *et al.* reported the design and synthesis of various structured alkyne containing molecules and antibody functionalised SERS tags for the detection of breast cancer in tissue samples. These cancer-specific, background free SERS nanotags allowed multiplex detection, by means of the position of the alkyne peak, of various breast cancer biomarkers expressed in the tissue samples obtained from patients.[160]

6.1.3. Cell Based SERS for *in vivo* and *ex vivo* Applications

Recently there has been an increasing focus on the use of nanotags to detect and image tumours and tumour models with good quality spectral intensity and resolution. Following the successful construction of chalcogenopyrylium (CP) dye molecules for SE(R)RS nanotag development there have been recent reports in literature of both *in vivo* and *ex vivo* applications by use of these CP based nanotags. By use of spatially offset Raman spectroscopy (SORS) CP dye based nanotags have been detected at depth, through up to 15 mm of pork tissue in multicellular tumour spheroids (MTS) as an *ex vivo* cancer tumour model.[136] This was then advanced upon this with the ability to detect and multiplex three of these CP based nanotags through up to 10 mm of tissue.[161] Additionally, Harmsen *et al.* have shown the use of targeted CP based nanotags by use of AuNPs functionalised with both a CP reporter molecule and an epidermal growth factor receptor (EGFR) specific antibody to successfully target cancerous prostate tumours *in vivo.*[106] These reports of CP dye based nanotags in biological sensing are promising and provide scope for further bio applications but thus far, their toxicity is unreported.

Dye 1 – 6 functionalised NPs were applied to human prostate cell (PNT2) populations in order to determine their cytotoxicity in addition to their detectability using SERS. These nanotags were imaged in order to compliment the toxicity study and determine if, at these concentrations, the nanotags would actually accumulate and be detectable inside cells and would therefore be detectable at the optimal concentrations deduced in chapters 3 and 4. It is anticipated this work will provide a stable proof of concept regarding the toxicity and potential of these nanotags to be developed for future *in vitro / in vivo* applications.

6.2. Chapter Aims

The aim of this chapter was to evaluate the cytotoxicity of five CP based gold nanotags used throughout this thesis, against a healthy cell line in order to assess their suitability for future biological applications. Two of these dyes have been

employed in cellular and cellular tumour model studies but the toxicity of these has not yet been studied or reported.[106,136,146] This chapter also seeks to assess the ability of these nanotags to be detected in cells in varying concentrations using SERS.

6.3. Results and Discussion

6.3.1. Synthesis and Characterisation of Gold Nanoparticles

Synthesis of gold nanoparticles is as reported in section 3.3.1.

6.3.2. Chalcogenopyrylium Gold Nanotag Toxicity Study

6.3.2.1. Cell Viability Indicator / Assay Selection

The toxicity of all nanotags employed in this thesis were investigated using Trypan Blue as a live/dead stain therefore allowing the cells to be easily counted under a microscope in a haemocytometer. Trypan Blue is employed in dye exclusion tests, in order to assess cell viability, where the number of viable cells can be determined on the basis that dead cells have a compromised membrane and thus cannot regulate uptake of the dye in the way that healthy viable cells can.[162] This allows any dead cells that were not removed, during the washing of the cell culture plate, to be easily visible and therefore discounted from the examination and cell count. Initially it was thought that an AlamarBlue assay followed by a SYTOX green nucleic acid stain would be a suitable method for evaluating cytotoxicity. AlamarBlue is used as an indicator of healthy cells, it contains a non-fluorescent active ingredient, resazurin, which is reduced to a highly fluorescent molecule, resorufin, on entering healthy viable cells. This fluorescent signal will decrease over time due to the natural reducing power of healthy cells.[163,164] SYTOX green describes the opposite; SYTOX green nucleic acid stain is a fluorescent indicator for cells with already compromised membranes. Therefore, the lower the florescence signal from the SYTOX green, the healthier the cells.[165] However, as the aim of this chapter was to evaluate the toxicity of CP based nanotags, and not solely the CP dyes, the measurement of fluorescence,

from both these assays and stains, as an indicator of cell viability was not suitable as gold nanoparticles are able to quench fluorescence therefore could potentially obscure the cytotoxicity results obtained. Trypan Blue as a method of healthy cell staining for ease of cell counting under a microscope was therefore carried forward.

6.3.2.2. Nanotag Toxicity Study

Human prostate cells (PNT2) were incubated for a 24-hour period with the optimal concentration for each nanotag, established in chapter 3, in cells at four final concentrations; 1.25 nM, 12.5 nM, 125 nM and the optimal 1280 nm SERS concentration, which differed slightly for each nanotag is shown in Table 5.

Table 5 - The optimal concentration of each nanotag upon 1280 nm laser excitation based on the peak intensity at approximately 1590 cm^{-1}.

Dye	Optimal concentration (nM)
1	500
2	450
3	500
4	350
6	350

The nanotag-cell samples were then stained with Trypan blue and counted using a haemocytometer. Trypan blue does not require an incubation period with samples; therefore analysis can be carried out immediately. The results of the Trypan blue stain and count are shown in Figure 37. The percentage viability values were calculated based on ideal cell conditions (healthy cells in uncompromised media) and were therefore considered to be 100% viable. These experimental counts were carried out in triplicate on three replicate samples.

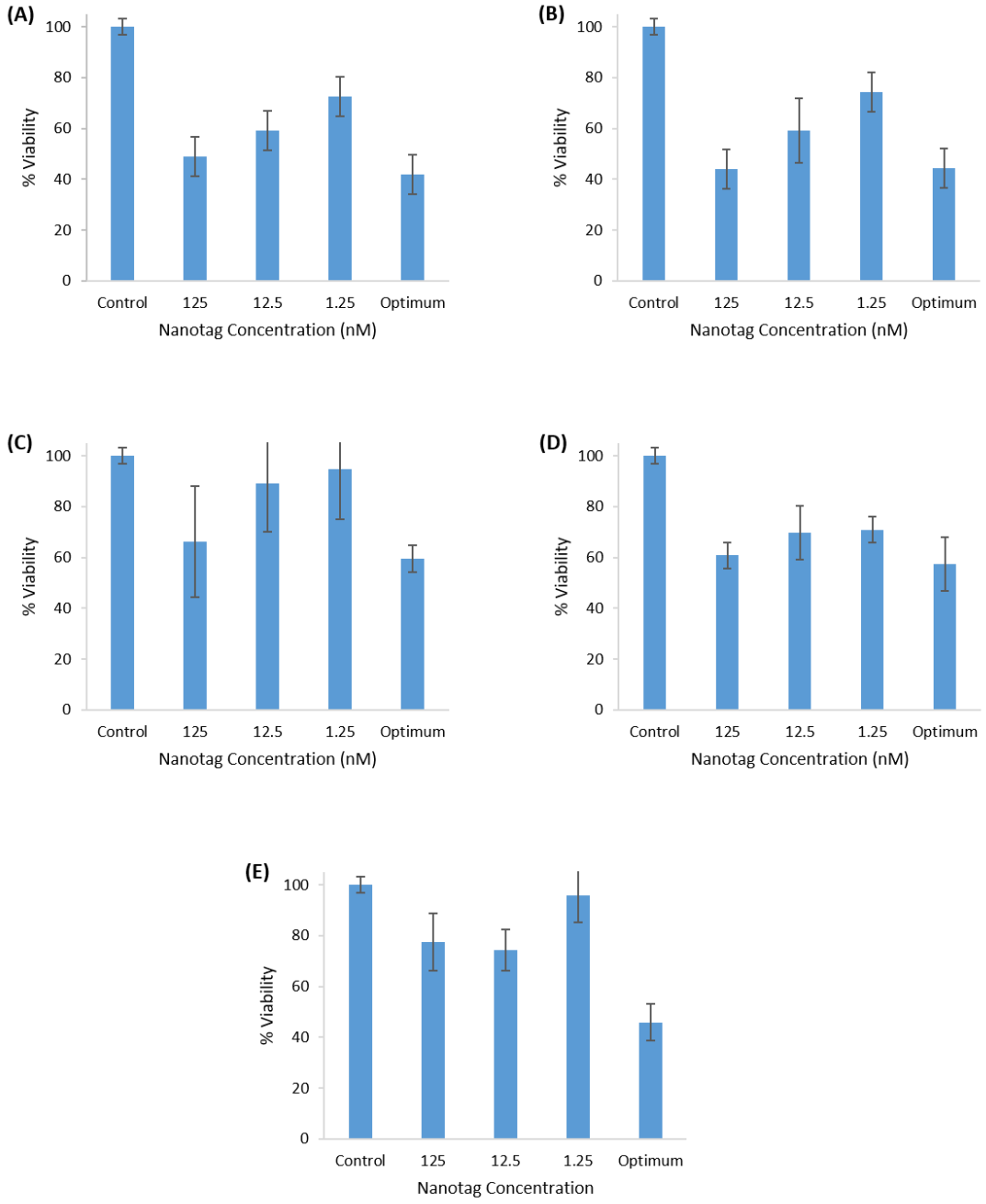

Figure 37 - Cell cytotoxicity results shown in bar chart format for the chalcogenopyrylium-based nanotags (A) dye 1, (B) dye 2, (C) dye 3, (D) dye 4 and (E) dye 6 over four final nanotag in cell concentrations of: 1.25 nM, 12.5 nM, 125 nM and the optimal concentration for each nanotag: dye 1 = 500 nM, dye 2 = 450 nM, dye 3 = 500 nM, dye 4 = 350 nM, dye 6 = 350 nM, evaluated using a Trypan blue stain. Percentages were calculated based on a control sample (100% healthy cells in media). Error bars are ± one standard deviation based on three replicate measurements of three replicate samples.

The results indicated that generally, the higher the final concentration of CP dye on particle, the greater number of cells were compromised. However, in comparing the optimal concentration of each CP dye based nanotag, the percentage of viable cells is very similar to that of the much higher optimal SERS concentration concluding that at concentrations greater than or equal to 125 nM, the toxicity of the CP based nanotags plateaus and approximately 40 – 60 % of the cell populations survive. This is outlined in Table 6.

Table 6 – Comparison of the percentage viabilities of 125 nM nanotags with the percentage viabilities their optimal concentrations.

Dye	% Viability at 125 nM	% Viability at optimal concentration
1	49	42
2	44	44
3	66	59
4	61	57
6	77	46

It would be beneficial to conduct a cytotoxicity study at concentrations 125 nM up to the optimal concentration of each dye in order to confirm if cell toxicity does in fact plateau over this concentration range.

Initially, these cytotoxicity results do not appear entirely feasible in that only 40 - 60 % of these cells remain healthy and viable; however if a future, and already eluded to, application of these nanotags includes the localisation in tumours *in vivo* for imaging and detection, then cell death could be advantageous if this could be controlled and limited to the malignant cells and tissues leaving the surrounding healthy cells and tissues unaffected.

It is interesting to compare the percentage viability values of dyes 1 and 6 at 125 nM in relation to their structure; both dyes are almost identical in structure

with the only difference being the length of the main body of the molecule. Dye 1 is a trimethine dye and dye 6 is a pentamethine dye. These values suggest that the pentamethine dye functionalised nanoparticles are less toxic to the cell population than the identical trimethine dye functionalised nanoparticles. Further work should be carried out comparing the percentage viability values of other identical trimethine and pentamethine dyes in order to determine if this relationship can be fully established. This would be important information in the future design of these CP based dyes specifically for cellular applications.

6.3.3. *In-vitro* SERS Imaging of CP Dye Based Nanotags

In addition to evaluating the toxicity of these nanotags, it was important to assess their detectability at these concentrations, using SERS, in cells. Due to the various bio-imaging, therapeutic and diagnostic applications of AuNPs there is a need for SERS nanotags capable of producing intense intracellular signals at NIR excitation wavelengths. Ideally this imagining would be carried out at a 1280 nm excitation wavelength however, instrumental constraints meant this was not a possibility at this time. Both 1280 nm spectrometers in possession are portable units with fixed laser apertures and sample mounts, therefore preventing variation in focus and mapping from being carried out. Additionally, a faulty 785 nm laser source within the Raman microscope system meant that this work was carried out with a 633 nm laser excitation source as a proof of concept.

As in section 6.3.2, human prostate cells (PNT2) were incubated for a 24-hour period with the optimal concentration for each nanotag (established in chapters 3 and 5) three final in cell concentrations of; 1.25 nM, 12.5 nM and 125 nM. The concentration of cells in each sample was $1x10^6$ cells per sample well. These cells were then fixed onto glass coverslips, by use of paraformaldehyde (PFA), for analysis. Samples were analysed using a Renishaw inVia Raman spectrometer with a 633 nm excitation wavelength (500 mW, 10% laser power), 1800 mm^{-1} grating, ×50 objective (NA = 0.75), an integration time of 0.2 seconds, centred at 1300 cm^{-1} therefore, over the spectral range of

715 - 1829 cm^{-1}, with a step size of 1 μm. All spectra were processed using Renishaw WiRE 4.4 software.

False colour images were obtained using direct classical least square (DCLS) analysis, built into the WiRE 4.4 software. DCLS finds the linear combination of spectra that closely resembles a given reference spectrum, in this case, the reference spectra was the solution spectra of each nanotag obtained using this spectrometer. From this, false colour images can be created by assigning a colour range of varying intensity to the pixels which match the reference spectrum. The minimum intensity of each pixel in every sample analysed was set to 0.3 to ensure consistency across samples and to confirm that the signal from the pixel, corresponded to that of the nanotag and was not signal achieved from potential SERS enhancement of cellular components. The white light image and false colour image of a cell for each nanotag concentration sample is shown. The nanotag reference spectrum overlaid with the spectrum acquired while imaging the cell is overlaid. The spectra have been baseline corrected, normalised and any cosmic rays were removed in order to clearly view the spectrum acquired from inside the cell was in fact that of the reference spectra.

The white light images, false colour images and spectra for cells containing dye 1 functionalised nanoparticles are shown in Figure 38, Figure 39 and Figure 40.

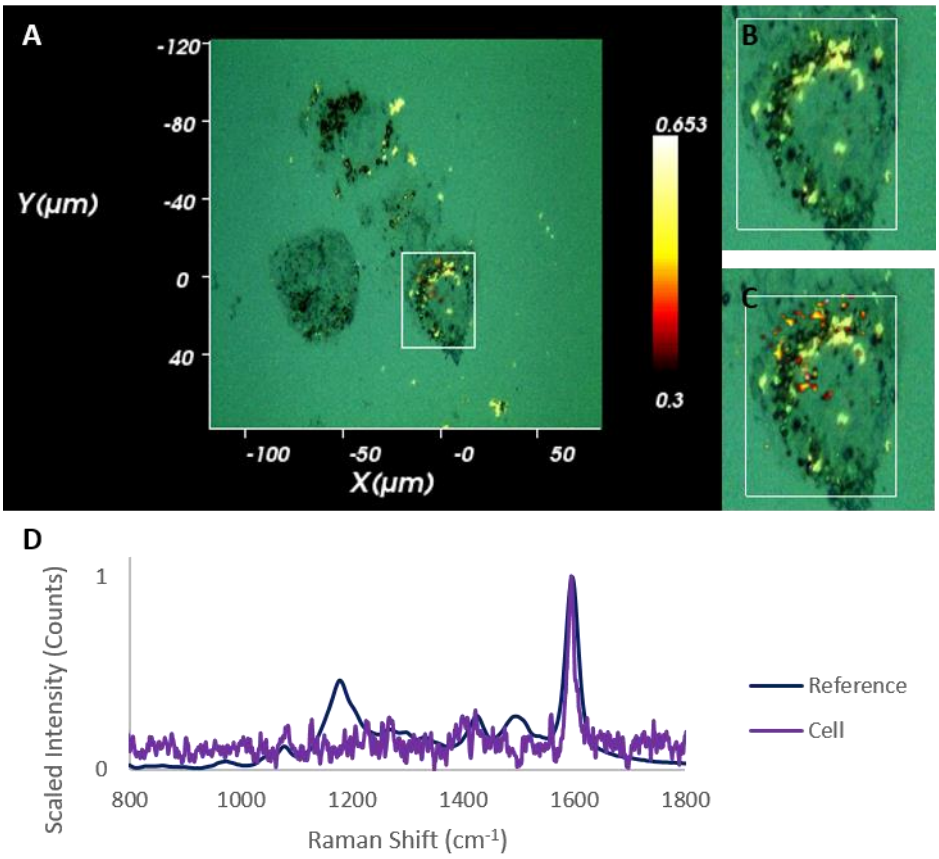

Figure 38 – Dye 1 functionalised gold nanoparticles (final nanotag concentration in cells 1.25 nM) incubated for 24 hours with the cells directly onto glass coverslips. (A) image of the cell with intensity scale bar. (B) white light image of the cell. (C) white light image of the cell with overlaid with a false colour intensity map calculated using DCLS. (D) representative cell spectrum from the mapped cell at a point of intensity signal overlaid with the reference spectrum for dye 1. The cell sample was analysed at 633 nm, 10% laser power (500 mW), 0.2-second acquisition time, centred at 1300 cm^{-1} and a step size of 1 µm.

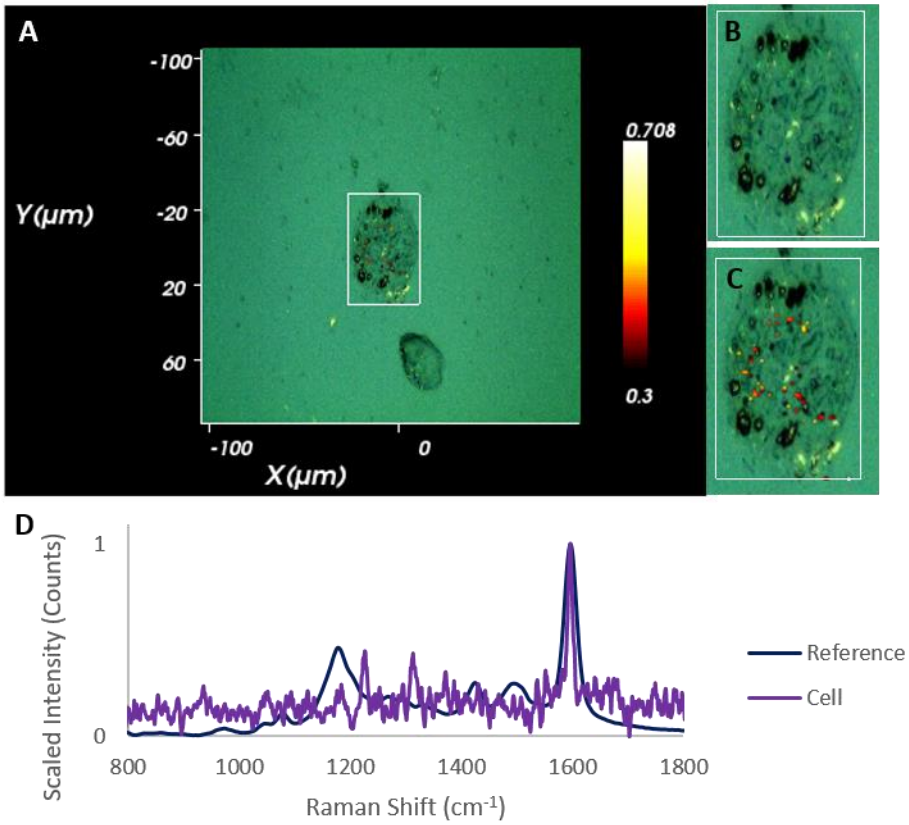

Figure 39 - Dye 1 functionalised gold nanoparticles (final nanotag concentration in cells 12.5 nM) incubated for 24 hours with the cells directly onto glass coverslips. (A) image of the cell with intensity scale bar. (B) white light image of the cell. (C) white light image of the cell with overlaid with a false colour intensity map calculated using DCLS. (D) representative cell spectrum from the mapped cell at a point of intensity signal overlaid with the reference spectrum for dye 1. The cell sample was analysed at 633 nm, 10% laser power (500 mW), 0.2-second acquisition time, centred at 1300 cm^{-1} and a step size of 1 µm.

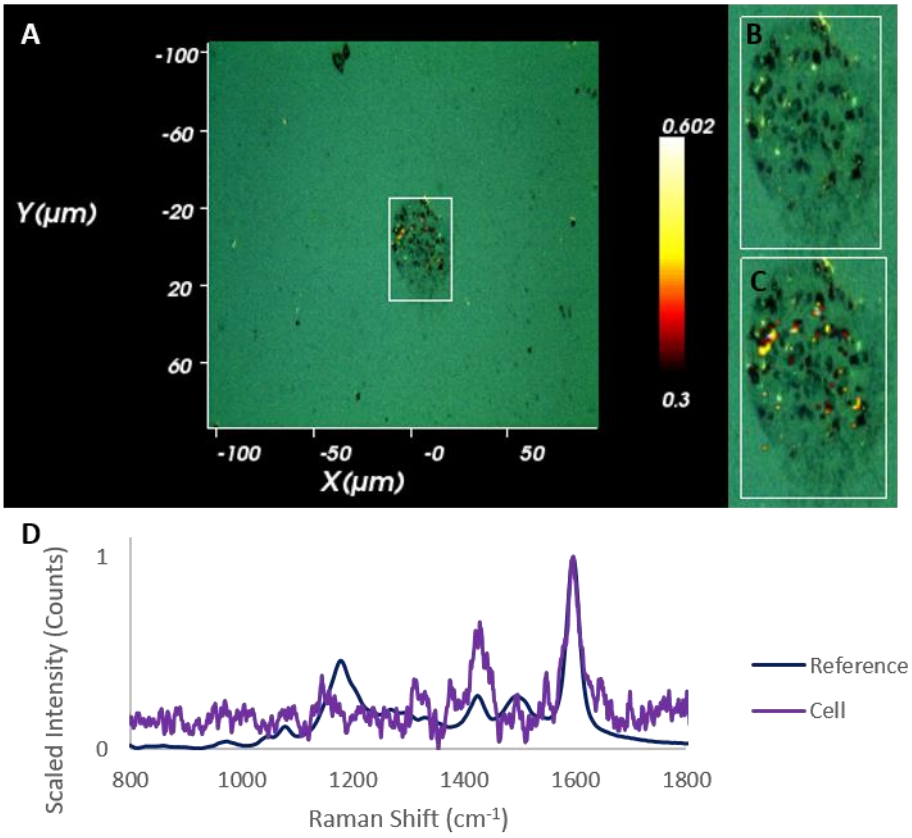

Figure 40 - Dye 1 functionalised gold nanoparticles (final nanotag concentration in cells 125 nM) incubated for 24 hours with the cells directly onto glass coverslips. (A) image of the cell with intensity scale bar. (B) white light image of the cell. (C) white light image of the cell with overlaid with a false colour intensity map calculated using DCLS. (D) representative cell spectrum from the mapped cell at a point of intensity signal overlaid with the reference spectrum for dye 1. The cell sample was analysed at 633 nm, 10% laser power (500 mW), 0.2-second acquisition time, centred at 1300 cm^{-1} and a step size of 1 µm.

The false colour images corresponding to the areas of nanotag SERS obtained for dye 1 over this concentration range do exhibit signal from within the cell boundary, sparsely scattered throughout the cell, with some nanotag signal localised around the cell membrane, with no background signals present out with the cell membrane. Localisation of the nanotags around the cell membrane could be due to the image being acquired at a point in the cell cycle where the cell was attempting to uptake or remove the nanotag containing endosomes. Further time studies would be required to confirm this. Another possibility is that the nanotags

are ‘stuck’ to the cell surface, particularly around the cell edges. This will be discussed following all of the nanotag-cell observations. A prominent peak from this dye is observed in the cellular spectrum at each of the three concentrations at 1595 cm^{-1} correlating with the nanotag solution spectrum overlaid (dark blue). The highest concentration of nanotag, 125 nM, also appears to display a broad and noisy band corresponding to the vibration at 1428 cm^{-1} in the reference spectrum as shown in Figure 40. This would be expected as the final concentration of nanotag increases by two orders of magnitude.

The white light images, false colour images and spectra for cells containing dye 2 functionalised nanoparticles are shown in Figure 41, Figure 42 and Figure 43.

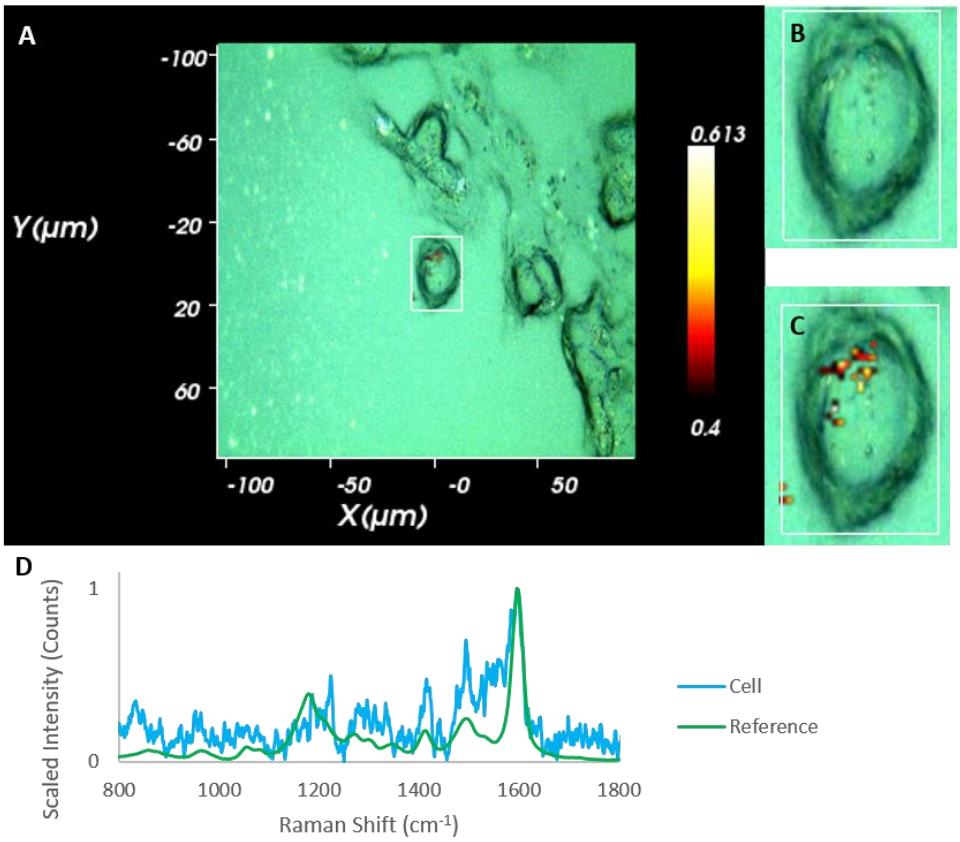

Figure 41 - Dye 2 functionalised gold nanoparticles (final nanotag concentration in cells 1.25 nM) incubated for 24 hours with the cells directly onto glass coverslips. (A) image of the cell with intensity scale bar. (B) white light image of the cell. (C) white light image of the cell with overlaid with a false colour intensity map calculated using DCLS. (D) representative cell spectrum from the mapped cell at a point of intensity signal overlaid with the reference spectrum for dye 1. The cell sample was analysed at 633 nm, 10% laser power (500 mW), 0.2-second acquisition time, centred at 1300 cm^{-1} and a step size of 1 µm.

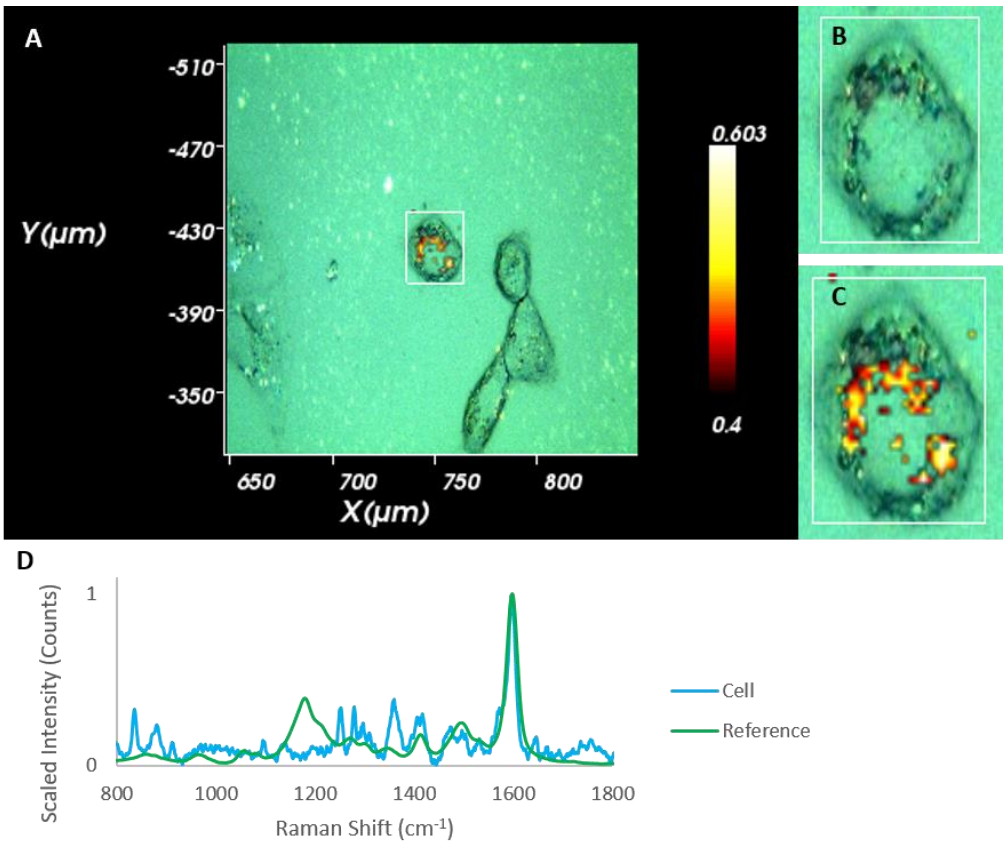

Figure 42 - Dye 2 functionalised gold nanoparticles (final nanotag concentration in cells 12.5 nM) incubated for 24 hours with the cells directly onto glass coverslips. (A) image of the cell with intensity scale bar. (B) white light image of the cell. (C) white light image of the cell with overlaid with a false colour intensity map calculated using DCLS. (D) representative cell spectrum from the mapped cell at a point of intensity signal overlaid with the reference spectrum for dye 1. The cell sample was analysed at 633 nm, 10% laser power (500 mW), 0.2-second acquisition time, centred at 1300 cm^{-1} and a step size of 1 µm.

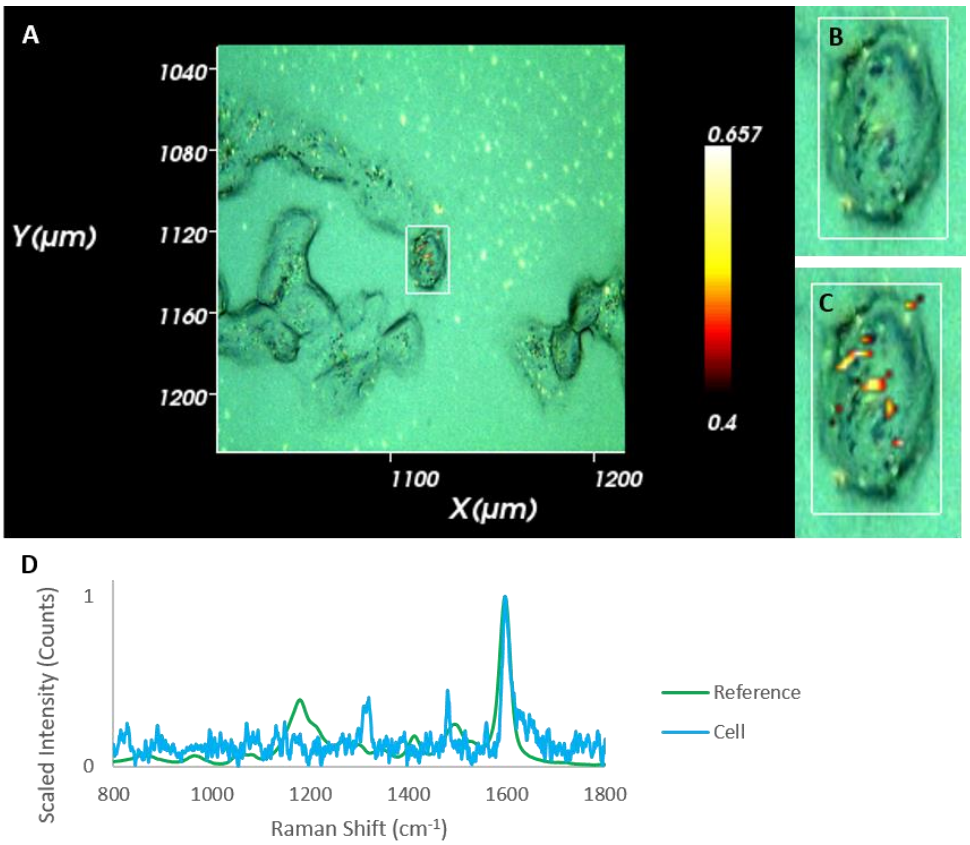

Figure 43 - Dye 2 functionalised gold nanoparticles (final nanotag concentration in cells 125 nM) incubated for 24 hours with the cells directly onto glass coverslips. (A) image of the cell with intensity scale bar. (B) white light image of the cell. (C) white light image of the cell with overlaid with a false colour intensity map calculated using DCLS. (D) representative cell spectrum from the mapped cell at a point of intensity signal overlaid with the reference spectrum for dye 1. The cell sample was analysed at 633 nm, 10% laser power (500 mW), 0.2-second acquisition time, centred at 1300 cm^{-1} and a step size of 1 µm.

Here, the false colour images corresponding to areas of SERS signal intensity show a greater degree of uptake and localisation within the cells, of all three nanotag concentrations, with the nanotags grouping together inside rather than scattering throughout the cell as with the dye 1 functionalised nanotags. There are a few pixels present out with the boundary of the cell and this is thought to be caused by incomplete washing of the slide during the PBS and water wash steps. A prominent peak at the vibration at 1597 cm^{-1} is visible at all three concentrations, corresponding to the reference nanotag solution spectrum

(shown in green). This was as expected as this peak generally tends to be the most intense with all of the chalcogenopyrylium based nanotags studied.

The white light images, false colour images and spectra for cells containing dye 3 functionalised nanoparticles are shown in Figure 44, Figure 45 and Figure 46.

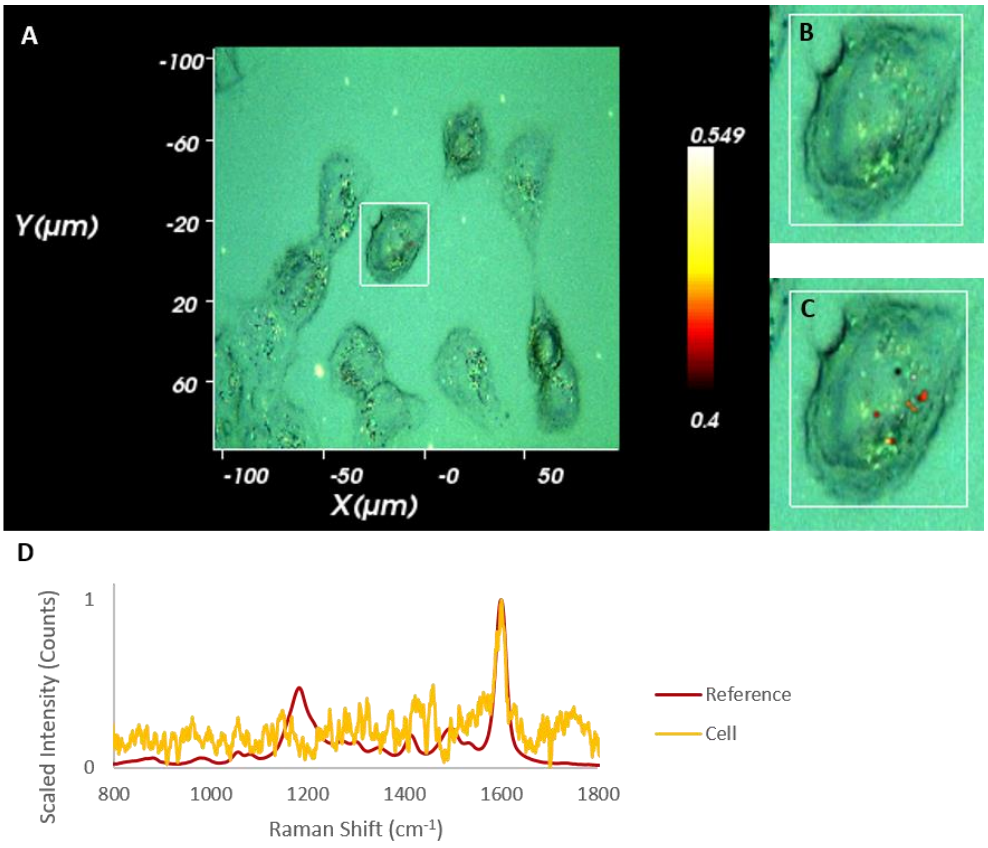

Figure 44 - Dye 3 functionalised gold nanoparticles (final nanotag concentration in cells 1.25 nM) incubated for 24 hours with the cells directly onto glass coverslips. (A) image of the cell with intensity scale bar. (B) white light image of the cell. (C) white light image of the cell with overlaid with a false colour intensity map calculated using DCLS. (D) representative cell spectrum from the mapped cell at a point of intensity signal overlaid with the reference spectrum for dye 1. The cell sample was analysed at 633 nm, 10% laser power (500 mW), 0.2-second acquisition time, centred at 1300 cm^{-1} and a step size of 1 µm.

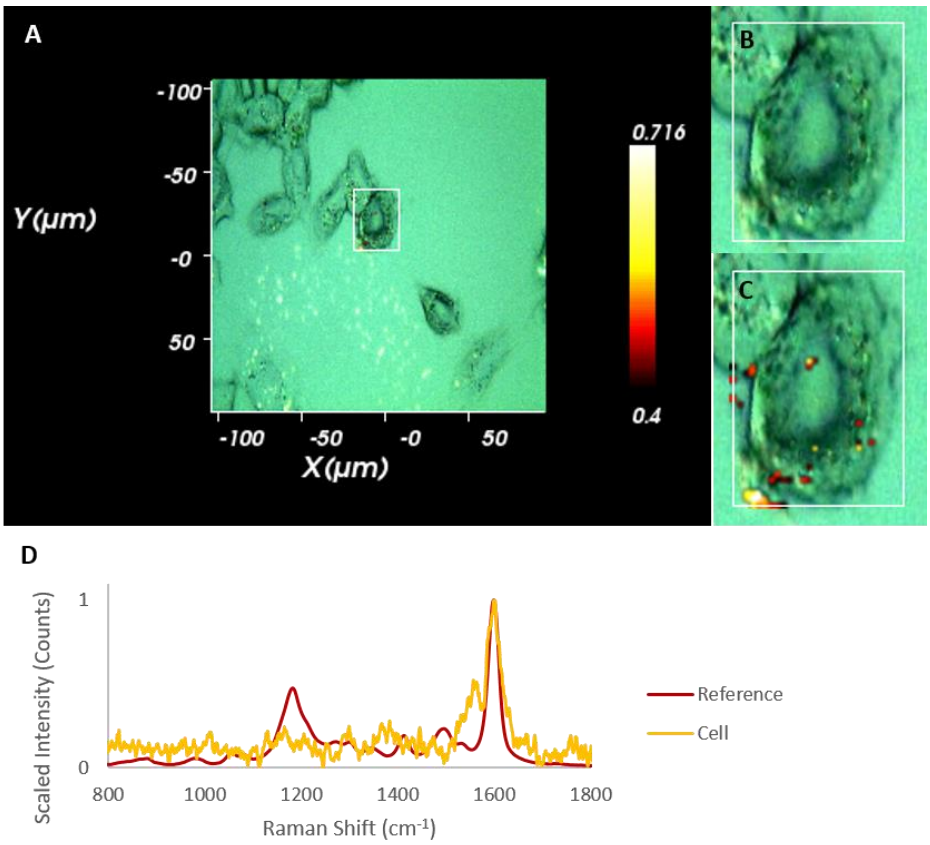

Figure 45 - Dye 3 functionalised gold nanoparticles (final nanotag concentration in cells 12.5 nM) incubated for 24 hours with the cells directly onto glass coverslips. (A) image of the cell with intensity scale bar. (B) white light image of the cell. (C) white light image of the cell with overlaid with a false colour intensity map calculated using DCLS. (D) representative cell spectrum from the mapped cell at a point of intensity signal overlaid with the reference spectrum for dye 1. The cell sample was analysed at 633 nm, 10% laser power (500 mW), 0.2-second acquisition time, centred at 1300 cm^{-1} and a step size of 1 µm.

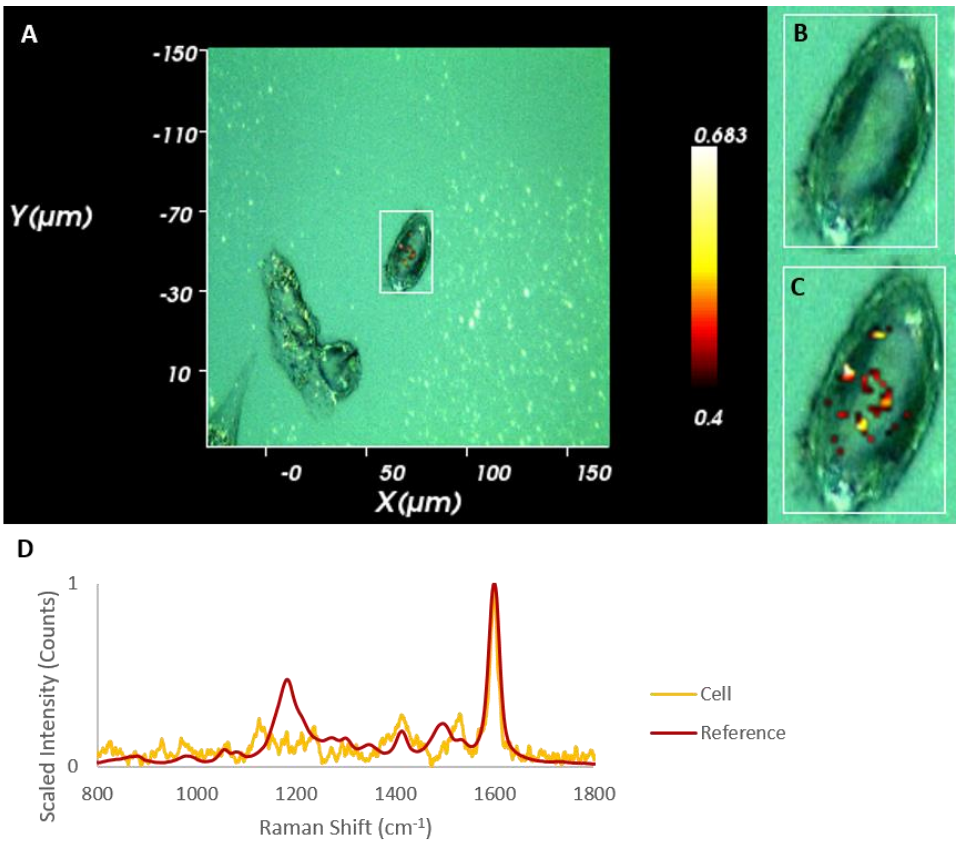

Figure 46 - Dye 3 functionalised gold nanoparticles (final nanotag concentration in cells 125 nM) incubated for 24 hours with the cells directly onto glass coverslips. (A) image of the cell with intensity scale bar. (B) white light image of the cell. (C) white light image of the cell with overlaid with a false colour intensity map calculated using DCLS. (D) representative cell spectrum from the mapped cell at a point of intensity signal overlaid with the reference spectrum for dye 1. The cell sample was analysed at 633 nm, 10% laser power (500 mW), 0.2-second acquisition time, centred at 1300 cm^{-1} and a step size of 1 µm.

The false colour images acquired for nanotags functionalised with dye 3 is similar to that acquired with dye 1; the areas of intensity are sparse and scattered throughout the cell. Some pixels are visible out with the boundary of the cell in the 12.5 nM sample (Figure 45 (C)), again attributed to incomplete washing of the slide. It is proposed that some of the nanotags may localise around the cell edges and immediately outside of the cell due to being 'stuck' on the cell surface as opposed to having been actually engulfed by the cell. This will be discussed in further detail following the spectral observations for all five nanotags. Again, the

most intense peak acquired is that at 1600 cm^{-1} corresponding to that of the dye 3 functionalised nanotag reference spectrum (shown in red).

The white light images, false colour images and spectra for cells containing dye 4 functionalised nanoparticles are shown in Figure 47, Figure 48 and Figure 49.

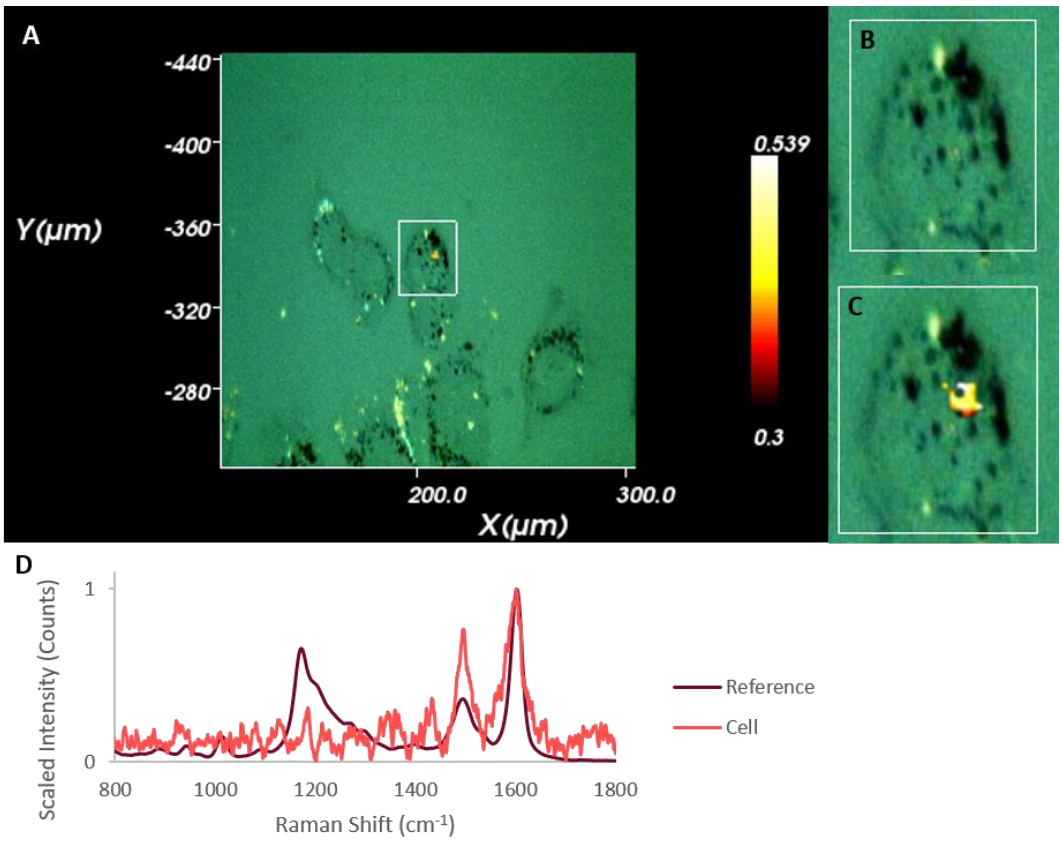

Figure 47 - Dye 4 functionalised gold nanoparticles (final nanotag concentration in cells 1.25 nM) incubated for 24 hours with the cells directly onto glass coverslips. (A) image of the cell with intensity scale bar. (B) white light image of the cell. (C) white light image of the cell with overlaid with a false colour intensity map calculated using DCLS. (D) representative cell spectrum from the mapped cell at a point of intensity signal overlaid with the reference spectrum for dye 1. The cell sample was analysed at 633 nm, 10% laser power (500 mW), 0.2-second acquisition time, centred at 1300 cm^{-1} and a step size of 1 µm.

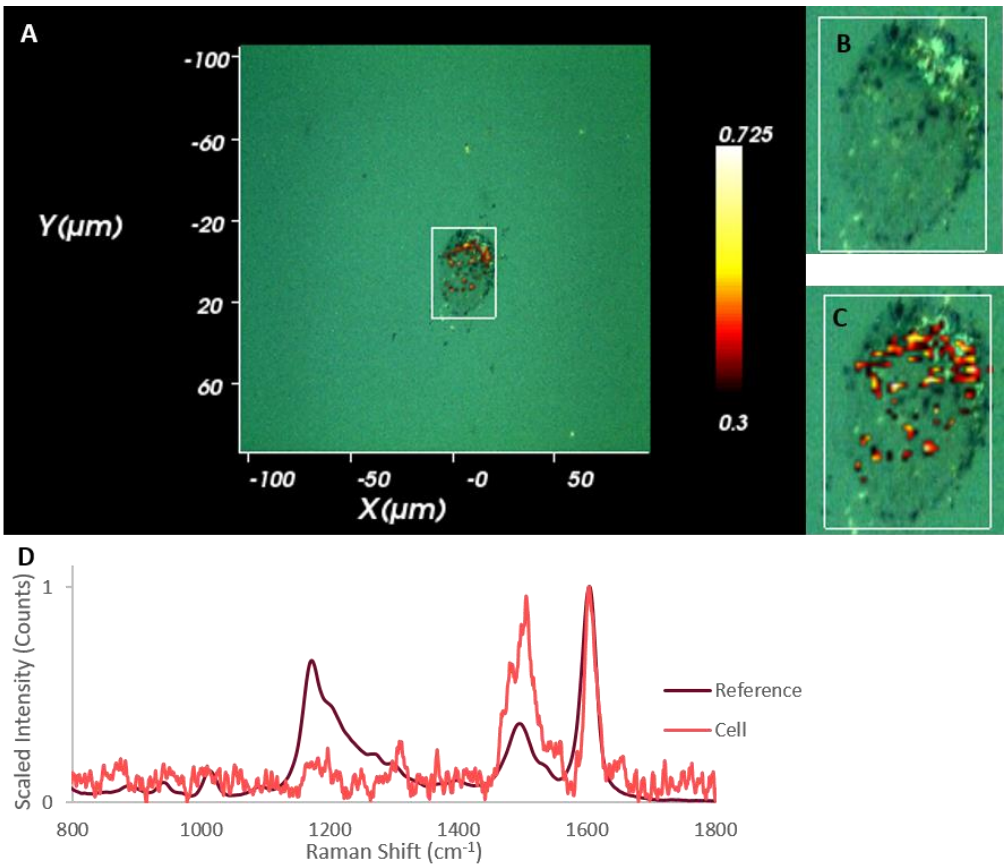

Figure 48 - Dye 4 functionalised gold nanoparticles (final nanotag concentration in cells 12.5 nM) incubated for 24 hours with the cells directly onto glass coverslips. (A) image of the cell with intensity scale bar. (B) white light image of the cell. (C) white light image of the cell with overlaid with a false colour intensity map calculated using DCLS. (D) representative cell spectrum from the mapped cell at a point of intensity signal overlaid with the reference spectrum for dye 1. The cell sample was analysed at 633 nm, 10% laser power (500 mW), 0.2-second acquisition time, centred at 1300 cm^{-1} and a step size of 1 µm.

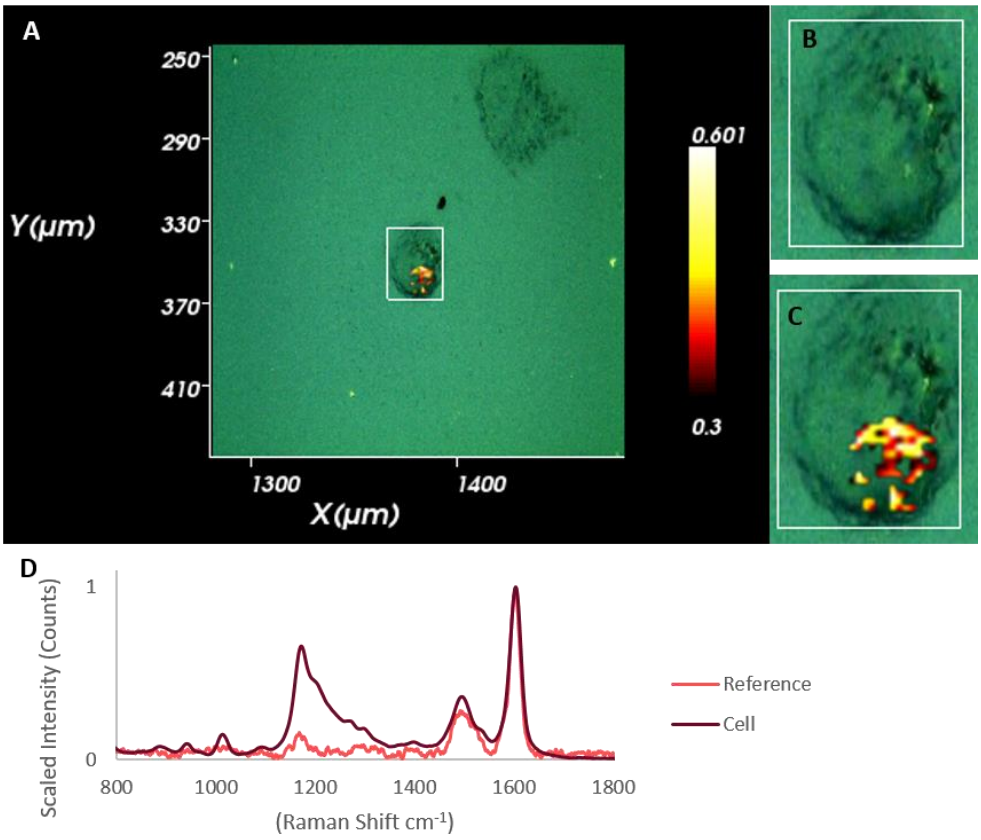

Figure 49 - Dye 4 functionalised gold nanoparticles (final nanotag concentration in cells 125 nM) incubated for 24 hours with the cells directly onto glass coverslips. (A) image of the cell with intensity scale bar. (B) white light image of the cell. (C) white light image of the cell with overlaid with a false colour intensity map calculated using DCLS. (D) representative cell spectrum from the mapped cell at a point of intensity signal overlaid with the reference spectrum for dye 1. The cell sample was analysed at 633 nm, 10% laser power (500 mW), 0.2-second acquisition time, centred at 1300 cm-1 and a step size of 1 µm.

The false colour images generated for dye 4 show a greater degree of localisation of nanotags within the cell at 1.25 nM and 125 nM (Figure 47and Figure 49 respectively) with the nanotags scattering throughout the cell at 12.5 nM final nanotag concentration (Figure 48). Here the nanotags appear to accumulate towards one section of the cell membrane, similar to that of dye 1 at 1.25 nM (Figure 38). 1.25 nM and 125 nM show the nanotags concentrating in on particular area of the cell providing greater evidence that these nanotags have been successfully up taken by the cells. This may also indicate that dye 4 is more

likely to localise within a specific component of the cell, however further studies would have to be conducted in order to confirm this. From all of the dyes studied in this section, dye 4 appears to give the 'closest match' to its reference spectrum (shown in purple) with two peaks visible at all three concentrations corresponding to peaks from the reference spectrum at 1500 cm^{-1} and 1605 cm^{-1}.

The white light images, false colour images and spectra for cells containing dye 6 functionalised nanoparticles are shown in Figure 50, Figure 51 and Figure 52.

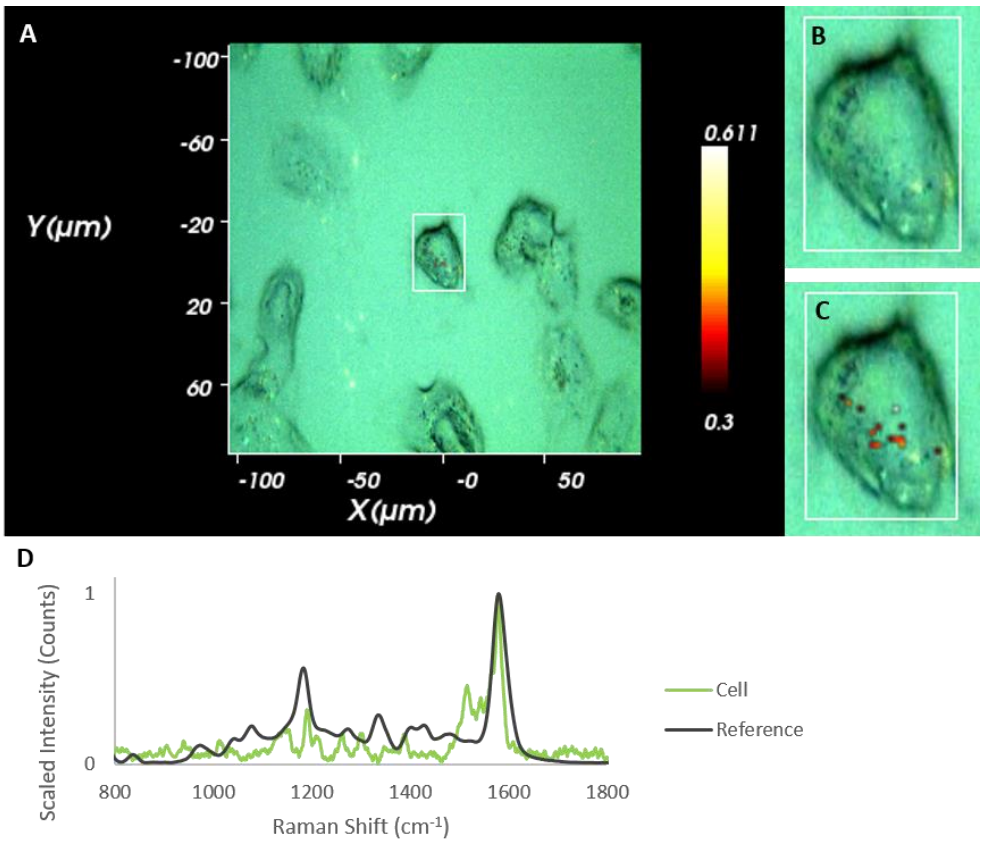

Figure 50 - Dye 6 functionalised gold nanoparticles (final nanotag concentration in cells 1.25 nM) incubated for 24 hours with the cells directly onto glass coverslips. (A) image of the cell with intensity scale bar. (B) white light image of the cell. (C) white light image of the cell with overlaid with a false colour intensity map calculated using DCLS. (D) representative cell spectrum from the mapped cell at a point of intensity signal overlaid with the reference spectrum for dye 1. The cell sample was analysed at 633 nm, 10% laser power (500 mW), 0.2-second acquisition time, centred at 1300 cm^{-1} and a step size of 1 µm.

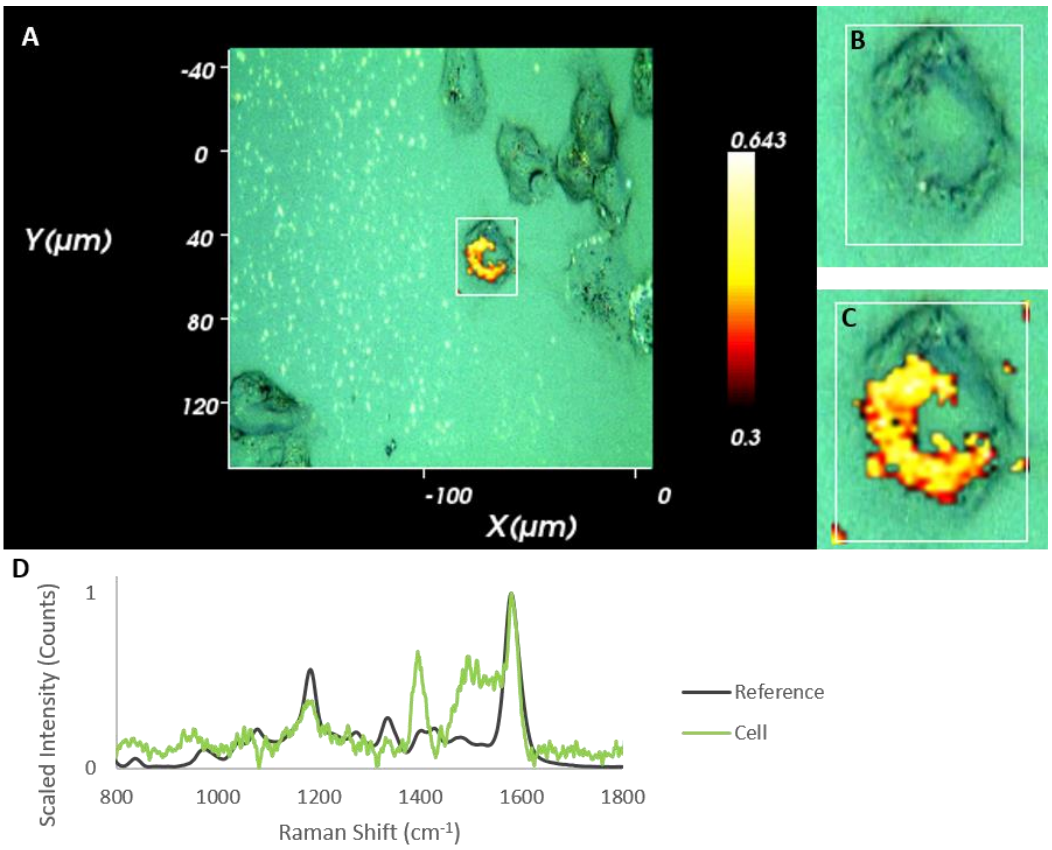

Figure 51 - Dye 6 functionalised gold nanoparticles (final nanotag concentration in cells 12.5 nM) incubated for 24 hours with the cells directly onto glass coverslips. (A) image of the cell with intensity scale bar. (B) white light image of the cell. (C) white light image of the cell with overlaid with a false colour intensity map calculated using DCLS. (D) representative cell spectrum from the mapped cell at a point of intensity signal overlaid with the reference spectrum for dye 1. The cell sample was analysed at 633 nm, 10% laser power (500 mW), 0.2-second acquisition time, centred at 1300 cm^{-1} and a step size of 1 µm.

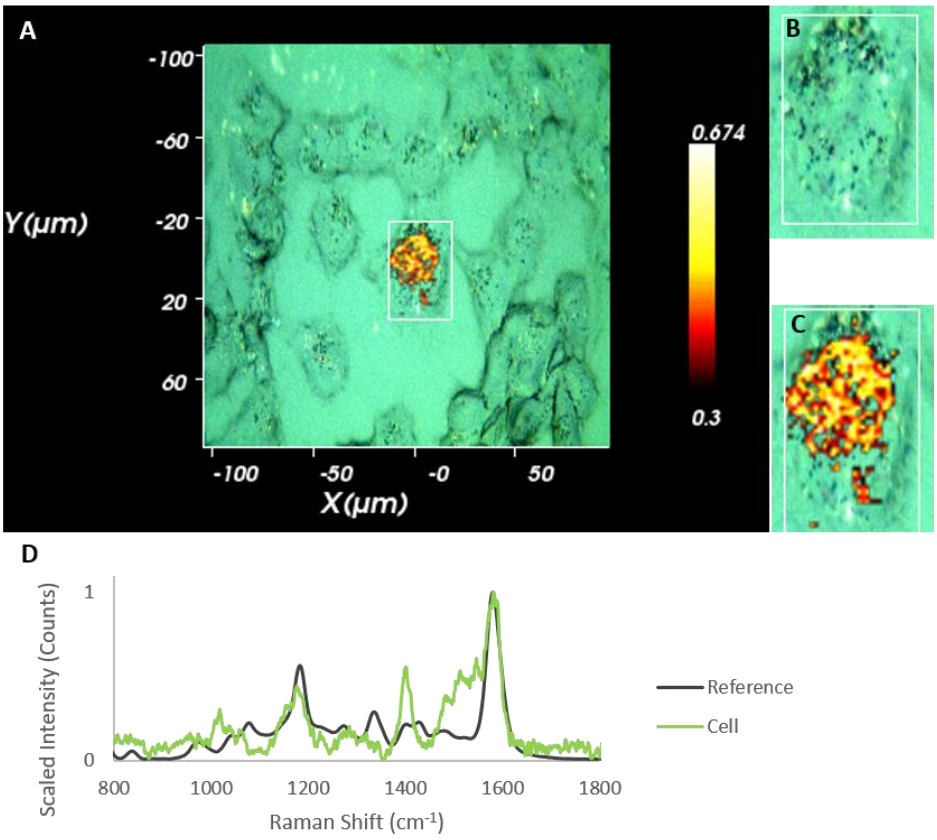

Figure 52 - Dye 6 functionalised gold nanoparticles (final nanotag concentration in cells 125 nM) incubated for 24 hours with the cells directly onto glass coverslips. (A) image of the cell with intensity scale bar. (B) white light image of the cell. (C) white light image of the cell with overlaid with a false colour intensity map calculated using DCLS. (D) representative cell spectrum from the mapped cell at a point of intensity signal overlaid with the reference spectrum for dye 1. The cell sample was analysed at 633 nm, 10% laser power (500 mW), 0.2-second acquisition time, centred at 1300 cm^{-1} and a step size of 1 µm.

The false colour images of the dye 6 based nanotags show the same scattered distribution, as mentioned with some other nanotags previously, at a tag concertation of 1.25 nM (Figure 50) but show much greater accumulation over all areas of the cell at 12.5 nM and 125 nM (Figure 51 and Figure 52 respectively). At 12.5 nM and 125 nM some areas of intensity are visible out with the cell membrane, again thought to be caused by incomplete wash steps. Spectrally, as with all other tags, the most prominent peak is visible at 1581 cm^{-1} corresponding

to that of the nanotag solution reference spectrum (shown in blue) with the 1185 cm^{-1} peak visible at concentrations of 12.5 nM and 125 nM.

A control image and spectrum of the PNT2 cells was also acquired. Figure 53 shows the white light image and spectra of a blank cell, containing no nanoparticles or nanotags.

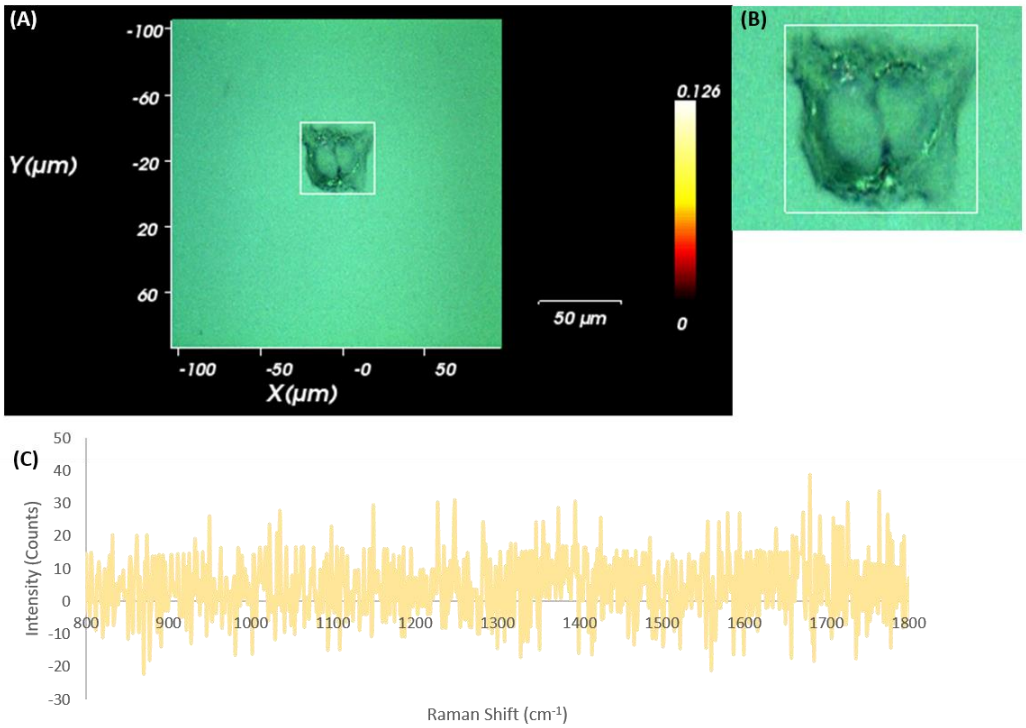

Figure 53 – Blank cells incubated for 24 hours with the cells directly onto glass coverslips. (A) image of the cell with intensity scale bar. (B) white light image of the cell. (c) representative cell spectrum from the mapped cell. The cell sample was analysed at 633 nm, 10% laser power (500 mW), 0.2-second acquisition time, centred at 1300 cm^{-1} and a step size of 1 µm.

Effective bio imaging of chalcogenopyrylium dye based nanotags was achieved at 633 nm laser excitation. Results observed for dyes 1 – 6 indicate uptake into cells and successful intracellular detectability using SERS with the majority of these signals originating from inside the cells with very little or no background signal present from outside the cell boundary. Cytotoxicity studies discovered that increasing the concentration of nanotags dosed to the cells does have a decreased

effect on the percentage of cell viability; this does appear to plateau in comparing the 125 nM and optimal nanotag concentration percentage viabilities, however a wider concentration range must be carried out in order to fully confirm this.

Additionally, it is important to address the minority of pixels visible out with the boundary of the cell membrane, present in some nanotag false colour images, not including dye 4. This is most likely due to incomplete removal of dead cells and other debris during the PBS and d.H_2O wash steps. It can also be argued that although washing the coverslip with PBS and d.H_2O will remove dead cells, it may be insufficient at removing nanoparticles and nanotags adhered to the glass coverslips out with the cells. The ease at which NPs adhere to glass is the reason why before and after NP synthesis, glassware is cleaned meticulously with aqua regia, ensuring any metal and NP residues are removed. This however would not be possible when working with glass cover slips during the cell fixation process as the cells would be killed and completely washed away. To combat this in the future, increasing the number of PBS and d.H_2O was steps would be beneficial to reduce non-specific nanotag localisation in extracellular space.

In addition to the appearance of pixels out with the cell membrane boundary, some images shown above display a high number of pixels and therefore nanotags around the boundary of the cell. There are two proposed explanations for this. Firstly, uptake of the nanotags occurs *via* channels in the cell membrane and the rate at which each nanotag and each concentration of nanotag is engulfed by the cell could vary. As only one incubation period (24 hours) was implemented, the incubation time regarding optimal nanotag uptake has not been investigated. Nanotags may still be involved in the uptake process of the cell, through the membrane, when fixed and imaged. Secondly, and most plausible of the two proposed explanations, is simply that the nanotags have adhered to the surface of the cell and around the cell boundary where there would be an edge. This could be confirmed using 3D cell mapping and TEM in order to visualise the localisation of nanotags in the cells at varying focal depths.

6.3.4. Alkyne Functionalised Chalcogenopyrylium Dyes

Towards the end of this research, the Detty research group, at University at Buffalo, synthesised and made available a series of chalcogenopyrylium dye molecules containing alkyne functionality, the use of which is advantageous for Raman signal acquisition in biological samples due to the presence of the alkyne peak in the biologically silent region of the spectrum (1800 – 2800 cm^{-1}). Although time constraints prevented the analysis of these alkyne dye nanotags in cells, these nanotags were analysed in solution in order to assess their ability to perform as NIR SERS nanotags, specifically regarding the position and visibility of the alkyne peak.

As a conclusive goal of this thesis was to analyse these nanotags in conjunction with red-shifted laser excitations, SERS measurements were carried out using a 1064 nm conventional handheld Raman spectrometer. Ideally SERS measurements of the alkyne peak would be obtained from a 1280 nm laser excitation source, however, the 1280 nm handheld Raman spectrometer was not employed in these studies as the alkyne peak was predicted to occur at approximately 2100 cm^{-1} and the spectral range of this spectrometer did not extend beyond 1800 cm^{-1}. Therefore, the 1064 nm handheld spectrometer was used in this study as this Raman spectrometer did possess a spectral range long enough to view the predicted ~ 2100 cm^{-1} alkyne peak. Additionally, from the depth of penetration studies conducted in chapter 5, significantly less spectral background is visible in tissue with the 1064 nm spectrometer than the 785 nm spectrometer, therefore it is of interest for both future cellular and tissue depth applications to assess the ability of the alkyne moiety to be detected *via* use of the 1064 nm handheld Raman spectrometer.

The structure of each of the alkyne-functionalised dyes analysed is shown in Figure 54.

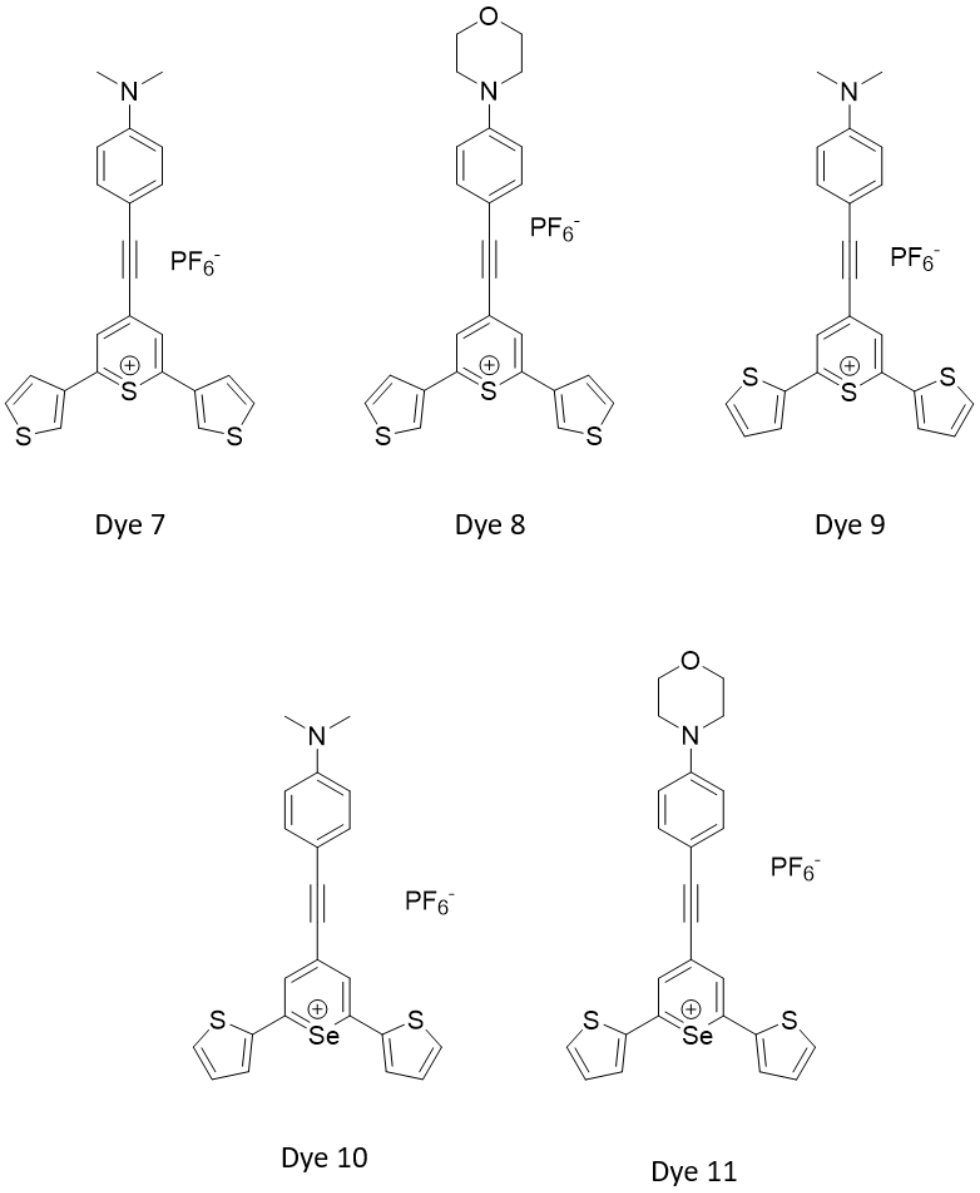

Figure 54 - Chemical structure of alkyne functionalised chalcogenopyrylium dyes 7 – 11.

6.3.4.1. 1064 nm SERS of CP Dyes containing Alkyne Moieties

Alkyne functionalised chalcogenopyrylium dyes were analysed in order to determine if signal from the alkyne peak was visible in the 'biologically silent' region of the spectrum. Due to time constraints, these were not analysed at in cells but analysed with a 1064 nm conventional handheld Raman spectrometer fitted with the point and shoot adaptor.

Dye stock solutions and nanotag samples were prepared in the same manner as all other dye stock and nanotags used throughout this thesis. SERS measurements were carried out using a Snowy Range (now Metrohm Raman) CBEX handheld Raman spectrometer 1064 nm, 30 mW laser power. A glass vial, 2 mL total volume, 15 mm vial diameter, 1 mm wall thickness was filled with each nanotag solution. The point and shoot adaptor was fitted to the spectrometer, placed in contact with the vial and the SERS measurement taken (As shown in Figure 30). Each nanotag had a final concentration of 500 nM, as this was the maximum concentration all other, similarly structured, CP based nanotags could reach before they crashed out of solution and no SERS response would be achieved. For future application, a full concentration study should be carried out in order to determine the optimal nanotag concentration.

The average baseline corrected spectrum for each nanotag is shown in Figure 55 and the absolute peak intensity of the alkyne peak in each spectrum is shown in Figure 56.

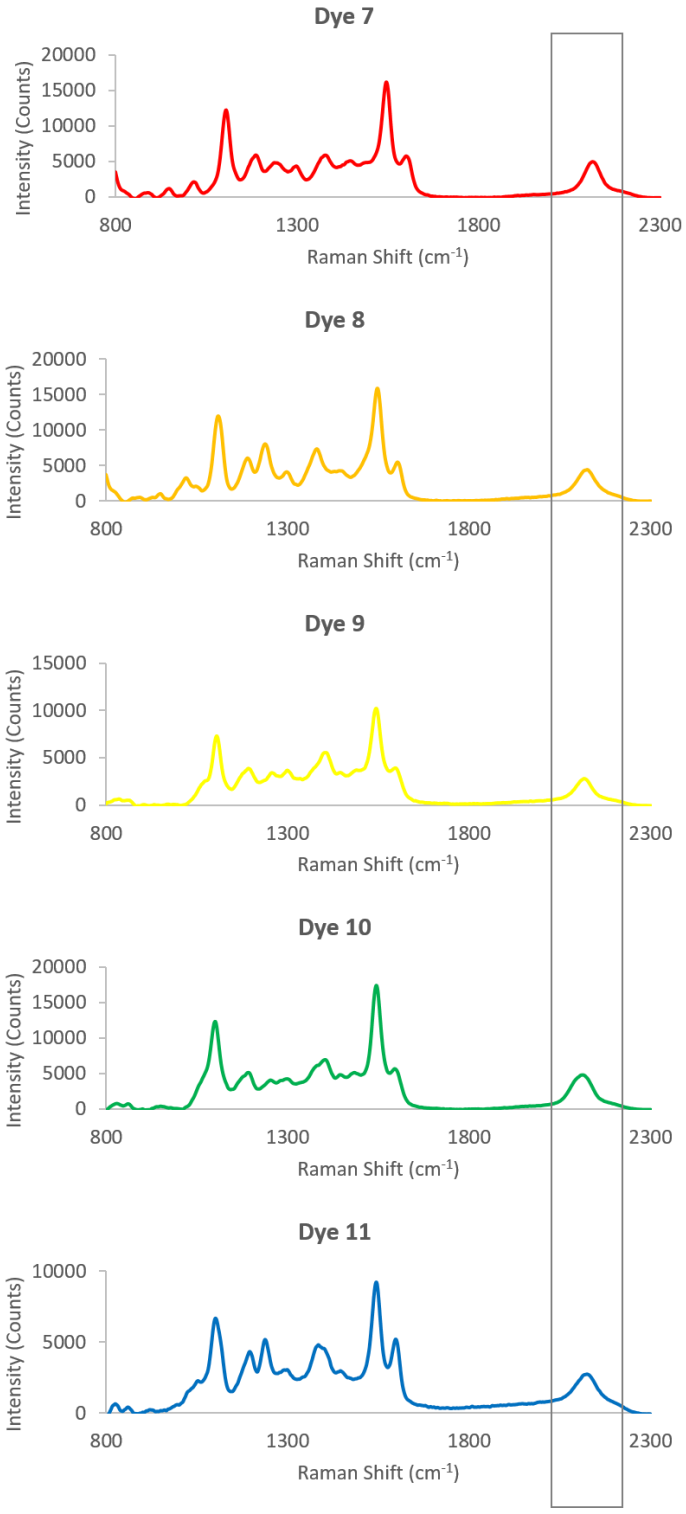

Figure 55 - Average baseline corrected SERS spectrum of dyes 7 – 11, at a concentration of 500 nM, exhibiting the characteristic alkyne peak at approximately 2100 cm^{-1}. Measured with a laser excitation wavelength of 1064 nm, laser power 30 mW and an integration time of 1 second. Each sample was prepared in triplicate with three replicate scans of each sample. A box highlights the peak of interest corresponding to the alkyne.

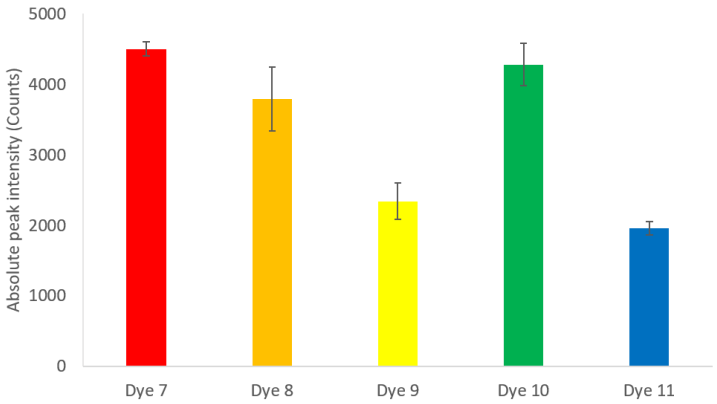

Figure 56 – Bar graph depicting the absolute peak intensity for the alkyne peak shown in each spectrum shown in Figure 55.

Dyes 7 – 11 analysed all show the characteristic alkyne peak at approximately 2100 cm^{-1}. The Raman shift of the alkyne peak of each dye is deduced and summarised in Table 7.

Table 7 – Summary of the Raman shift the alkyne peak in each dye spectrum (dye 7 – 11).

Dye	Alkyne peak Raman shift (cm^{-1})
7	2113
8	2125
9	2116
10	2112
11	2124

The Raman shift of dyes 8 and 11 are very similar to one another, as is the Raman shift of dyes 7, 9 and 10. This can be attributed to the similarities in structure: dyes 8 and 11 both contain morpholine functionality in addition to the alkyne moiety, whereas dyes 7, 9 and 10 possess dimethylamine functionality in addition

to the alkyne group. This could lead to the ability to multiplex using this specific alkyne peak, incredibly useful for the need to simultaneously detect multiple biomarkers in a, particularly in a non-destructive and sensitive manner, in media where this is often difficult due to spectral obstructions from the biological media itself.

As shown in Figure 56, these alkyne peaks are also relatively intense for spectra acquired in a solution via a point and shoot adaptor with no ability to specifically focus on the sample vial. This is advantageous for cellular applications where due to reasons regarding cytotoxicity, as little nanotag as possible could be used while still achieving respectable SERS intensity from the alkyne moieties. Once an optimal alkyne-CP nanotag concentration has been investigated, these alkyne functionalised CP dyes show promise as a useful tool for future intracellular imaging applications.

6.4. Chapter Conclusions and Future Work

Effective bio imaging at 633 nm excitation using chalcogenopyrylium based nanotags, designed and employed in chapters 3, 4 and 5 of this thesis, was accomplished. Initial cytotoxicity results, achieved by use of Trypan Blue as a live dead stain, discovered that these nanotags were relatively biocompatible with an approximate 40 – 60 % cell viability rate. It was also discovered that the percentage viability of these nanotags in cells at a concentration of 125 nM was similar to the percentage viability of that of the optimal nanotag concentration, deduced in chapters 3 and 4. With these optimal concentrations being approximately 3 and 5 times greater than the 125 nM concentration, this indicated that the percentage of cells compromised would plateau over this range. A more in depth concentration study over the concentration range 125 - 500 nM should be carried out in order to ascertain if this is in fact the case. It may also be beneficial, for future cellular applications, to extend this concentration range allowing determination of the concentration at which no

cells survive; the concentration at which these nanotags have a complete toxic effect.

As a future application of these nanotags would be application in cancerous tumour detection, it would be interesting to monitor the toxic effects of these nanotags on cancerous cells and in cancerous tumours as this 40 – 60 % cell viability rate on a healthy cell population may actually be of potential use if approximately half of a cancerous cell population is compromised. This could be complimented by functionalising these nanotags with specific biomarkers relating to the type of biological abnormality, cancer or tumour being analysed in order to determine if these nanotags will localise in the malignant cells and tissues and not in healthy media, allowing effective tumour imaging to be carried out.

As this thesis employs the use of a 1280 nm laser excitation in conjunction with these red-shifted nanotags, it would be of extreme benefit to incorporate one or both of the 1280 nm Raman spectrometers into an experimental set up allowing these nanotags to be imaged. As it stands, white light images of the cells could not be obtained with these Raman spectrometers in a point-and-shoot set up, however manually imaging across the cell or group of cells allowing production of a 2D heat map of intracellular nanotag intensity could in theory be possible. Further work should be carried out to investigate the instrumental capabilities in the arrangement of the 1280 nm spectrometer for mapping across a cellular sample containing these nanotags.

It was evident that most nanotags did localise inside the cells, some showing 'grouping' confining to a small area of the cell indicative that these nanotags were successfully engulfed by the cells. However, some cell images obtained appeared to show nanotags scattered throughout the cell, gathering around the cell membrane and localising out with the membrane boundary of the cell in the extracellular space. 2D cell mapping alone is not enough to confidently confirm these nanotags are in fact localised inside the cells and in some samples shown, not simply adhered to the cell edge and cell surface. 2D mapping was elected over 3D mapping for speed of analysis, however, future SERS imaging should be

carried out as a 3D map in order to view the depth profile of the cell and thus determine the degree of nanotag localisation within the cell. Ideally, TEM analysis should also be employed in order to aid conformation of successful cell uptake. Obtaining TEM images focused both on the surface of the cell and focused at a depth within the cell will allow visualisation of whether or not the nanotags are inside the cells or merely adhered to the surface. TEM images would also show the distribution of nanotags within the cell, complimenting the false colour images acquired *via* SERS imaging. An additional thought towards the localisation of these nanotags around the cell membrane was that the rate at which the cells would uptake the nanotags was unknown; therefore, some nanotags may be present in the cell membrane as the image was taken during the uptake process. A study comparing a range of different nanotag-cell incubation times should be carried out in order to determine the incubation time resulting in optimal SERS response.

Cellular imaging studies were conducted with the optimal on-nanoparticle dye concentration, reported in chapters 3 and 4, which assumed monolayer coverage and therefore a slight degree of nanoparticle stability. However, this alone is not enough and studies should be carried out investigating appropriate nanotag stabilisation layers suited to *in vitro* applications.

As a proof of concept, cell-imaging studies were carried out on fixed cells. There is debate surrounding the accuracy of representation when imaging fixed cells. The condition of a fixed cell varies significantly to that of a live cell and it is known that the cell membrane lipid content is considerably affected during the fixation process. The wash and drying steps of the coverslip also present the opportunity for ineffective washing and often nanotags can adhere to the glass and surface of the fixed cell. Therefore, it would be beneficial to carry out these imaging and detectability studies on live cells.

As mentioned in 6.3.4.1, towards the end of this research project, the Detty research group synthesised and made available a series of alkyne functionalised chalcogenopyrylium dye molecules shown in Figure 54. In order to model the ability of these alkyne-CP dyes to provide a SERS response at NIR excitation

wavelengths, these dyes were functionalised onto AuNPs and the SERS response in solution measured. They provide a clear peak, corresponding to the alkyne stretch within the molecule, at approximately 2100 cm^{-1}. The Raman shift of this alkyne varies slightly depending on the other functionality present within the CP dye molecule and as a result, the difference in alkyne peak shift could allow multiplexing of these alkyne-CP dye molecules in future studies. These alkyne-CP nanotags should be investigated in cell and an optimal nanotag concentration should be obtained and the cellular alkyne response and localisation studied.

7. Thesis Conclusions

Large gold nanoparticles functionalised with a novel emerging class of chalcogenopyrylium dye molecules have shown to exhibit an intense SERS response at 1280, 1064 and 785 nm laser excitations providing effective NIR active nanotags. These nanotags have been exploited in multiple SERS applications discussed throughout this thesis.

Five CP dye molecules were designed for a study in order to investigate the relationship between the CP dye binding orientation, determined by SFG-VS, and the SERS response in conjunction with a prototype 1280 nm Raman spectrometer was investigated. It was discovered that optimal SERS response was achieved when the CP dye was orientated on the surface in the most perpendicular arrangement possible. Dye 4 was predicted to orientate on the surface at an almost flat angle of 10° - 30°, which at the lowest concentration of 50 nM it was believed to do so. However, upon increasing the dye concentration, there was a significant change in the relative peak intensities of the vibrations correspond to the main body of the molecule thus leading to the belief that surface packing of the CP dye molecule, on the NP surface, caused this dye to assume a more 'upright' position. It is believed that the bands that appear most intense in these SERS spectra (~ 1490 cm^{-1} and ~1590 cm^{-1}) arise due to displacements along the core of the CP dye molecule. This π-system provides a readily polarisable electron cloud along the core of the dye molecule, therefore when the core of the dye molecule is as perpendicular as possible to the metal surface, the greatest surface enhancement is found to occur.

Chapter 4 of this thesis investigated the ability to design a nanotag capable of selectively producing a SERS response at 1280 nm laser excitation while remaining transparent upon interrogation with a 785 nm laser source. A nanotag, already known to perform well in conjunction with a 1280 nm laser source was created. To this colloidal solution a new CP based dye 'blocking molecule' was added. Addition of this BM to the nanotag solution caused either complete elimination of the nanotag at 785 nm excitation at concentrations greater than

5 mM by oversaturation of the detector, or caused masking of the nanotag signal at concentrations of 1425 nM and above. The nanotag SERS signal acquired at 1280 nm remained visible with very little variation regardless of the approach selected.

In biomedical imaging, there is a significant requirement to probe through biological media by non-invasive means. The majority of biological Raman imaging of tissues, cancerous tumours and other malignancies is conducted by use of a 785 nm laser source. However, moving further into the red-shifted laser excitations available, probing deeper through tissue samples should be possible due to the fact the majority of components in the tissue samples have reduced light absorption and scattering backgrounds. Specifically, at wavelengths greater than 1100 nm, water is the most strongly absorbing component of biological samples. Therefore, there was requirement to investigate the depth of penetration abilities of conventional portable handheld Raman spectrometers over three NIR excitation wavelengths: 785, 1064 and 1280 nm. The 1064 nm Raman spectrometer was found to provide the greatest depth of nanotag detection through the pork tissue samples analysed. The 1064 nm Raman spectrometer was able to probe 4 mm deeper in comparison to the 785 nm Raman spectrometer when a resonant CP dye was employed as the reporter molecule. No depth of penetration was achieved in the pork tissue models in conjunction with the 1280 nm spectrometer, only spectral noise was observed. It is thought components of the tissue may absorb the laser light and / or scattered light from the nanotag preventing it from reaching the detector. As it is known water is highly absorbing at this wavelength and that water is in fact added to the pork during the manufacturing process, this was suggested as a reason why no SERS response, at depth was achieved. To confirm the tissue prevented signal acquisition and not the pork tissue, clear plastic was employed as the barrier. Here, the 1280 nm spectrometer was able to detect the nanotags up to a depth of 8 mm plastic.

Reports in literature have very recently emerged employing these CP based dyes in biological applications including localisation within and detection of cancerous

tumours, cell-based cancer models and in *ex vivo* multiplexing platforms. Up until the research reported in chapter 6 of this thesis, the toxicity of such CP based nanotags had not been studied and was unknown. Five CP dye based nanotags were applied to healthy prostate cell populations and their cytotoxicity evaluated using a Trypan Blue stain. Cytotoxicity results were as expected, the higher the nanotag concentration within the cell, the lower the % of cell viability. However, it was observed that the % viability of the cells appeared to remain consistent over the concentration range 125 nM – the optimal concentration range, indicating the toxicity of CP based nanotags plateaus over this range in which they are not overly toxic. In addition to cytotoxicity, it was important to assess whether or not these nanotags would be detectable in cells at these concentrations. The cells were incubated with the nanotags and imaged using a Raman microscope. Work carried out in chapter 6 highlights the successful ability of these nanotags to be localised and detected within fixed cell populations using SERS, mainly by tracking of the most intense peak in the spectrum (~ 1590 cm^{-1}) corresponding to the main body of the CP dye molecules. Towards the end of this research, collaborators at the University at Buffalo, NY, USA made available a series of alkyne containing CP dyes. Although time constraints prevented analysis of these alkyne-CP nanotags in cells and at depth through tissue, they were analysed in solution using a handheld 1064 nm Raman spectrometer in order to assess their ability to provide the characteristic alkyne peak in the 'biologically silent' region of the spectrum upon red shifted excitation. These alkyne-CP nanotags provided a relatively intense peak at approximately 2100 cm^{-1} in the Raman spectrum indicating their suitability to be applied in cells and tissue depth models for interference free monitoring and detection. Additionally, variations in the Raman shift of this alkyne peak, corresponding to the variations in structure of these molecules, makes these alkyne-CP dyes excellent candidates for multiplexed biological detection applications.

8. Experimental

8.1. Materials

All chalcogenopyrylium dye molecules were synthesised and provided by Professor Michael Detty, Miss Lauren Rosch and Mr. Konstantinos Plakas at the University at Buffalo, NY, USA.

Chemicals used for cell viability experiments: 1640 Roswell Park Memorial Institute medium (RPMI), heat-inactivated fetal bovine serum (FBS), penicillin/streptomycin, fungizone and Trypan Blue were purchased from ThermoFisher Scientific.

All other chemicals were purchased from Sigma Aldrich and used without further purification, unless stated otherwise.

Ultrapure deionized water was obtained from an in-house Merck Milli-Q filtration unit.

The plastic barriers used in chapter 5 for depth of penetration experiments was purchased from a local art store by a previous PhD student. Pork loin meat also used in this chapter for depth of penetration experiments was obtained from a local butcher.

8.2. Instrumentation

8.2.1. Extinction Spectroscopy

All UV-Vis measurements were carried out on an Agilent Cary 60 UV-Visible spectrometer in conjunction with Cary WinUV software over the 350 – 1100 nm wavelength range. Approximately 500 μL of sample was run in a disposable poly(methyl methacrylate) (PMMA), with a total volume of 1.5 mL and a path length of 1 cm.

8.2.2. Dynamic Light Scattering (DLS) and Zeta Potential

All size and zeta potential measurements were carried out using a Malvern Zetasizer Nano ZS in conjunction with Zetasizer μV and APS software, version 6.20. Approximately 2 cm of sample was run in a disposable PMMA cuvette with a total volume of 3 mL and a path length of 1 cm. A standard Malvern dip cell was inserted into the cuvette in order to measure the zeta potential of each sample. This dip cell was carefully cleaned *via* sonication in addition to multiple water and isopropyl alcohol (IPA) rinses to ensure there was no contamination sample to sample.

8.2.3. Scanning Electron Microscopy (SEM) Measurements

All SEM measurements were carried out using a Hitachi S-3000N variable pressure SEM with an acceleration voltage of 30 kV. Initially, nanotag samples were spotted onto silica wafers and left to dry, these wafers were then placed onto the SEM pin mount and inserted into the instrument.

8.2.4. Surface Enhanced Raman Scattering (SERS) Measurements

8.2.4.1. SnRI 1280 nm Measurements

Solution spectra were collected using a portable Snowy Range (now Metrohm Raman) Sierra series Raman spectrometer with a 1280 nm excitation wavelength (not commercially available) and a laser power of 100 mW. All spectra were acquired with a 3 second integration time. Each sample was prepared in triplicate with three replicate scans of each sample measured.

8.2.4.2. CBEx 785 nm Measurements

Solution spectra were collected using: a handheld Snowy Range (now Metrohm Raman) CBEx spectrometer with a 785 nm excitation wavelength and a laser power of 43 mW.

8.2.4.3. CBEx 1064 nm Measurements

Solution spectra were collected using a handheld Snowy Range CBEx spectrometer (now Metrohm Raman) with a 1064 nm excitation wavelength and a laser power of 30 mW.

8.2.4.4. 785, 1064 and 1280 nm SERS Measurements Involving Plastic Barriers

Large transparent polyethylene terephthalate (PET) plastic sheets, of 1 mm thickness, were purchased from a local art store and cut up into smaller rectangular pieces (10.5 x 3 cm) by a previous PhD student. These smaller sheets of plastic were clamped together in order to obtain the desired thickness, typically beginning with one sheet, therefore a 1 mm thickness, increasing by one sheet each time until SERS signal from the nanotag was no longer visible. They were then placed in front of the sample vial (15 mm diameter, 1 mm wall thickness) and brought into contact with the point and shoot adaptor of the hand held Raman spectrometer ensuring no space, and therefore air, was between the sample vial, plastic and instrument. The SERS measurements were taken with a 3 second integration time and the raster feature of the spectrometer switched on.

8.2.4.5. 785, 1064 and 1280 nm SERS Measurements Involving Tissue Barriers

Pork loin meat was purchased from a local butcher with each slice measuring 2 mm in thickness (the lowest thickness of which the butcher's machine was capable of producing). Pork loin was selected, as it is generally the less "fatty" of the cuts and was the closest mimic to a human tissue model. Each slice was cut into 3 x 3 cm pieces and placed in front of the vial in the same manner mentioned

in section 5.3.3.1, for the plastic barriers. The SERS measurements were taken with a 3 second integration time and the raster feature of the spectrometer switched on.

8.3. Experimental

8.3.1. Synthesis of Gold Nanoparticles

AuNPs, used in all chapters of this thesis, were synthesised by heating gold(III) chloride hydrate (500 mL, 103 μM) until boiling. This was then reduced by the addition of sodium citrate (7.5 mL, 1.07 μM) and left to boil for 15 minutes, during which, a colour change of pale yellow to a dark orange/red was observed.

8.3.2. Chalcogenopyrylium Dye Stock Solution Preparation

All chalcogenopyrylium dyes used throughout this thesis were prepared by dissolving the solid dye, provided by University at Buffalo, in anhydrous N,N-Dimethylformamide (99.8%) to produce a 1 mM stock solution. Subsequent dilutions were then carried out using a 50:50 DMF/h.H_2O solution.

8.3.3. Nanotag Preparation

Chalcogenopyrylium dye solutions were added to the 'as prepared' nanoparticle solution yielding the final concentration required. This was achieved by serial dilution. These nanotags were purified by centrifugation (2500 rpm, 15 minutes) and re-suspended in the same volume of d.H_2O as supernatant was removed. The total final volume of each nanotag was 500 μL.

8.3.4. Cell Sample Preparations

8.3.4.1. Cell Line Selection

Healthy human prostate cells (PNT2) were used in this study.

8.3.4.2. Cell Culture and Nanotag Incubation

Initial cell culture was carried out by Corinna Wetherill. PNT2 human prostate cells were cultured in 1640 Roswell Park Memorial Institute medium (RPMI) with the addition of 10% heat-inactivated fetal bovine serum (FBS), 1% penicillin/streptomycin and 1% fungizone. Cells were incubated in a humidified incubator at 37 °C and 5% CO_2. Cells were grown in a T75 flask, trypsinised and reuspended in medium. The concentration of cells varied depending on the batch used. Cell concentrations are denoted in appendix X. Cells were pipetted into sterile polystyrene cell culture plates (9.5 cm^2 growth area) at a concentration of $0.5x10^{-6}$ cells per well and incubated overnight. The following day (24 hours) nanotags were added to cells at concentrations 1.25 nM, 12.5 nM, 125 nM and the optimal concentration for each nanotag. These cells were then incubated for a further 24 hours. Following nanotag addition and 24 hour incubation period, cells were trypsinised, removed from the plates and counted using a Trypan Blue stain.

8.3.4.3. Cell Culture and Nanotag Incubation – Preparation for Imaging

Initial cell culture was carried out by Corinna Wetherill. PNT2 human prostate cells were cultured in 1640 Rosewell Park Memorial Institute medium (RPMI) treated with the addition of 10% heat-inactiveted fetal bovine serum (FBS), 1% penicillin/streptomycin and 1% fungizone. Cells were incubated in a humidified incubator at 37 °C and 5% CO_2. Cells were grown in a T75 flask, trypsinised and reuspended in medium. The concentration of cells varied depending on the batch used. Cell concentrations are denoted in appendix X. Cells were pipetted into sterile polystyrene cell culture plates (9.5 cm^2 growth area), containing a glass cover slip, at a concentration of $0.5x10^{-6}$ cells per well and incubated overnight. The following day (24 hours) nanotags were added to cells at concentrations 1.25 nM, 12.5 nM, 125 nM and the optimal concentration for each nanotag. These cells were then incubated for a further 24 hours. Following nanotag addition and 24 hour incubation period, cells were fixed with paraformaldehyde (PFA), left to air dry and stored in their initial well plates.

8.3.4.4. Cellular SERS Imaging

Images were collected using a Renishaw inVia Raman spectrometer with a 633 nm excitation wavelength (500 mW, 10% laser power), 1800 mm^{-1} grating, x50 objective (NA = 0.75), an integration time of 0.2 seconds and a spectral range of 715 – 1829 cm^{-1} and a step size of 1 μm. Again, it is noted this work would have been carried out with the 785 nm laser excitation had the 785 nm laser not been inoperative. A silica standard was used to optimise the spectrometer signal intensity and to provide an intensity reference for data normalisation by using the peak at 520 cm^{-1}.

8.3.4.5. Data Processing of Cell Images and Spectra

Data was processed using Renishaw WiRE software version 4.4. The spectra was baseline corrected and any cosmic rays were removed. The spectra was then plotted and saved in .spc .txt and the WiRE file format, for future processing. White light cell images were taken by the spectrometer camera were not processed any further. Heat map overlays were generated using DCLS. These images were used without further image processing.

9. References

1 R. Feynman, in *Feynman and Computation*, CRC Press, 2018, pp. 63–76.

2 O. V. Salata, *Journal of Nanobiotechnology*, 2004, **6**, 1–6.

3 G. Schmid, *Metal Nanoclusters in Catalysis and Materials Science*, 2008.

4 X. Huang and M. A. El-Sayed, *Journal of Advanced Research*, 2010, 1, 13–28.

5 Jü. Altmann, *Security Dialogue*, 2004, **35**, 61–79.

6 N. L. Rosi and C. A. Mirkin, *Chemical Reviews*, 2005, **105**, 1547–1562.

7 J. Turkevich, P. C. Stevenson and J. Hillier, *Discussions of the Faraday Society*, 1951, **11**, 55.

8 P. C. Lee and D. Meisel, *The Journal of Physical Chemistry*, 1982, **86**, 3391–3395.

9 D. de Caro, H. Wally, C. Amines and B. Chaudret, *Journal of the Chemical Society, Chemical Communications*, 1994, 1891.

10 H. Ping, K. Lu, Y. Jun, Y. Fan, W. Kuaishe, D. Jinjing, Y. Zhanlin, C. Weicheng and L. Dongxin, *Rare Metal Materials and Engineering*, 2016, **45**, 3112–3114.

11 K. S. Rao, K. El-Hami, T. Kodaki, K. Matsushige and K. Makino, *Journal of Colloid and Interface Science*, 2005, **289**, 125–131.

12 I. Freestone, N. Meeks, M. Sax and C. Higgitt, *Gold Bulletin*, 2008, **40**, 270–277.

13 L. Kool, A. Bunschoten, A. H. Velders and V. Saggiomo, *Beilstein Journal of Nanotechnology*, 2019, **10**, 442–447.

14 D. A. Giljohann, D. S. Seferos, W. L. Daniel, M. D. Massich, P. C. Patel and C. A. Mirkin, *Angewandte Chemie International Edition*, 2010, **49**, 3280–3294.

15 Z. Chen, H. Meng, G. Xing, C. Chen, Y. Zhao, G. Jia, T. Wang, H. Yuan, C. Ye, F.

Zhao, Z. Chai, C. Zhu, X. Fang, B. Ma and L. Wan, *Toxicology Letters*, 2006, **163**, 109–120.

16 X. Chen, Q. W. Li and X. M. Wang, in *Precious Metals for Biomedical Applications*, Woodhead Publishing, 2014, pp. 163–176.

17 A. M. Schwartzberg, T. Y. Olson, C. E. Talley and J. Z. Zhang, *Journal of Physical Chemistry B*, 2006, **110**, 19935–19944.

18 B. Nikoobakht and M. A. El-Sayed, *Chemistry of Materials*, 2003, **15**, 1957–1962.

19 H. J. Han, T. Yu and S. H. Im, *Journal of Crystal Growth*, 2017, **469**, 48–53.

20 S. E. Skrabalak, J. Chen, Y. Sun, X. Lu, L. Au, C. M. Cobley and Y. Xia, *Accounts of Chemical Research*, 2008, **41**, 1587–1595.

21 C. A. J. Lin, T. Y. Yang, C. H. Lee, S. H. Huang, R. A. Sperling, M. Zanella, J. K. Li, J. L. Shen, H. H. Wang, H. I. Yeh, W. J. Parak and W. H. Chang, *ACS Nano*, 2009, **3**, 395–401.

22 L. Fabris, M. Bhamidipati, K. Dardir, T. V. Tsoulos and S. Atta, in *Colloidal Nanoparticles for Biomedical Applications XIII*, eds. X.-J. Liang, W. J. Parak and M. Osiński, SPIE, 2018, vol. 10507, p. 5.

23 G. Frens, *Nature Physical Science*, 1973, **241**, 20–22.

24 H. Dozol, G. Mériguet, B. Ancian, V. Cabuil, H. Xu, D. Wang and A. Abou-Hassan, *Journal of Physical Chemistry C*, 2013, **117**, 20958–20966.

25 N. Shirtcliffe, U. Nickel and S. Schneider, *Journal of Colloid and Interface Science*, 1999, **211**, 122–129.

26 M. Faraday, *Philosophical Transactions of the Royal Society of London*, 1857, **147**, 145–181.

27 K. R. Brown, D. G. Walter and M. J. Natan, *Chemistry of Materials*, 2000, **12**, 306–313.

28 S. D. Perrault and W. C. W. Chan, *Journal of the American Chemical Society*,

2009, **131**, 17042–17043.

29 S. T. Gentry, S. J. Fredericks and R. Krchnavek, *Langmuir*, 2009, **25**, 2613–2621.

30 N. G. Bastús, J. Comenge and V. Puntes, *Langmuir : the ACS journal of surfaces and colloids*, 2011, **27**, 11098–105.

31 A. Gautam and F. C. J. M. Van Veggel, *Journal of Materials Chemistry B*, 2013, **1**, 5186–5200.

32 I. P. Lau, H. Chen, J. Wang, H. C. Ong, K. C. F. Leung, H. P. Ho and S. K. Kong, *Nanotoxicology*, 2012, **6**, 847–856.

33 C. Grabinski, N. Schaeublin, A. Wijaya, H. D'Couto, S. H. Baxamusa, K. Hamad-Schifferli and S. M. Hussain, *ACS Nano*, 2011, **5**, 2870–2879.

34 A. P. Leonov, J. Zheng, J. D. Clogston, S. T. Stern, A. K. Patri and A. Wei, *ACS Nano*, 2008, **2**, 2481–2488.

35 J. Manson, D. Kumar, B. J. Meenan and D. Dixon, *Gold Bulletin*, 2011, **44**, 99–105.

36 S. Rucareanu, M. MacCarini, J. L. Shepherd and R. B. Lennox, *Journal of Materials Chemistry*, 2008, **18**, 5830–5834.

37 F. Zhang, E. Lees, F. Amin, P. Rivera-Gil, F. Yang, P. Mulvaney and W. J. Parak, *Small*, 2011, 7, 3113–3127.

38 A. Kumari, S. K. Yadav and S. C. Yadav, *Colloids and surfaces. B, Biointerfaces*, 2010, **75**, 1–18.

39 H. Kearns, N. C. Shand, K. Faulds and D. Graham, *Chem. Commun.*, 2015, **51**, 8138–8141.

40 K. A. Willets and R. P. Van Duyne, *Annual Review of Physical Chemistry*, 2006, **58**, 267–297.

41 J. Homola, S. S. Yee and G. Gauglitz, *Sensors and Actuators B: Chemical*, 1999, **54**, 3–15.

42 G. Mie, *Annalen der Physik*, 1908, **25**, 377–452.

43 P. Newman, *Contributions to the optics of turbid media, particularly of colloidal metal solutions*, Albuquerque, New Mexico, 1908, vol. 25.

44 S. Eustis and M. A. El-Sayed, *Chem. Soc. Rev.*, 2006, **35**, 209–217.

45 V. Amendola, O. M. Bakr and F. Stellacci, *Plasmonics*, 2010, **5**, 85–97.

46 M. Hu, J. Chen, Z.-Y. Li, L. Au, G. V. Hartland, X. Li, M. Marquez and Y. Xia, *Chemical Society Reviews*, 2006, **35**, 1084.

47 Gold Nanoparticles: Optical Properties – nanoComposix, https://nanocomposix.com/pages/gold-nanoparticles-optical-properties#target, (accessed 21 May 2019).

48 nanoComposix, Silver Nanoparticles: Optical Properties – nanoComposix, https://nanocomposix.com/pages/silver-nanoparticles-optical-properties#target, (accessed 21 May 2019).

49 S. Atta, M. Beetz and L. Fabris, *Nanoscale*, 2019, **11**, 2946–2958.

50 S. Trigari, A. Rindi, G. Margheri, S. Sottini, G. Dellepiane and E. Giorgetti, *Journal of Materials Chemistry*, 2011, **21**, 6531.

51 S. L. Smitha, K. G. Gopchandran, N. Smijesh and R. Philip, *Progress in Natural Science: Materials International*, 2013, **23**, 36–43.

52 W. P. Hall, S. N. Ngatia and R. P. Van Duyne, *Journal of Physical Chemistry C*, 2011, **115**, 1410–1414.

53 H. Aldewachi, T. Chalati, M. N. Woodroofe, N. Bricklebank, B. Sharrack and P. Gardiner, *Nanoscale*, 2018, 10, 18–33.

54 C. A. Mirkin, R. L. Letsinger, R. C. Mucic and J. J. Storhoff, *Nature*, 1996, **382**, 607–609.

55 C. L. Schofield, R. A. Field and D. A. Russell, *Analytical Chemistry*, 2007, **79**, 1356–1361.

56 H. P. Liang, L. J. Wan, C. L. Bai and L. Jiang, *Journal of Physical Chemistry B*, 2005, **109**, 7795–7800.

57 N. R. Jana, L. Gearheart and C. J. Murphy, *Journal of Physical Chemistry B*, 2001, 105, 4065–4067.

58 K. S. Lee and M. A. El-Sayed, *Journal of Physical Chemistry B*, 2005, **109**, 20331–20338.

59 F. Hao, C. L. Nehl, J. H. Hafner and P. Nordlander, *Nano Letters*, 2007, **7**, 729–732.

60 C. V. Raman and K. S. Krishnan, *Nature*, 1928, **121**, 501–502.

61 A. Smekal, *Die Naturwissenschaften*, 1923, 11, 873–875.

62 P. Vítek, E. M. A. Ali, H. G. M. Edwards, J. Jehlička, R. Cox and K. Page, *Spectrochimica Acta Part A: Molecular and Biomolecular Spectroscopy*, 2012, **86**, 320–327.

63 D. I. Ellis, D. P. Cowcher, L. Ashton, S. O'Hagan and R. Goodacre, *The Analyst*, 2013, **138**, 3871.

64 I. R. Lewis, N. W. Daniel, N. C. Chaffin, P. R. Griffiths and M. W. Tungol, *Spectrochimica Acta Part A: Molecular Spectroscopy*, 1995, **51**, 1985–2000.

65 W. E. Smith and G. Dent, *Modern Raman spectroscopy—a practical approach, John Wiley and Sons Ltd, Chichester, UK*, John Wiley & Sons, Ltd, 2005.

66 H. A. Szymanski, *Raman Spectroscopy : Theory and Practice*, Springer US, 1967.

67 G. Kister, G. Cassanas, M. Vert and C. Flahault, *Infra-red and Raman spectroscopy*, 1998, vol. 39.

68 J. R. Ferraro, K. Nakamoto and C. W. Brown, *Introductory Raman Spectroscopy*, Academic Press, 2003.

69 O. Stevens, I. E. Iping Petterson, J. C. C. Day and N. Stone, *Chemical Society*

Reviews, 2016, **45**, 1919–1934.

70 B. Robert, *Photosynthesis Research*, 2009, **101**, 147–155.

71 A. P. Shreve, N. J. Cherepy and R. A. Mathies, *Applied Spectroscopy*, 1992, **46**, 707–711.

72 P. Matousek, M. Towrie, C. Ma, W. M. Kwok, D. Phillips, W. T. Toner and A. W. Parker, *Journal of Raman Spectroscopy*, 2001, **32**, 983–988.

73 Nie and Emory, *Science*, 1997, **275**, 1102–6.

74 M. Fleischmann, P. J. Hendra and A. J. McQuillan, *Chemical Physics Letters*, 1974, **26**, 163–166.

75 E. C. Le Ru and P. G. Etchegoin, *Annual Review of Physical Chemistry*, 2012, **63**, 65–87.

76 J. Docherty, S. Mabbott, E. Smith, K. Faulds, C. Davidson, J. Reglinski and D. Graham, *Analyst*, 2016, **141**, 5857–5863.

77 K. Gracie, E. Correa, S. Mabbott, J. A. Dougan, D. Graham, R. Goodacre and K. Faulds, *Chemical Science*, 2014, **5**, 1030–1040.

78 M. G. Albrecht and J. A. Creighton, *Journal of the American Chemical Society*, 1977, **99**, 5215–5217.

79 D. L. Jeanmaire and R. P. Van Duyne, *Journal of Electroanalytical Chemistry*, 1977, **84**, 1–20.

80 M. Moskovits, *Reviews of Modern Physics*, 1985, **57**, 783–826.

81 S. L. Kleinman, R. R. Frontiera, A.-I. Henry, J. A. Dieringer and R. P. Van Duyne, *Physical Chemistry Chemical Physics*, 2013, **15**, 21–36.

82 T. Chen, H. Wang, G. Chen, Y. Wang, Y. Feng, W. S. Teo, T. Wu and H. Chen, *ACS Nano*, 2010, **4**, 3087–3094.

83 X. Zhao and M. Chen, *RSC Adv.*, 2014, **4**, 63596–63602.

84 J. R. Lombardi and R. L. Birke, *Accounts of Chemical Research*, 2009, **42**,

734–742.

85 A. A. Stacy and R. P. Van Duyne, *Chemical Physics Letters*, 1983, **102**, 365–370.

86 G. McNay, D. Eustace, W. E. Smith, K. Faulds and D. Graham, *Applied Spectroscopy*, 2011, **65**, 825–837.

87 K. Faulds, R. E. Littleford, D. Graham, G. Dent and W. E. Smith, *Analytical Chemistry*, 2004, **76**, 592–598.

88 Z. Starowicz, R. Wojnarowska-Nowak, P. Ozga and E. M. Sheregii, *Colloid and polymer science*, 2018, **296**, 1029–1037.

89 J. A. Dougan and K. Faulds, *The Analyst*, 2012, **137**, 545–554.

90 K. Faulds, R. Jarvis, W. E. Smith, D. Graham and R. Goodacre, *The Analyst*, 2008, **133**, 1505.

91 J. Popp, C. Krafft and T. Mayerhöfer, *Optik & Photonik*, 2011, **6**, 24–28.

92 J. M. Schmitt, A. Knuttel, M. Yadlowsky and M. A. Eckhaus, *Physics in Medicine and Biology*, 1994, **39**, 1705–1720.

93 H. Kearns, N. C. Shand, W. E. Smith, K. Faulds and D. Graham, *Physical chemistry chemical physics : PCCP*, 2015, **17**, 1980–6.

94 M. A. Bedics, H. Kearns, J. M. Cox, S. Mabbott, F. Ali, N. C. Shand, K. Faulds, J. B. Benedict, D. Graham and M. R. Detty, *Chem. Sci.*, 2015, **6**, 2302–2306.

95 H. Kearns, M. A. Bedics, N. C. Shand, K. Faulds, M. R. Detty and D. Graham, *The Analyst*, 2016, **141**, 5062–5065.

96 R. Smith, K. L. Wright and L. Ashton, *Analyst*, 2016, 141, 3590–3600.

97 L. Frame, J. Brewer, R. Lee, K. Faulds and D. Graham, *Analyst*, 2018, **143**, 157–163.

98 K. C. Gordon and C. M. McGoverin, *International Journal of Pharmaceutics*, 2011, 417, 151–162.

99 P. Ropret, C. Miliani, S. A. Centeno, Č. Tavzes and F. Rosi, *Journal of Raman Spectroscopy*, 2010, **41**, 1462–1467.

100 M. A. Bedics, K. R. Mulhern, D. F. Watson and M. R. Detty, *The Journal of Organic Chemistry*, 2013, **78**, 8885–8891.

101 K. A. Leonard, M. I. Nelen, L. T. Anderson, S. L. Gibson, R. Hilf and M. R. Detty, *Journal of medicinal chemistry*, 1999, **42**, 3942–52.

102 S. P. Ebert, B. Wetzel, R. L. Myette, G. Conseil, S. P. C. Cole, G. A. Sawada, T. W. Loo, M. C. Bartlett, D. M. Clarke and M. R. Detty, *Journal of Medicinal Chemistry*, 2012, **55**, 4683–4699.

103 R. E. McKnight, M. Ye, T. Y. Ohulchanskyy, S. Sahabi, B. R. Wetzel, S. J. Wagner, A. Skripchenko and M. R. Detty, *Bioorganic & Medicinal Chemistry*, 2007, **15**, 4406–4418.

104 M. R. Detty and B. J. Murray, *The Journal of Organic Chemistry*, 1982, **47**, 5235–5239.

105 M. R. Detty, J. M. McKelvey and H. R. Luss, *Organometallics*, 1988, **7**, 1131–1147.

106 S. Harmsen, M. A. Bedics, M. A. Wall, R. Huang, M. R. Detty and M. F. Kircher, *Nature Communications*, 2015, **6**, 6570.

107 A. F. Palonpon, J. Ando, H. Yamakoshi, K. Dodo, M. Sodeoka, S. Kawata and K. Fujita, *Nature Protocols*, 2013, **8**, 677–692.

108 H. Yamakoshi, K. Dodo, A. Palonpon, J. Ando, K. Fujita, S. Kawata and M. Sodeoka, *Journal of the American Chemical Society*, 2012, **134**, 20681–20689.

109 M. Futamata and M. I. Y. Maruyama, *Journal of Physical Chemistry*, 2003, **107**, 7607–7617.

110 I. D. G. Macdonald and W. E. Smith, *Langmuir*, 1996, **12**, 706–713.

111 L. Seballos, T. Y. Olson and J. Z. Zhang, *Journal of Chemical Physics*, 2006,

125, 234706.

112 A. Michota and J. Bukowska, *Journal of Raman Spectroscopy*, 2003, **34**, 21–25.

113 M. A. Bedics, H. Kearns, J. M. Cox, S. Mabbott, F. Ali, N. C. Shand, K. Faulds, J. B. Benedict, D. Graham and M. R. Detty, *Chem. Sci.*, 2015, **6**, 2302–2306.

114 H. Kearns, S. Sengupta, I. R. Sasselli, L. Bromley III, K. Faulds, T. Tuttle, M. A. Bedics, M. R. Detty, L. Velarde, D. Graham and W. E. Smith, *Chem. Sci.*, 2016, **7**, 5160–5170.

115 J. H. Hunt, P. Guyot-Sionnest and Y. R. Shen, *Chemical Physics Letters*, 1987, **133**, 189–192.

116 Y. R. Shen, *Nature*, 1989, 337, 519–525.

117 H. Kearns, S. Sengupta, I. R. Sasselli, L. Bromley III, K. Faulds, T. Tuttle, M. A. Bedics, M. R. Detty, L. Velarde, D. Graham and W. E. Smith, *Chem. Sci.*, 2016, **7**, 5160–5170.

118 S. Moreton, K. Faulds, N. Shand, M. Bedics, M. Detty and D. Graham, *Nanoscale*, 2015, **7**, 6075–6082.

119 D. K. Carpenter, *Journal of Chemical Education*, 2009, **54**, A430.

120 M. Panalytical, Zeta potential measurement to improve formulation stability, https://www.malvernpanalytical.com/en/products/measurement-type/zeta-potential/, (accessed 6 May 2019).

121 T. Cosgrove, *Colloid science : principles, methods and applications*, Wiley, 2010.

122 K. Dégardin, Y. Roggo and P. Margot, *Journal of Pharmaceutical and Biomedical Analysis*, 2014, **87**, 167–175.

123 Frontier Economics, *The Economic Impacts of Counterfeiting and Piracy*, 2016.

124 G. Power, *Impact - World Health Organisation Report*, 2008, 1–13.

125 Y. Cui, I. Y. Phang, Y. H. Lee, M. R. Lee, Q. Zhang and X. Y. Ling, *Chemical Communications*, 2015, **51**, 5363–5366.

126 L. S. Lawson and J. D. Rodriguez, *Analytical Chemistry*, 2016, **88**, 4706–4713.

127 M. Haris, S. K. Yadav, A. Rizwan, A. Singh, E. Wang, H. Hariharan, R. Reddy and F. M. Marincola, *Journal of Translational Medicine*, 2015, **13**, 313.

128 T. Saga, *Japanese Journal of Clinical Radiology*, 2011, **56**, 311–319.

129 N. J. Everall, *Applied Spectroscopy*, 2000, **54**, 773–782.

130 Y. Omura, D. Lu, B. O'Young, M. Jones, A. Nihrane, H. Duvvi, Y. Shimotsuura and M. Ohki, *Acupuncture & electro-therapeutics research*, 2015, **40**, 1–15.

131 P. Matousek, I. P. Clark, E. R. C. Draper, M. D. Morris, A. E. Goodship, N. Everall, M. Towrie, W. F. Finney and A. W. Parker, *Applied Spectroscopy*, 2005, **59**, 393–400.

132 P. Matousek, *TrAC - Trends in Analytical Chemistry*, 2018, 103, 209–214.

133 B. Sharma, K. Ma, M. R. Glucksberg and R. P. Van Duyne, *Journal of the American Chemical Society*, 2013, **135**, 17290–17293.

134 A. S. Moody, P. C. Baghernejad, K. R. Webb and B. Sharma, *Analytical Chemistry*, 2017, **89**, 5688–5692.

135 N. Stone, R. Baker, K. Rogers, A. W. Parker and P. Matousek, *Analyst*, 2007, **132**, 899–905.

136 F. Nicolson, L. E. Jamieson, S. Mabbott, K. Plakas, N. C. Shand, M. R. Detty, D. Graham and K. Faulds, *Chemical Science*, 2018, **9**, 3788–3792.

137 R. H. Clarke, *Google Patents*.

138 A. Miernik, Y. Eilers, C. Bolwien, A. Lambrecht, D. Hauschke, G. Rebentisch, P. S. Lossin, A. Hesse, J. J. Rassweiler, U. Wetterauer and M. Schoenthalerk,

Journal of Urology, 2013, **190**, 1895–1900.

139 R. O. P. Draga, M. C. M. Grimbergen, P. L. M. Vijverberg, C. F. P. van Swol, T. G. N. Jonges, J. A. Kummer and J. L. H. Ruud Bosch, *Analytical Chemistry*, 2010, **82**, 5993–5999.

140 S. L. Jacques, *Physics in Medicine and Biology*, 2013, 58, 37–61.

141 A. M. Smith, M. C. Mancini and S. Nie, *Nature Nanotechnology*, 2009, 4, 710–711.

142 L. T. Kerr, H. J. Byrne and B. M. Hennelly, *Analytical Methods*, 2015, **7**, 5041–5052.

143 F. L. Magalhães, A. M. C. Machado, E. Paulino, S. K. Sahoo, A. M. de Paula, A. M. Garcia, I. Barman and J. S. Soares, *Journal of Biomedical Optics*, 2018, **23**, 1.

144 I. J. Pence, C. A. Patil, C. A. Lieber and A. Mahadevan-Jansen, *Biomedical Optics Express*, 2015, **6**, 2724.

145 F. Nicolson, L. E. Jamieson, S. Mabbott, N. C. Shand, D. Graham and K. Faulds, *Journal of Raman Spectroscopy*, 2017, **48**, 1828–1838.

146 F. Nicolson, L. E. Jamieson, S. Mabbott, K. Plakas, N. C. Shand, M. R. Detty, D. Graham and K. Faulds, *Analyst*, 2018, **143**, 5965–5973.

147 J. Taylor, A. Huefner, L. Li, J. Wingfield and S. Mahajan, *Analyst*, 2016, 141, 5037–5055.

148 L. Shang, K. Nienhaus and G. U. Nienhaus, *Journal of Nanobiotechnology*, 2014, 12, 5.

149 V. Pillay, K. Murugan, Y. E. Choonara, P. Kumar, D. Bijukumar and L. C. du Toit, *International Journal of Nanomedicine*, 2015, **10**, 2191.

150 J. Chan, S. Fore, S. Wachsmann-Hogiu and T. Huser, *Laser and Photonics Reviews*, 2008, 2, 325–349.

151 R. Smith, K. L. Wright and L. Ashton, *Analyst*, 2016, 141, 3590–3600.

152 A. Mitchell, L. Ashton, X. B. Yang, R. Goodacre, A. Smith and J. Kirkham, *Cytometry Part A*, 2015, **87**, 1012–1019.

153 X. Cao, C. Shi, W. Lu, H. Zhao, M. Wang, M. Zhang, X. Chen, J. Dong, X. Han and W. Qian, *Journal of Nanoscience and Nanotechnology*, 2016, **16**, 12161–12171.

154 I. R. Nabiev, H. Morjani and M. Manfait, *European Biophysics Journal*, 1991, **19**, 311–316.

155 C. A. R. Auchinvole, P. Richardson, C. McGuinnes, V. Mallikarjun, K. Donaldson, H. McNab and C. J. Campbell, *ACS Nano*, 2012, **6**, 888–896.

156 M. F. Escoriza, J. M. Vanbriesen, S. Stewart and J. Maier, in *Applied Spectroscopy*, SAGE PublicationsSage UK: London, England, 2007, vol. 61, pp. 812–823.

157 Y. H. Ong, M. Lim and Q. Liu, *Optics Express*, 2012, **20**, 25041.

158 Z. Zhai, F. Zhang, X. Chen, J. Zhong, G. Liu, Y. Tian and Q. Huang, *Lab on a Chip*, 2017, **17**, 1306–1313.

159 D. C. Kennedy, C. S. McKay, L. L. Tay, Y. Rouleau and J. P. Pezacki, *Chemical Communications*, 2011, **47**, 3156–3158.

160 M. Li, J. Wu, M. Ma, Z. Feng, Z. Mi, P. Rong and D. Liu, *Nanotheranostics*, 2019, **3**, 113–119.

161 F. Nicolson, L. E. Jamieson, S. Mabbott, K. Plakas, N. C. Shand, M. R. Detty, D. Graham and K. Faulds, *Chemical Communications*, 2018, **54**, 8530–8533.

162 W. Strober, in *Current Protocols in Immunology*, John Wiley & Sons, Inc., Hoboken, NJ, USA, 2001, vol. 21, p. A.3B.1-A.3B.2.

163 J. O'Brien, I. Wilson, T. Orton and F. Pognan, *European Journal of Biochemistry*, 2000, **267**, 5421–5426.

164 ThermoFisher, alamarBlue Cell Viability Reagent - Thermo Fisher Scientific,

https://www.thermofisher.com/order/catalog/product/DAL1025, (accessed 20 May 2019).

165 SYTOX Green Nucleic Acid Stain - 5 mM Solution in DMSO - Thermo Fisher Scientific, https://www.thermofisher.com/order/catalog/product/S7020?SID=srch-srp-S7020, (accessed 20 May 2019).

10. Appendix

- Appendix 1 – CP Dye Absorption Measurements
- Appendix 2 – Extinction Spectra
- Appendix 3 – DLS and Zeta Measurements
- Appendix 4 – Pre-processed Cell Images
- Appendix 5 – Conference Presentations

Appendix 1 – Dye Absorption Measurements

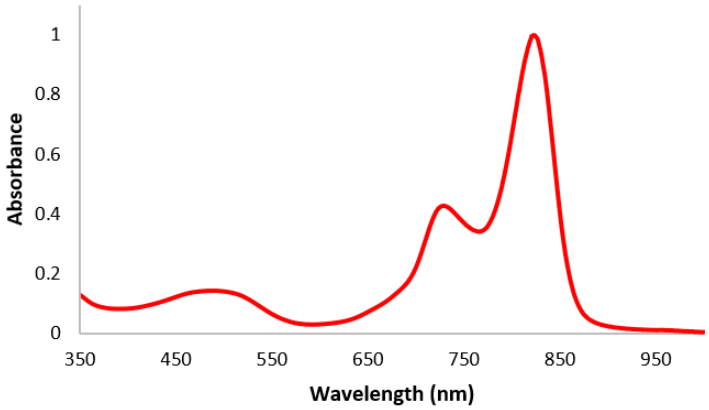

Figure 57 - Dye absorbance spectra of dye 1, measured in DMF at a scan rate of 1 nm per second.

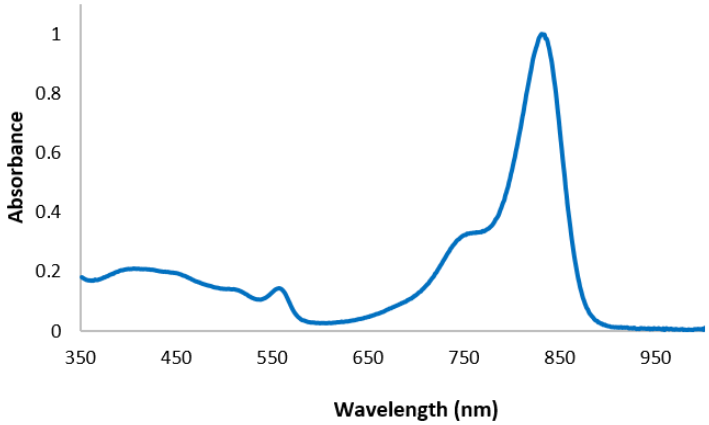

Figure 58 - Dye absorbance spectra of dye 2, measured in DMF at a scan rate of 1 nm per second.

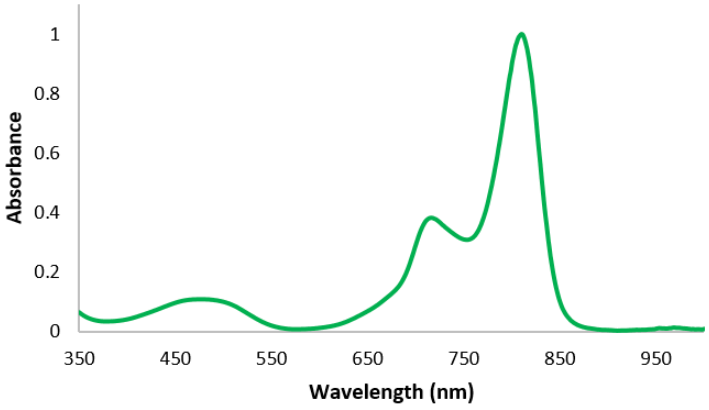

Figure 59 - Dye absorbance spectra of dye 3, measured in DMF at a scan rate of 1 nm per second.

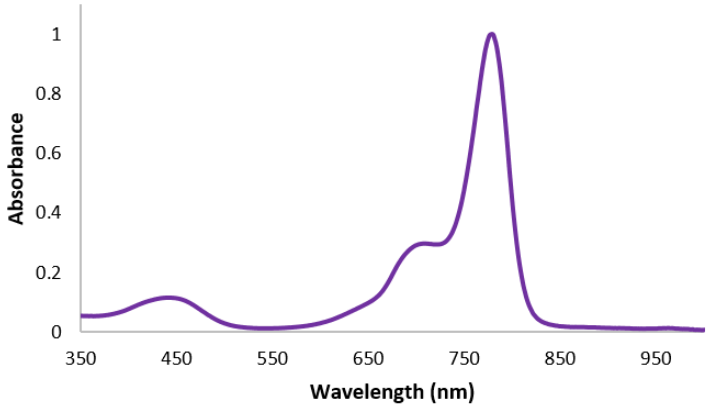

Figure 60 - Dye absorbance spectra of dye 4 measured in DMF at a scan rate of 1 nm per second.

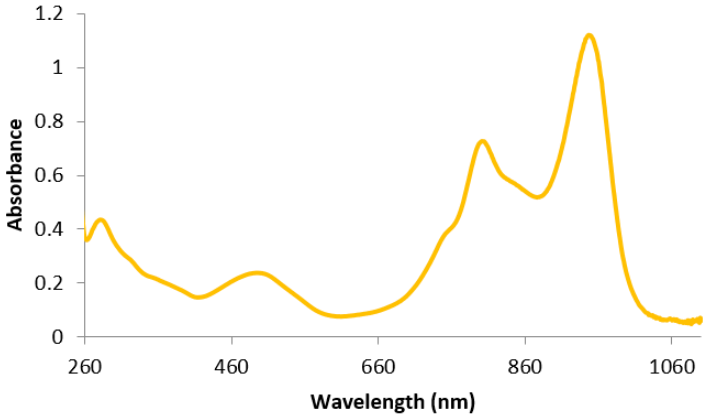

Figure 61 - Dye absorbance spectra, of dye 6, measured in DMF at a scan rate of 1 nm per second.

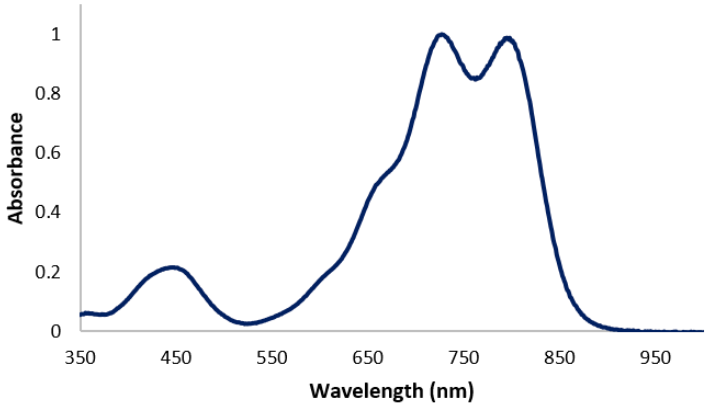

Figure 62 – Dye absorbance spectra of nanoparticles functionalised with the CP blocking molecule measured at a scan rate of 1 nm per second.

Appendix 2 – Extinction Spectra

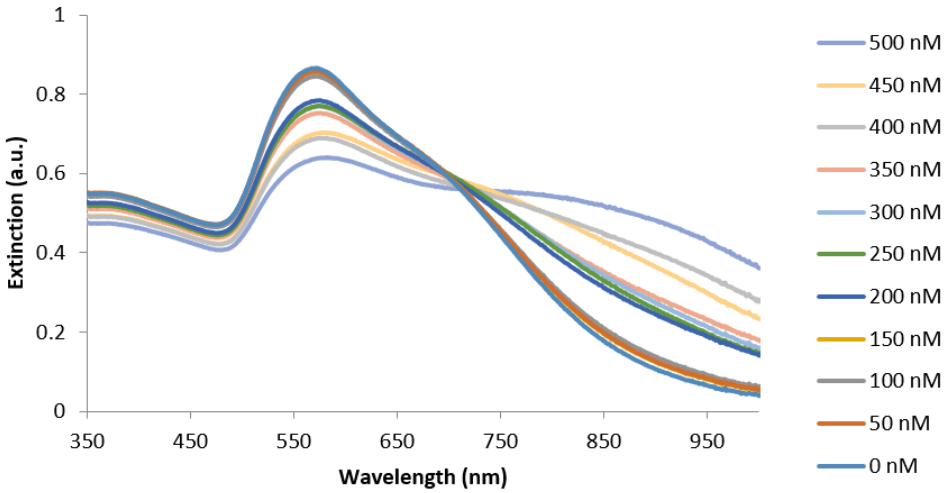

Figure 63 - Extinction spectra of nanoparticles functionalised with dye 1 over the concentration range 50 - 500 nM, measured at a scan rate of 1 nm per second.

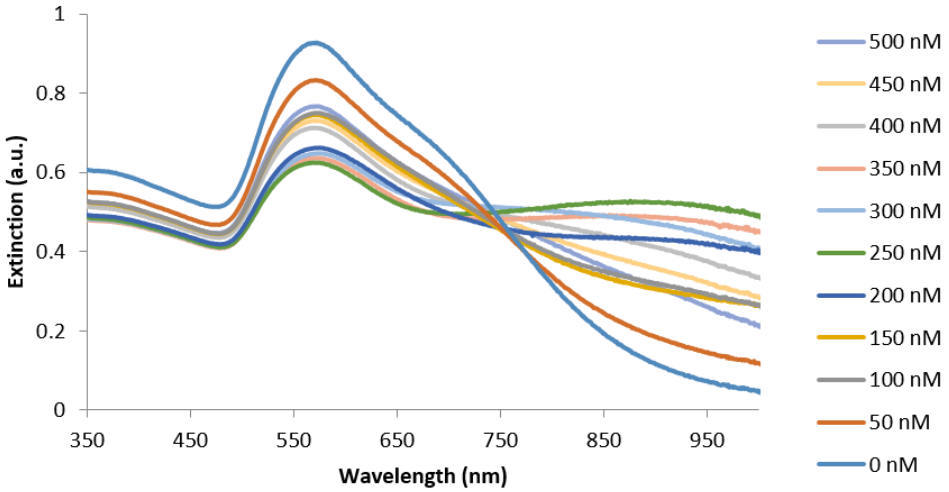

Figure 64 - Extinction spectra of nanoparticles functionalised with dye 2 over the concentration range 50 - 500 nM, measured at a scan rate of 1 nm per second.

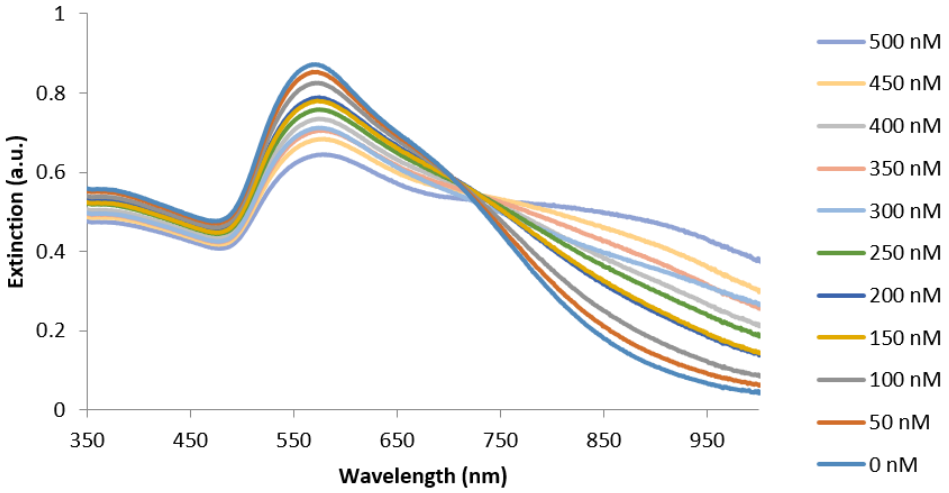

Figure 65 - Extinction spectra of nanoparticles functionalised with dye 3 over the concentration range 50 - 500 nM, measured at a scan rate of 1 nm per second.

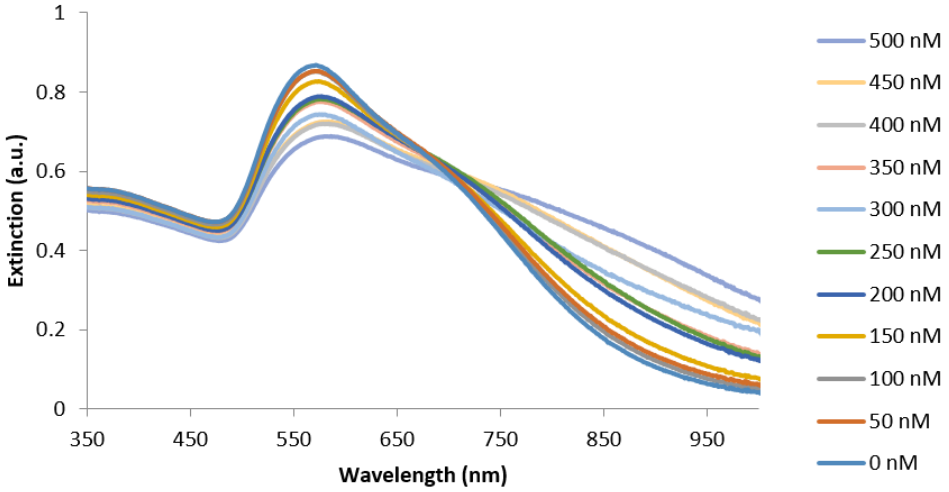

Figure 66 - Extinction spectra of nanoparticles functionalised with dye 4 over the concentration range 50 - 500 nM, measured at a scan rate of 1 nm per second.

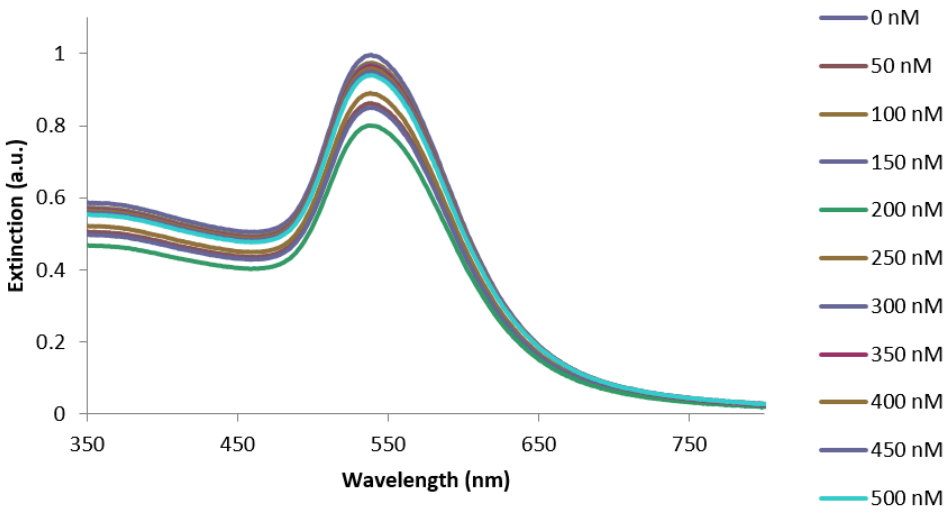

Figure 67 - Extinction spectra of nanoparticles functionalised with dye 6 over the concentration range 50 - 500 nM, measured at a scan rate of 1 nm per second.

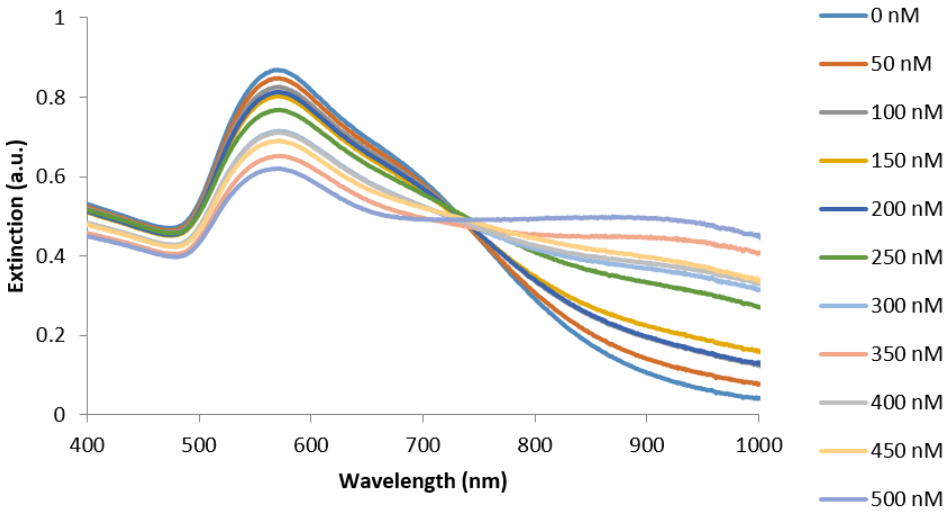

Figure 68 - Extinction spectra of nanoparticles functionalised with the CP blocking molecule (used in chapter 3) over the concentration range 50 - 500 nM, measured at a scan rate of 1 nm per second.

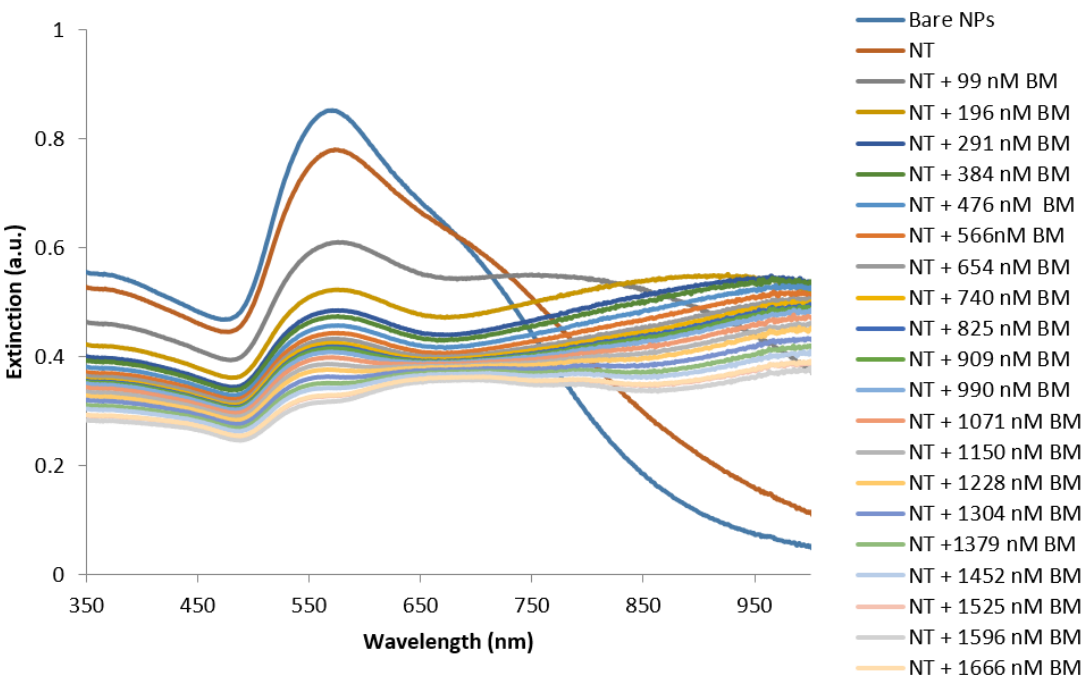

Figure 69 – Extinction spectra of the nanotag (gold nanoparticles functionalised with dye 6 at a final concentration of 350 nM) with the addition of the blocking molecule over a concentration range of 99 – 1666 nM, measured at a scan rate of 1 nm per second.

Appendix 3 - DLS and Zeta Potential Measurements

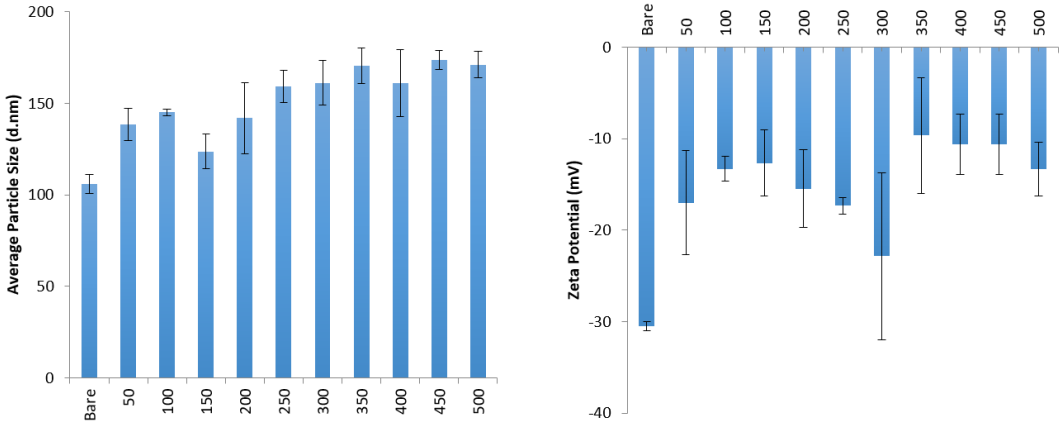

Figure 70 - DLS and Zeta potential measurements of gold nanoparticles functionalised with dye 1 over the concentration range of 50 - 500 nM.

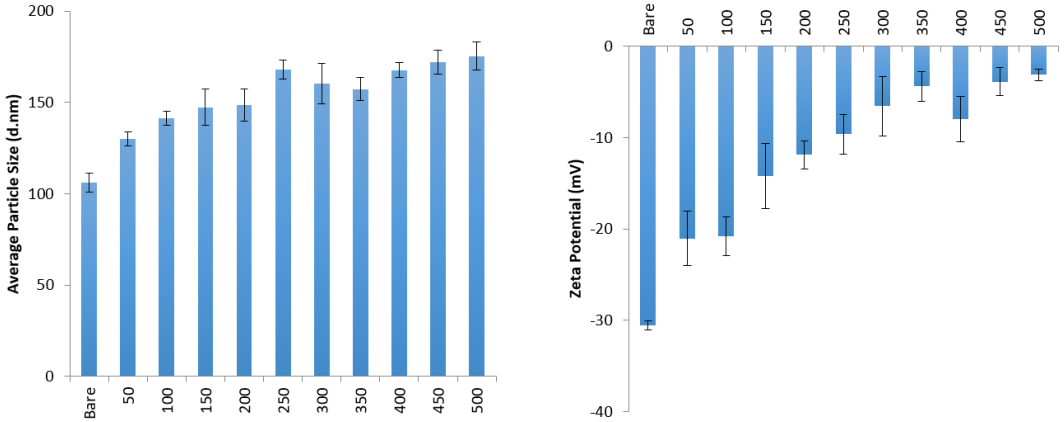

Figure 71 - DLS and Zeta potential measurements of gold nanoparticles functionalised with dye 2 over the concentration range of 50 - 500 nM.

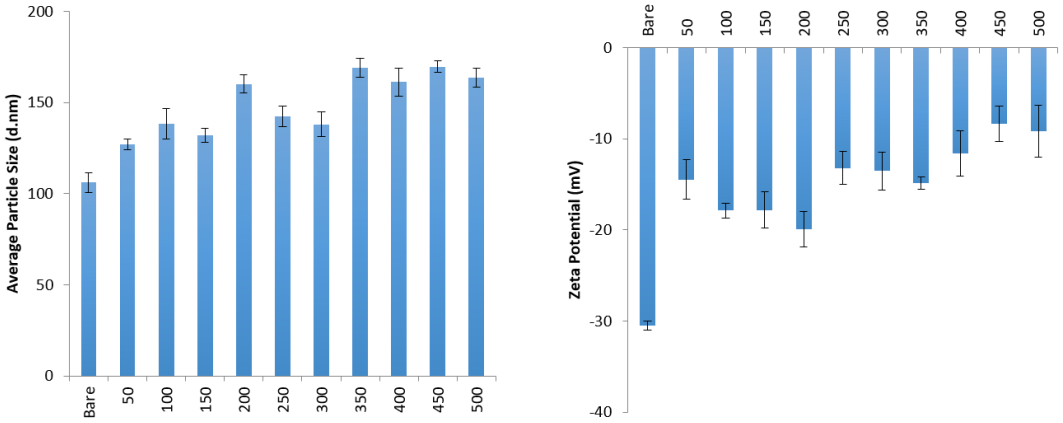

Figure 72 - DLS and Zeta potential measurements of gold nanoparticles functionalised with dye 3 over the concentration range of 50 - 500 nM.

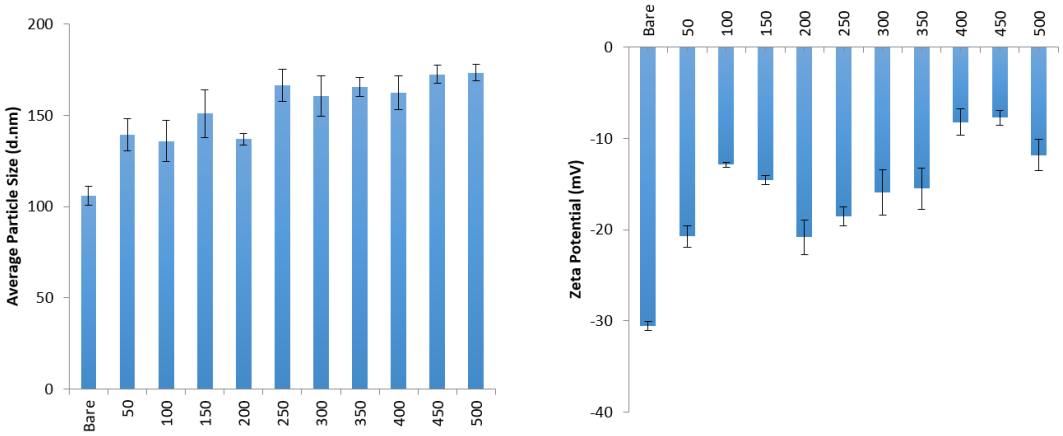

Figure 73 - DLS and Zeta potential measurements of gold nanoparticles functionalised with dye 4 over the concentration range of 50 - 500 nM.

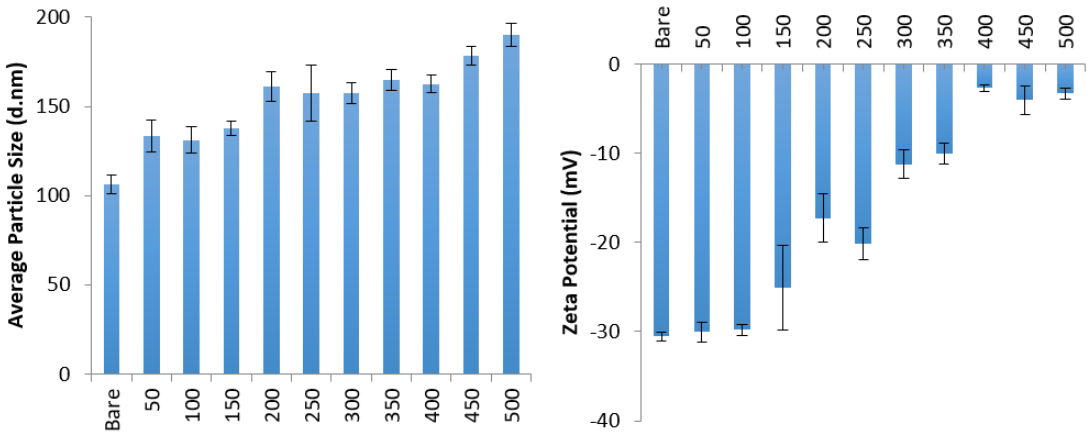

Figure 74 - DLS and Zeta potential measurements of gold nanoparticles functionalised with dye 6 over the concentration range 50 - 500 nM.

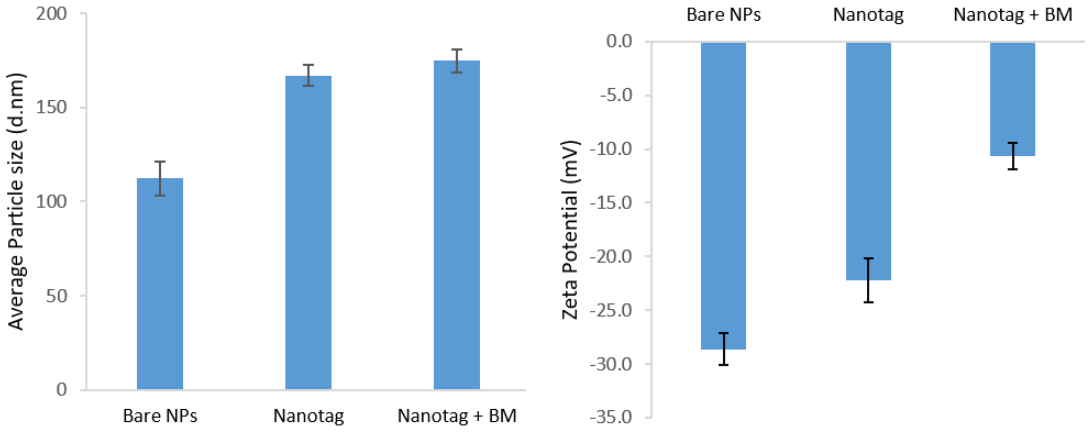

Figure 75 – DLS and Zeta potential measurements of the nanotag (gold nanoparticles functionalised with dye 6 at a final concentration of 350 nM) with the addition of the blocking molecule at a concentration of 1666 nM.

Appendix 4 – Pre-processed Cell Images

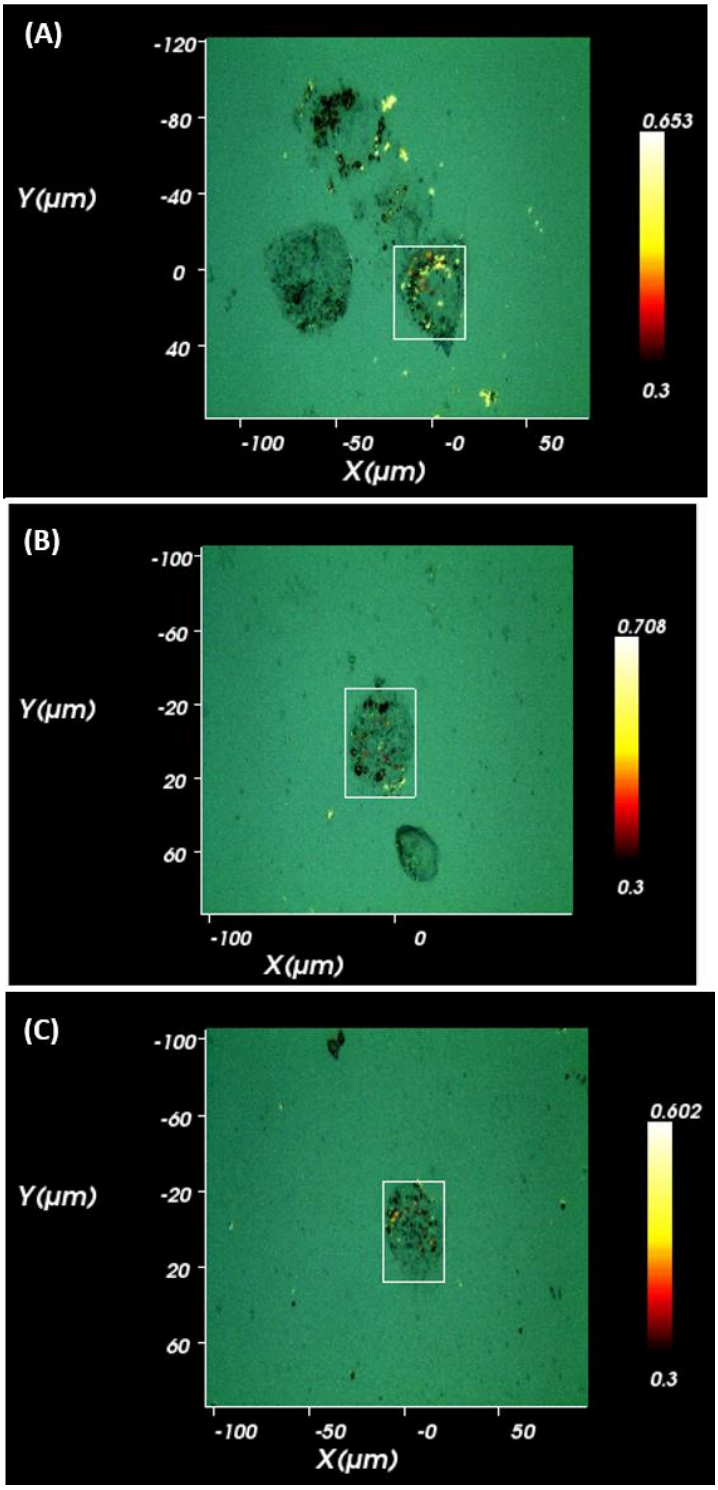

Figure 76 – Pre-processed images of cells dosed with dye 1 functionalised nanoparticles of concentration (A) 1.25 nM, (B) 12.5 nM and (c) 125 nM. The cell sample was analysed at 633 nm, 10% laser power (500 mW), 0.2-second acquisition time, centred at 1300 cm^{-1}.

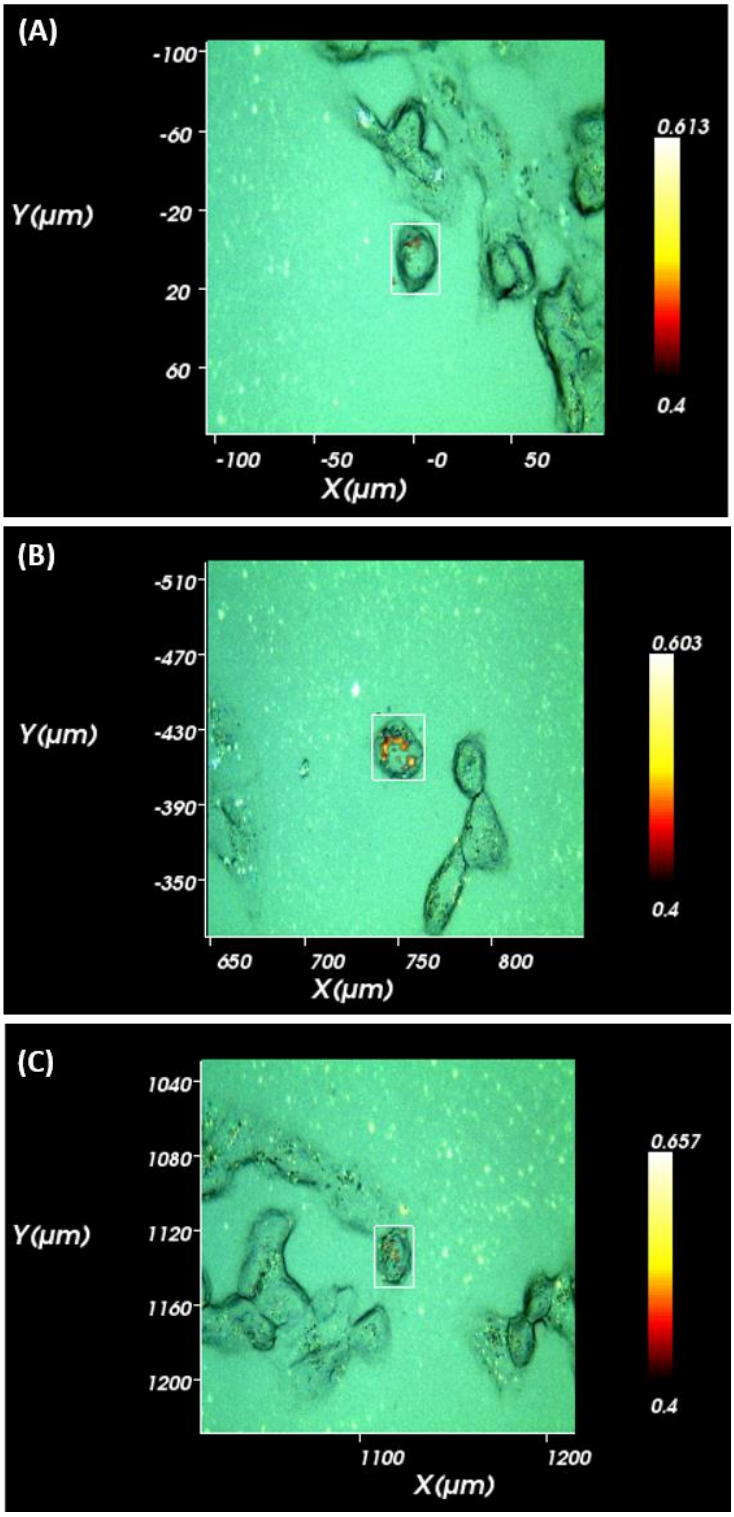

Figure 77 - Pre-processed images of cells dosed with dye 2 functionalised nanoparticles of concentration (A) 1.25 nM, (B) 12.5 nM and (c) 125 nM. The cell sample was analysed at 633 nm, 10% laser power (500 mW), 0.2-second acquisition time, centred at 1300 cm^{-1}.

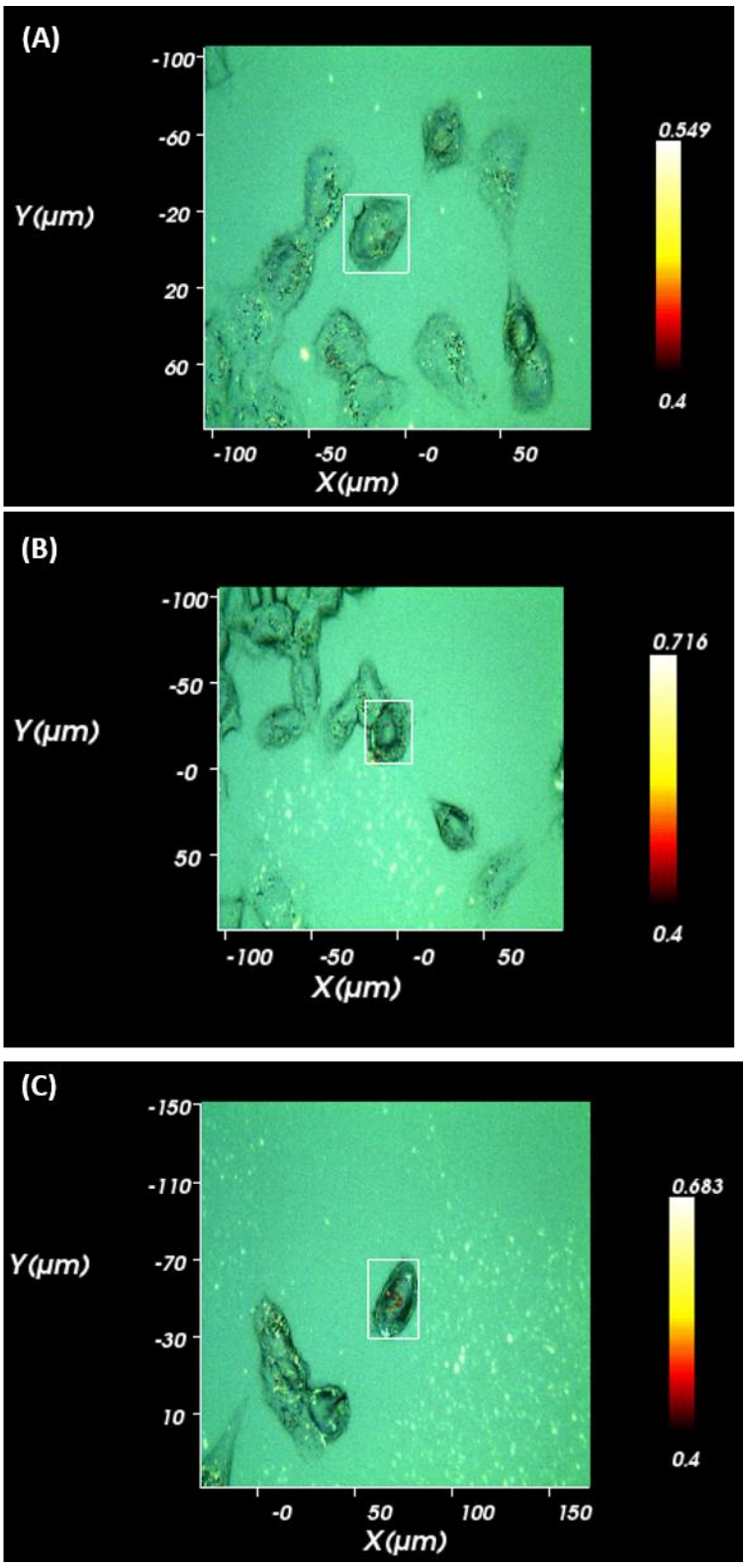

Figure 78 - Pre-processed images of cells dosed with dye 3 functionalised nanoparticles of concentration (A) 1.25 nM, (B) 12.5 nM and (c) 125 nM. The cell sample was analysed at 633 nm, 10% laser power (500 mW), 0.2-second acquisition time, centred at 1300 cm^{-1}.

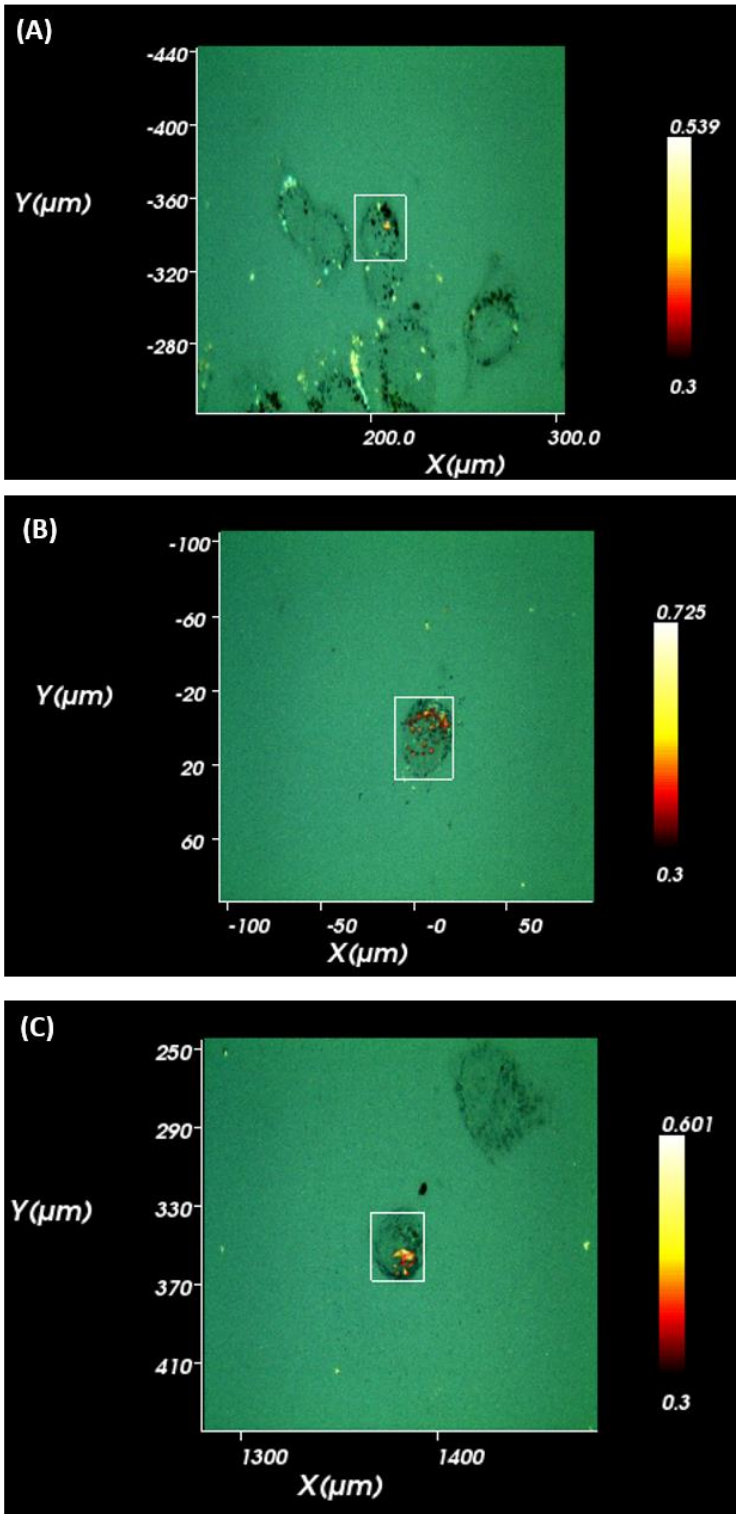

Figure 79 - Pre-processed images of cells dosed with dye 4 functionalised nanoparticles of concentration (A) 1.25 nM, (B) 12.5 nM and (c) 125 nM. The cell sample was analysed at 633 nm, 10% laser power (500 mW), 0.2-second acquisition time, centred at 1300 cm^{-1}.

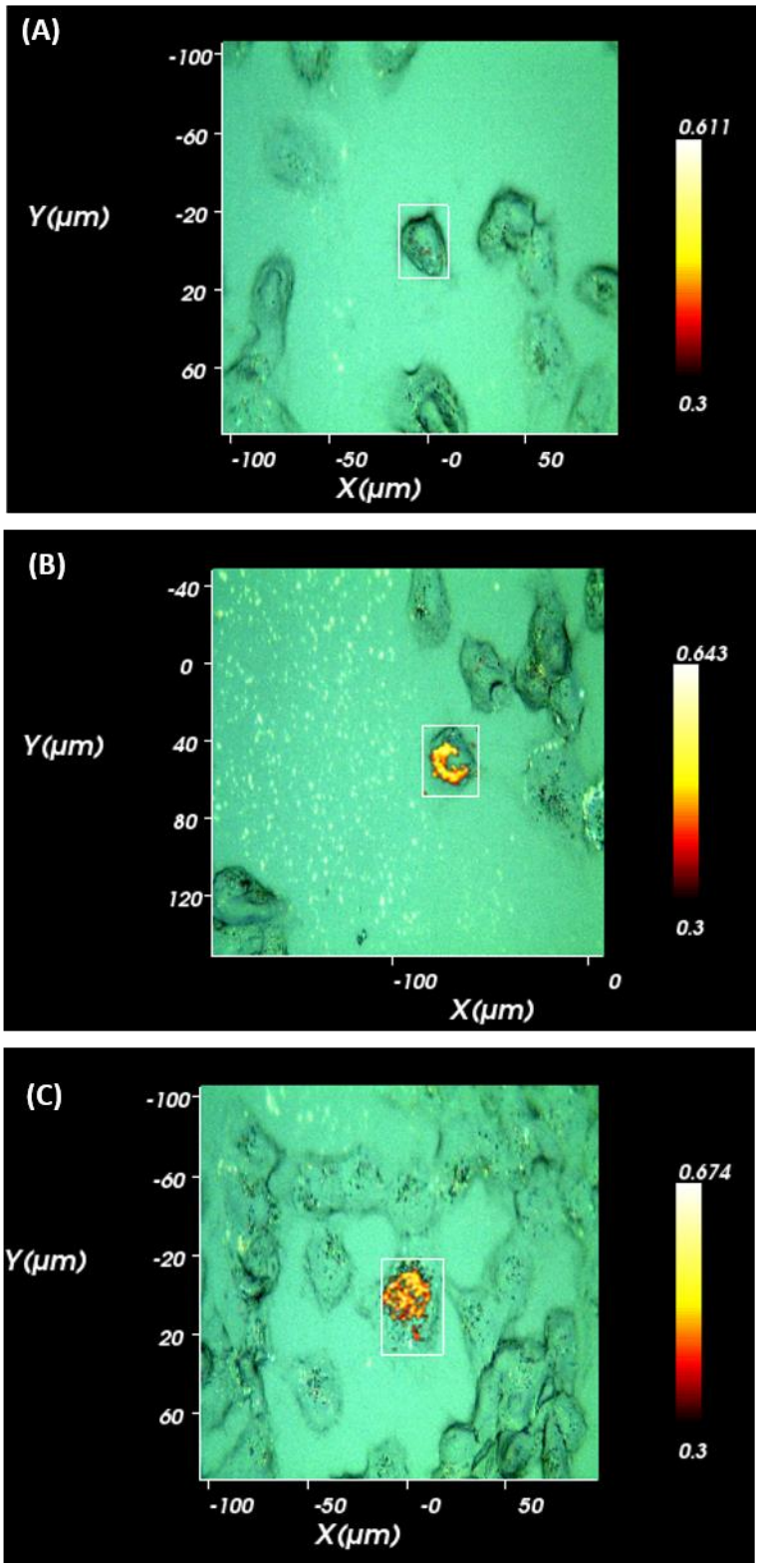

Figure 80 - Pre-processed images of cells dosed with dye 6 functionalised nanoparticles of concentration (A) 1.25 nM, (B) 12.5 nM and (c) 125 nM. The cell sample was analysed at 633 nm, 10% laser power (500 mW), 0.2-second acquisition time, centred at 1300 cm^{-1}.

Appendix 5 – Conference Presentations

- **Spring SciX 2018**
  Oral Presentation
  The University of Strathclyde, Glasgow, UK
  "Functionalisation of Nanoparticles for Use as Red-Shifted SERS Nanotags and their Biological Applications"

- **University at Buffalo Graduate Student Symposium 2018**
  Poster Presentation
  The University at Buffalo, New York, USA
  "Red-Shifted Nanomaterials for Invisible Tagging and Detection"

- **Analytical Research Forum 2018**
  Poster Presentation
  The Royal Society of Chemistry, Burlington House, London, UK
  "Wavelength Selective SERS for Invisible Tagging and Detection"

- **FACSS SciX 2019**
  Oral Presentation
  Atlanta, Georgia, USA
  "Exploiting a New Class of Raman Active Dyes and Near Infra-Red SERS with Promising Biological Applications"